

AFRL-AFOSR-UK-TR-2014-0039



Development and Application of Laser-Induced Energy Deposition for Flow Control of Edney Type IV Interactions

Konstantinos Kontis

**University of Manchester Research Office
Oxford Road
Manchester M13 9PL
UNITED KINGDOM**

EOARD Grant 12-2007

Report Date: October 2014

Final Report from 15 March 2012 to 28 February 2014

Distribution Statement A: Approved for public release distribution is unlimited.

**Air Force Research Laboratory
Air Force Office of Scientific Research
European Office of Aerospace Research and Development
Unit 4515, APO AE 09421-4515**

REPORT DOCUMENTATION PAGE				Form Approved OMB No. 0704-0188	
<p>Public reporting burden for this collection of information is estimated to average 1 hour per response, including the time for reviewing instructions, searching existing data sources, gathering and maintaining the data needed, and completing and reviewing the collection of information. Send comments regarding this burden estimate or any other aspect of this collection of information, including suggestions for reducing the burden, to Department of Defense, Washington Headquarters Services, Directorate for Information Operations and Reports (0704-0188), 1215 Jefferson Davis Highway, Suite 1204, Arlington, VA 22202-4302. Respondents should be aware that notwithstanding any other provision of law, no person shall be subject to any penalty for failing to comply with a collection of information if it does not display a currently valid OMB control number.</p> <p>PLEASE DO NOT RETURN YOUR FORM TO THE ABOVE ADDRESS.</p>					
1. REPORT DATE (DD-MM-YYYY) 31 October 2014		2. REPORT TYPE Final Report		3. DATES COVERED (From – To) 15 March 2012 –28 February 2014	
4. TITLE AND SUBTITLE Development and Application of Laser-Induced Energy Deposition for Flow Control of Edney Type IV Interactions			5a. CONTRACT NUMBER FA8655-12-1-2007		
			5b. GRANT NUMBER Grant 12-2007		
			5c. PROGRAM ELEMENT NUMBER 61102F		
			5d. PROJECT NUMBER		
6. AUTHOR(S) Konstantinos Kontis			5d. TASK NUMBER		
			5e. WORK UNIT NUMBER		
7. PERFORMING ORGANIZATION NAME(S) AND ADDRESS(ES) University of Manchester Research Office Oxford Road Manchester M13 9PL UNITED KINGDOM			8. PERFORMING ORGANIZATION REPORT NUMBER N/A		
9. SPONSORING/MONITORING AGENCY NAME(S) AND ADDRESS(ES) EOARD Unit 4515 APO AE 09421-4515			10. SPONSOR/MONITOR'S ACRONYM(S) AFRL/AFOSR/IOE (EOARD)		
			11. SPONSOR/MONITOR'S REPORT NUMBER(S) AFRL-AFOSR-UK-TR-2014-0039		
12. DISTRIBUTION/AVAILABILITY STATEMENT Distribution A: Approved for public release; distribution is unlimited.					
13. SUPPLEMENTARY NOTES					
14. ABSTRACT This report describes the research activities conducted at the University of Manchester in this project. A comprehensive literature survey of the relevant phenomena and subsequent interactions is presented along with a description of the wind tunnel facility calibration. Experimental techniques and methodologies are discussed, including reference to the range of their applicability in the campaign. Model designs, experimental setup, and preliminary analysis of the flow field are presented. The following techniques have already been used in the experimental programme: high speed schlieren photography, infrared thermography and force measurements taken from a three-component balance.					
15. SUBJECT TERMS EOARD, edney iv, energy deposition, hypersonics					
16. SECURITY CLASSIFICATION OF:			17. LIMITATION OF ABSTRACT SAR	18. NUMBER OF PAGES 113	19a. NAME OF RESPONSIBLE PERSON Gregg L. Abate
a. REPORT UNCLAS	b. ABSTRACT UNCLAS	c. THIS PAGE UNCLAS			19b. TELEPHONE NUMBER (Include area code) +44 (0)1895 616021

Final Report
EOARD Project: FA8655-12-1-2007

**DEVELOPMENT AND APPLICATION OF LASER-
INDUCED ENERGY DEPOSITION FOR FLOW
CONTROL OF EDNEY TYPE IV INTERACTIONS**

1. Duration: 18 months
2. Name of Organization: University of Manchester
3. Principal Investigator:
Professor Konstantinos Kontis
School of Engineering
University of Glasgow, United Kingdom
E-mail: kostas.kontis@glasgow.ac.uk

Contents

1	Introduction	6
1.1	Relevance of Proposed Research	6
1.2	Research Objectives	7
1.3	Expected Project Contributions and Payoffs	8
2	Literature Review	10
2.1	Introduction	10
2.1.1	In flight consequences of shock impingement	12
2.2	Edney's investigation	13
2.2.1	Type I Interference	14
2.2.2	Type II Interference	16
2.2.3	Type III Interference	16
2.2.4	Type IV Interference	18
2.2.5	Type V Interference	22
2.2.6	Type VI Interference	25
2.2.7	Edney's Findings	27
2.3	Edney Interactions - Further studies	28
2.4	Control Techniques - Energy Deposition	31
2.4.1	Laser Energy Deposition	34
2.4.2	Counter-Flow Jet	38
2.5	Conclusions	44
3	Methodology	45
3.1	Introduction	45
3.2	Hypersonic Tunnel	45
3.2.1	Hypersonic Tunnel Calibration	46
3.3	Experimental Program	48
3.4	Diagnostic Techniques	49

3.4.1	Introduction	49
3.4.2	Surface Oil Flow Imagery	49
3.4.3	Three-component Force Balance	50
3.4.4	Pressure and Temperature Sensitive Paints	50
3.4.5	Schlieren and Shadowgraph	55
3.4.6	Particle Image Velocimetry	57
3.4.7	Infrared Thermography	58
3.5	Experimental Models	59
4	Experimental Tests	63
4.1	Introduction	63
4.2	Measured Data	63
5	Future Work	68
5.1	Work plan for Years 2 and 3	68

List of Figures

1.1	Edney Interference Patterns Overview	7
2.1	Edney Type I interference	14
2.2	Shock polar - Edney Type I interference	15
2.3	Edney Type II interference	17
2.4	Shock polar - Edney Type II interference	18
2.5	Edney Type III interference	19
2.6	Edney Type III interference; detailed depiction	20
2.7	Edney Type IV interference	21
2.8	Edney Type IV interference; detailed depiction	22
2.9	Edney Type IV interference; high speed detailed depiction	22
2.10	Shock polar - Edney Type III/IV interference	23
2.11	Edney Type V interference	24
2.12	Shock polar - Edney Type V interference	25
2.13	Edney Type VI interference	26
2.14	Shock polar - Edney Type VI interference	27
2.15	Wieting's multiple shock impingement experimental setup	30
2.16	Myrabo et. al's experimental setup.	32
2.17	Girgis et. al's numerical setup.	33
2.18	A) Schlieren image of hemisphere cylinder, 70 μ s after laser energy deposition had occurred. Flow is from right to left [1]. B) Numerical schlieren image of a hemisphere cylinder with a counterflow jet. Flow is from left to right [2].	34
2.19	Laser energy deposition process	35
2.20	Schlieren by Oliveira et. al of laser energy deposition in front of a hemisphere cylinder	36
2.21	Schlieren by Adelgren et. al of laser energy deposition in front of a hemisphere cylinder	39

2.22	Schlieren by Adelgren et. al of laser energy deposition in front of a hemisphere cylinder with an Edney Type IV interaction	40
2.23	Diagram showing the flow characteristic in a counter-flow jet, produced by Finley.	43
3.1	Schematic of Hypersonic Wind Tunnel	46
3.2	Schematic of pitot rake used to calibrate Hypersonic Wind Tunnel	47
3.3	Time traces of temperature and pressures.	48
3.4	General schematic of PSP/TSP	51
3.5	Porous-based schematic of PSP/TSP	53
3.6	TSP Absorbtion/Emission Spectrum	54
3.7	Basic schlieren setup diagram	56
3.8	Experimental schlieren system diagram	56
3.9	Typical PIV system setup	57
3.10	Sample PIV velocity field	58
3.11	Sample IR image and 3-D mapping	59
3.12	Aluminium swept-cylinder Fin rendering	60
3.13	Macor swept-cylinder Fin rendering	61
3.14	Aluminium hemisphere cylinder rendering	61
3.15	Shock generator rendering	62
4.1	Baseline Surface Heat Transfer (W/m^2) along the centreline (X position in mm) of hemisphere cylinder.	65
4.2	Lift Force (N) vs Angle of Attack ($^\circ$). High $\text{Re} = 13 \times 10^6$ and Low $\text{Re} = 4.6 \times 10^6$	66
4.3	Schlieren images of hemisphere cylinder at different angles of attack. Flow is from left to right, $\text{Re}/\text{m} = 13 \times 10^6$	67
5.1	Proposed timeline of work for the coming year	69

Abstract

This report describes the research activities conducted at the University of Manchester in the first year of the project. A comprehensive literature survey of the relevant phenomena and subsequent interactions is presented along with a description of the wind tunnel facility calibration. Experimental techniques and methodologies are discussed, including reference to the range of their applicability in the campaign. Model designs, experimental setup, and preliminary analysis of the flow field are presented. The following techniques have already been used in the experimental programme: high speed schlieren photography, infrared thermography and force measurements taken from a three-component balance. The first year of the work has set the foundation for remaining steps in the second and third years.

Chapter 1

Introduction

1.1 Relevance of Proposed Research

The significance of Edney Type IV interactions, or shockwave interference heating as it was first labelled was seen in a flight test of the X-15 hypersonic research aircraft. A hypersonic research engine model was attached to the underside of the aircraft, and the oblique shock generated by the wing of the X-15 interacted with the bow shock of the engine support pylon [3]. This resulted in catastrophic damage to the pylon and incineration of part of the protective skin. A detailed description of the Edney Type IV interaction is given later, but the damage reported by Watts [3] was due to an increase in the peak heat transfer and pressure at the surface of the pylon. Controlling these interactions is a key part of moving forward in creating and maintaining a viable hypersonic program. Although no aircraft would be designed intentionally to undergo such interactions, it is entirely possible that during manoeuvres in flight, such an interaction might come to pass. Figure 1.1 gives an overview of the various shock interference patterns seen when an oblique shock intersects a bow shock. These increase in severity as the impingement point gets closer to the subsonic region of the bow shock, peaking at around the centreline, where Edney Type IV interactions are seen.

Research has shown that laser energy deposition is a method which can be used to decrease the drag on blunt bodies in hypersonic flight, and a small number of researchers have looked at applying this method to the problem of Edney Type IV interactions [1, 5]. However a clear and comprehensive evaluation of the effects of the laser discharge energy and location on the

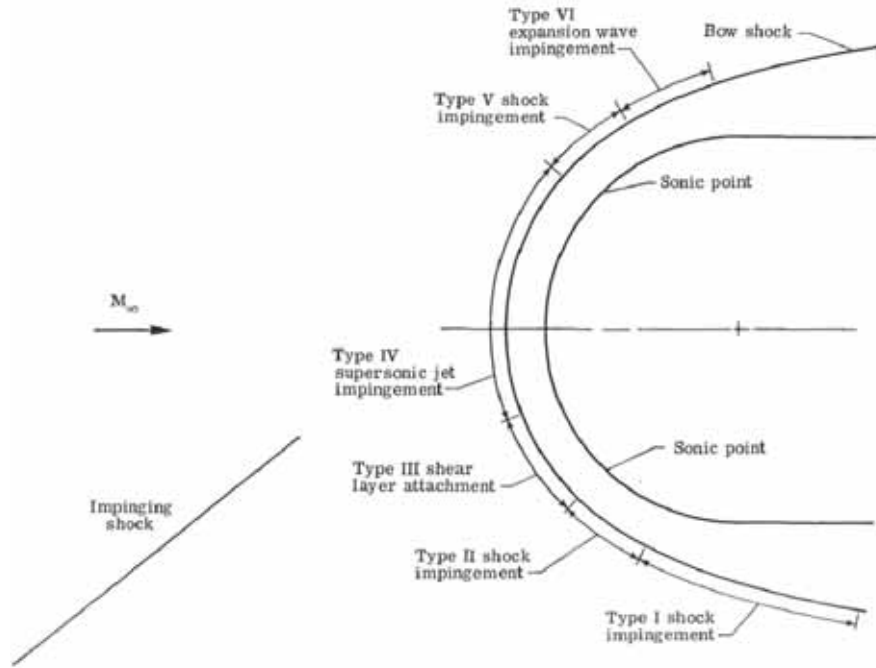


Figure 1.1: Edney interference patterns [4]. Flow is from left to right, with a hemisphere cylinder as the blunt body.

peak heat transfer and pressure associated with Edney Type IV interactions has not been undertaken. Numerical work by Anderson and Knight [6] has demonstrated that laser energy deposition has the potential to reduce the peak heat transfer by at least 30%. Other work has shown that counterflow jets are another viable method for drag reduction on blunt bodies in hypersonic flight. Research by Shang [7] has shown that drag can be reduced by up to 44 % by use of a counterflow jet from a hemisphere cylinder.

1.2 Research Objectives

The proposed research will investigate methods of controlling Edney Type IV interactions by use of energy deposition. Energy will either be deposited through focusing a laser to a small volume, causing optical breakdown of air, or by use of a pneumatic jet on the leading surface of the model. This will be accomplished by the use of two different model types: a hemisphere cylinder

which can change incidence between 20° and -20° and a swept cylinder which is able to move between sweep angles from 45° to -45° . In order to produce the controlled oblique shock necessary for the Edney Type IV interaction, a shock generator capable of changing angle between 0° and 12° will be used. These experimental models will be used inside the hypersonic blowdown tunnel at the University of Manchester. Flow diagnostic techniques will include pressure sensitive paints, temperature sensitive paints, infrared thermography, schlieren and shadowgraph imaging and particle image velocimetry.

A summary of the controlled variables is listed below:

- Hemisphere cylinder; Angle of attack: $\pm 20^\circ$.
- Swept cylinder; Sweep angles $\pm 45^\circ$, $\pm 30^\circ$, $\pm 15^\circ$ and 0° .
- Incident shock strength; Relative deflection angles of 0° , 3° , 6° , 9° and 12° .

These controlled variables have been chosen to produce good quality data which will be used in developing a methodology for optimizing the position and power of laser energy deposition, as a control technique to minimise the peak heat transfer seen in Edney Type IV interactions. In addition, the use of counter-flow jets will be investigated as a control technique, as their use in minimising drag and heat transfer on blunt bodies in hypersonic flows has been well documented.

This report outlines the first steps which have been completed in undertaking a more comprehensive investigation of energy deposition methods as used for control of Edney Type IV interactions, and briefly lists the work which will be pursued in the coming year.

1.3 Expected Project Contributions and Pay-offs

A brief summary of the expected contributions of this project to the larger body of work is itemised below.

- Development and application of laser-induced energy deposition for flow control of Edney Type IV interactions, which are critical in the design of hypersonic vehicles.
- Development and understanding of the potential of counter-flow jets for flow control of Edney Type IV interactions

- Development and population of a reliable experimental database for use in CFD code validation. As this database is generated, the researchers will naturally develop unique expertise and insights, which will be invaluable to those wishing to run CFD models of Edney Type IV interactions as well as for those wanting to run design studies as part of future collaborations.
- Collaboration with Prof. Doyle Knight at Rutgers University is planned - this will initially take the form of frequent meetings either in the United States of America or United Kingdom, with potential of a parallel computation study starting in the future.

The areas of greatest impact of this project are expected to be within the field of high speed aeronautics and the cascade of application areas. These areas include: design of more efficient, lighter, economical and environmentally friendly aerospace vehicles, transport, turbulence research, turbomachinery, aero-acoustics, suppressors and muzzle brakes design, atmospheric research, pulse detonation engines, scramjets and automobile exhaust flow fields.

Dissemination of the gained expertise will happen within the project team as well as to the wider research community. This will take the place of publication/presentation in high quality international journals, conferences and workshops, which will be pursued with due diligence and care so that the work exhibits the high standards of excellence expected from all parties.

Chapter 2

Literature Review

2.1 Introduction

Shock interference heating was first noticed when research on supersonic aircraft at Langley implied that unusually high heating rates were occurring on the wings in areas where an oblique shock impinged on a bow shock [8]. This started some preliminary investigations into the phenomenon known (then) as shock interference heating. The first of these investigations was run by Newlander [8], who looked at the interactions between shocks generated by a 16.25° wedge and a vertical cylinder. Flow speeds of Mach 2.65, 3.51 and 4.44 were used, along with boundary-layer thicknesses of 0.6 or 6 inches, and a unit Reynolds number ranging from $4.17 \times 10^6/\text{m}$ to $14.8 \times 10^6/\text{m}$. He found that the lowest speed (Mach 2.65) increased the heating rate (from the case of an infinite cylinder without shock impingement) by a factor of 1.5, whereas the highest speed, Mach 4.44, increased the heating rate by a factor of 3. The increase in boundary-layer thickness from 0.6 to 6 inches decreased the heating rate by 25%. Newlander concluded that the mechanism behind the interference heating is a vortical flow emanating from the intersection between the oblique shock and bow shock.

Carter and Carr [9] used a free flight model consisting of two cylinders with their axis perpendicular to the direction of flight. The bow shock from a hemispherical nose interfered with the bow shock of the cylinders, with the speed going up to a maximum of Mach 5.5, although data was only recorded between Mach 2.53 and 5.50. Reynolds number ranged from $1.00 \times 10^6/\text{m}$ to $1.87 \times 10^6/\text{m}$. They found quite a small increase in heating rate — up to Mach

3.23, the increase was no more than 0.5 from the laminar infinite cylinder theory, with a maximum increase to be a factor of 2, found between Mach 3.23 and 5.50.

Beckwith [10] used a wedge with a half angle of 8° to generate an oblique shock which impinged on a swept cylinder. The cylinder had two angles — 20° and 60° , with a freestream flow velocity of Mach 4.15 and a Reynolds number range of $1.6 \times 10^6/\text{m}$ to $4.0 \times 10^6/\text{m}$. Beckwith found that at 20° of sweep, the heating rate increased by a factor of 2.5, while at 60° of sweep, the heating rate only increased by 1.6. In his analysis of results, he concluded that the increase in heating rate was due more to flow separation than any negative effect of shock impingement, as the heating rate increase was higher in the case where the flow separated, according to his pressure analysis.

Jones [11] looked at a 60° swept fin with a cylindrical leading edge, mounted on a flat plate with a sharpened leading edge. The flow speed was Mach 6, at Reynolds numbers from 0.62×10^5 to 7.7×10^5 , and fin yaw ranging from 0° to 30° . He found that the heating rate increased by a factor of 3.0 at the highest Reynolds number, and was not greatly affected by the yaw angle. The largest increases in heat transfer coefficient for a given Reynolds number were found near shock-wave impingement sites. Jones suggests that the increase in heating rate may show that shock impingement aids transition to turbulence, although recognizes that other factors make it difficult to make a solid conclusion on the matter.

Hiers and Loubsky [12] used a Mach number of 14 and a Reynolds number of $3.2 \times 10^6/\text{m}$, with heat transfer measurements taken on a cylindrical leading edge swept at angles of 0° , 22.5° and 45° , secured on the plate which generated the impinging shock. Their investigation posits that the aerophysical understanding of the effects of shockwave impingement on heat transfer is well known for highly swept leading edges (Hiers and Loubsky consider 45° to be highly swept), but not for unswept edges or a shock-generator with boundary-layer separation. They found that the areas of intense heating (measured to ± 0.2 mm) corresponded to the point where the generated shockwave impinged upon the bow shock, and their results agreed with the vortical flow model presented by Newlander [8]. The highest increase in heat transfer found was seven times the theoretical value, at a sweep angle of 22.5° .

Bushnell [13] conducted two sets of experiments; one was with an unswept cylinder at Mach 8 and a shock generator at 12° to the flow. The other experiment was simulating a highly-swept (76°) leading edge with small grooves

running parallel to the chord, simulating thermal expansion joints built into the construction of a delta wing. Bushnell found that the pressure increase due to shockwave impingement was equal to the heat transfer increase, within $\pm 30\%$ of the pressure increase. He also found that there is a greater increase in heat transfer as the impingement location nears the tip or root of the leading edge. Using the vortical flow theory proposed by Newlander [8], Bushnell sees that by decreasing the distance between shockwave interaction and impingement on the surface, the diffusion of the vortices into the mixing layer is decreased, hence there are larger temperature and velocity gradients present when the flow strikes the leading edge. The addition of the grooves parallel to the chord on the delta wing were not found to make a discernable difference to the heat transfer at the leading edge.

In all of the above experimental investigations, the methodology did not try to vary the impingement location on the bow shock, nor did they do much to vary the strength of the impinging shock (perhaps by changing the turning angle). This lack of a more methodical approach meant that it was impossible to extrapolate the effects of the shock interference to understand the pressure and temperature distributions around the body. The experimental results and interpretation are able to describe what is seen, to an extent, but are unable to provide an overall understanding of the phenomenon which can be applied to more generalized flow geometry. It is also very hard to obtain a clear picture of the shock interactions described in the papers, simply because the published schlieren images are so poor. As a result of the collective methodological and equipment/technological shortcomings, the investigations did not accomplish their goal of providing a deeper understanding of shock interference heating.

2.1.1 In flight consequences of shock impingement

Watts [3] reported on the results of shock impingement on the X-15-2 research aircraft whilst in flight, specifically on a mounting pylon for a mock-up ramjet engine. The damage sustained by the ramjet pylon was enough to cause catastrophic structural failure. At a speed of Mach 6.7, the protective thermal coating was burned through, and part of the steel structure of the pylon was melted. A maximum temperature of approximately 1800°K was calculated to achieve the melting of the steel, with a sustained temperature above 1000°K for about 100 seconds. The increase in the heat transfer coefficient was calculated to be at least nine times that for a turbulent flat plate. Watts

concludes that the potential for such extreme temperatures in shock interference heating means that a more detailed understanding of the phenomenon is required, as well as great care so that the design condition does not induce these high temperature and pressures.

2.2 Edney's investigation

Barry Edney [14] undertook a detailed and thorough analysis of the shock-wave interference phenomenon, as an earlier experiment in 1964 had yielded peculiar results, and he was unable to find anything to explain the findings. Edney's study used Mach numbers of 4.6 and 7, with unit Reynolds number ranges from $4.05 \times 10^6/\text{m}$ - $4.75 \times 10^6/\text{m}$ and $1.11 \times 10^6/\text{m}$ - $7.65 \times 10^6/\text{m}$ respectively. He utilized three different models: a hemisphere-cylinder with 30 mm diameter, a flat-face cylinder with 30 mm diameter and a blunted cone-cylinder with 30 mm diameter and 5 mm tip radius. These models were manufactured from glass, and were inserted into the tunnel after it had started via an injection arm. The shock generator had turning angles of -3° , 0° , 5° , 10° and 15° . Heat transfer was measured using platinum thin film gauges, with pressure being measured both by conventional pressure tappings as well as a large transducer mounted inside a spherical model. Flow was visualized using Schlieren, oil flow and temperature sensitive paint.

Edney found that the effects of shockwave impingement depend not only on the strength of the impinging shock, but also on the geometry of the body creating the shock which is impinged on and the location of the impingement. This is not a surprising result, but, as noted at the end of section 2.1, not understanding and applying this result meant that previous studies were unable to come up with a cohesive picture of the nature of shockwave impingement. Due to the inequality of the shock strengths, a streamline through the point of impingement defines a contact surface, separating two regions which had differing velocities, temperatures and densities, but share the same pressure. Depending where the shock impinges will determine the type of interaction seen. Edney defined six different interference types, giving graphical details for freestream Mach number of 4.6, and a wedge angle of 5° . The impinged shock comes from the hemi-sphere cylinder. A diagram of the shock interactions is given for each type, as well as the shock polars. All diagrams are from Edney's paper [14].

2.2.1 Type I Interference

Type I interference occurs when the incoming shock impinges well below the sonic line. A shear layer is created at the point of impingement, separating the regions of different velocities. This shear layer will not intersect the model and thus is not involved in any local heating. As the impinging shock passes through the bow shock, it may then go on to interact with the model by promoting transition to turbulence or separation of the boundary layer. In figure 2.1, the impinging shock is denoted by the line PR.

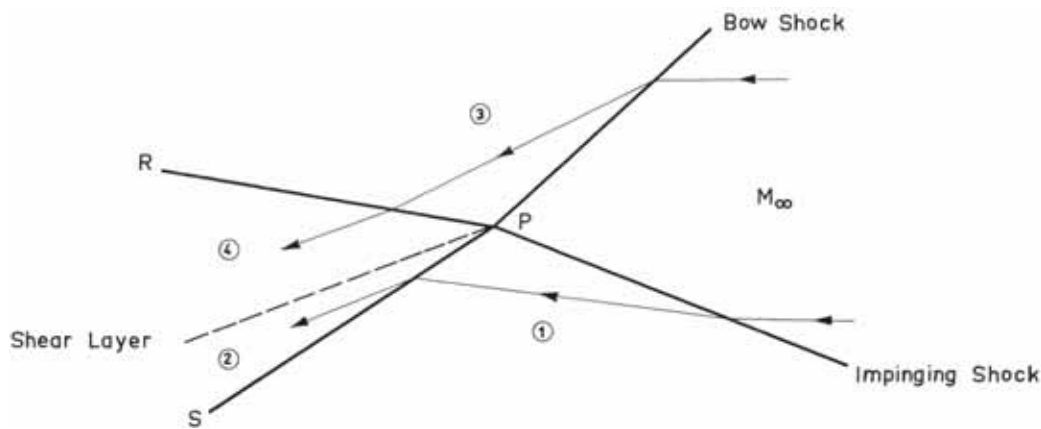


Figure 2.1: Edney Type I interference [14]. The freestream velocity is Mach 4.6, with a 5° wedge creating the impinging shock. The blunt body is a hemisphere cylinder with a radius of 30 mm. Flow is from right to left.

After the impinging shock, in region 1, the flow is at Mach 3.6 and has been deflected 10.6° upwards. In region 3, the flow after the bow shock is at Mach 3.3. The flow deflection through the bow shock directly above the impingement point is 14.8° downwards. The flow diagram displayed in figure 2.1 helps one to gain a qualitative picture of the flow, but cannot give a quantitative picture. Shock polars, which plot a curve of pressure rise against deflection angle for each Mach number, allow one to see pressure increases, flow deflections and whether the flow is supersonic or subsonic. The shock polar for this interaction is shown in figure 2.2 below. In the shock polar diagram, the effect of the shockwaves on the potential pressure increases can be seen. Even for a Type 1 interaction, which does not carry the same potency of pressure and temperature increases, the pressure increases by a

factor of 10 in regions 2 and 4. There are two intersections of the curves describing the oblique shock and bow shock, but only the high speed (weak shock) interaction will take place. This is because the weak shock requires less energy, so this solution will be desired. Also, in this specific case, the strong shock interaction would require the flow to deflect upwards, which may not be possible due to the presence of the model.

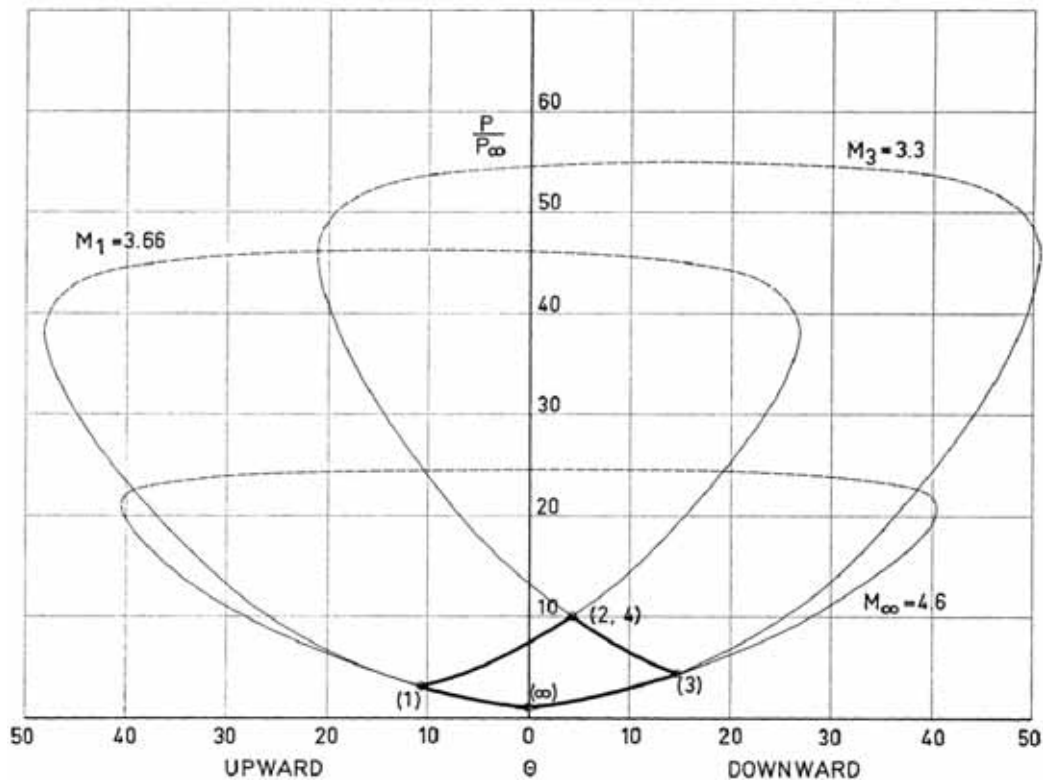


Figure 2.2: Shock polar for an Edney Type I interference [14]. The vertical axis is pressure ratio, relative the to freestream static pressure. The horizontal axis shows the flow deflection; deflection downward is displayed on the positive side, upward deflection on the negative side. Bold lines indicate flow paths, dashed lines indicate subsonic regions.

2.2.2 Type II Interference

Type II interference occurs when the incoming shock impinges just below the sonic line. The bow shock is much stronger at the impingement point, because of the greater flow deflection (In figure 2.1, the bow shock deflects the flow by approximately 14.8° , whereas the flow in figure 2.3 is deflected by approximately 37.2°). This means that two shear layers are formed, because there are two triple points. These triple points are connected by a slightly curved normal shock. The two shear layers converge, allowing the subsonic flow behind the curved shock to accelerate. The two shear layers will have vastly different effects on the model if they interact with it. Because the shear layer originating from Q (a point between the impingement point and the sonic line) separates subsonic flow and barely sonic flow, the differences in the flow characteristics across it will be minor. However, the shear layer originating at P (the impingement point separates subsonic flow from, in this instance, Mach 3.6 flow. If this shear layer were to impinge on the model, it would increase the local heating by a large amount. The shock denoted by the line QR in figure 2.3 will interfere with the boundary layer on the model, causing either transition or separation; the curved shock is denoted by the line QP in the Type II flow diagram.

From the shock polar diagram in figure 2.4, the effect of the high deflection angle by the bow shock can be seen. The smaller heart curve, denoted by $M_3 = 1.44$ can't intersect the curve defined by the oblique shock, $M_1 = 3.66$. The only way for the flow to be resolved is by joining the curves from the intersecting shocks along the $M_\infty = 4.6$ curve, in the subsonic region. This is what gives the curved shock QP, and the resulting subsonic flow. The shock polar also demonstrates the difference in pressure increase from Type I to Type II. Type I flow had a pressure increase of $\frac{P}{P_\infty} \approx 10$ and under the same operating conditions, Type II flow has $\frac{P}{P_\infty} \approx 23$.

When the point Q in figure 2.3 coincides with the sonic line, the interference type changes to Type III, and the shock denoted by QR vanishes.

2.2.3 Type III Interference

In Type III interference, the impinging shock intersects the bow shock in the subsonic region. A shear layer is again formed at the impingement point, separating subsonic flow above from supersonic flow below. Due to the position of the shock impingement, this shear layer attaches to the surface at the

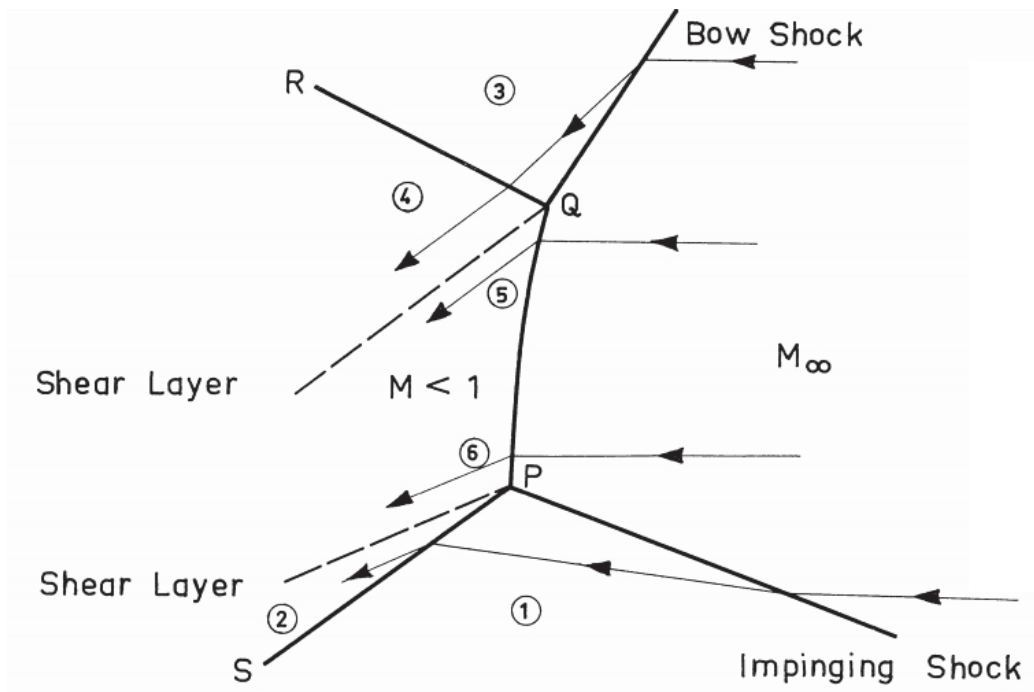


Figure 2.3: Edney Type II interference [14]. The freestream velocity is Mach 4.6, with a 5° wedge creating the impinging shock. The blunt body is a hemisphere cylinder with a radius of 30 mm. Flow is from right to left.

stagnation point of the subsonic flow around the model. An oblique shock is formed near the stagnation point in order to turn the supersonic flow away from the model. The pressure is greatly increased across this oblique shock (line RQ in figure 2.5), and since the pressure on the subsonic side of the shear layer will be relatively low, the thickness of the boundary layer is decreased near the attachment point. In addition, the Reynolds number in the supersonic flow may be such that transition occurs in the shear layer. Both of these factors help to increase the heating rate around the attachment point of the shear layer.

Edney calculated a more detailed depiction of the shock interactions for this interference type, shown in figure 2.6. What appears to be another shear layer in figure 2.5 originating at Q is actually a supersonic jet, acting as a demarcation between the subsonic region after the oblique shock RQ and the sonic flow in region 4. The greater pressure rise near the attachment point

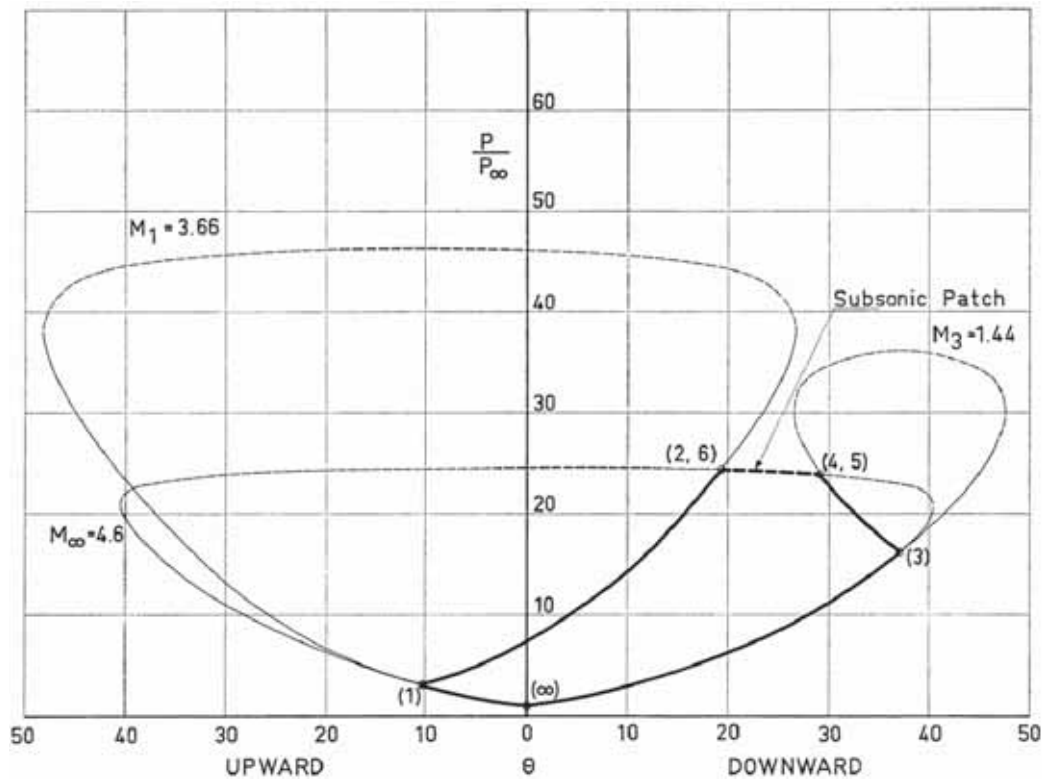


Figure 2.4: Shock polar for an Edney Type II interference [14]. The vertical axis is pressure ratio, relative to freestream static pressure. The horizontal axis shows the flow deflection; deflection downward is displayed on the positive side, upward deflection on the negative side. Bold lines indicate flow paths, dashed lines indicate subsonic regions.

causes the shock OM, helping to thin the boundary layer and thus increase the heating at the model surface. The pressure rise near the attachment point is roughly the same as the increase in pressure between the shear layer and model in region 3.

2.2.4 Type IV Interference

The transition between Type III and Type IV interference depends on the angle between the model surface and the flow direction. When the angle is high enough, the supersonic flow in region 2 can no longer be deflected

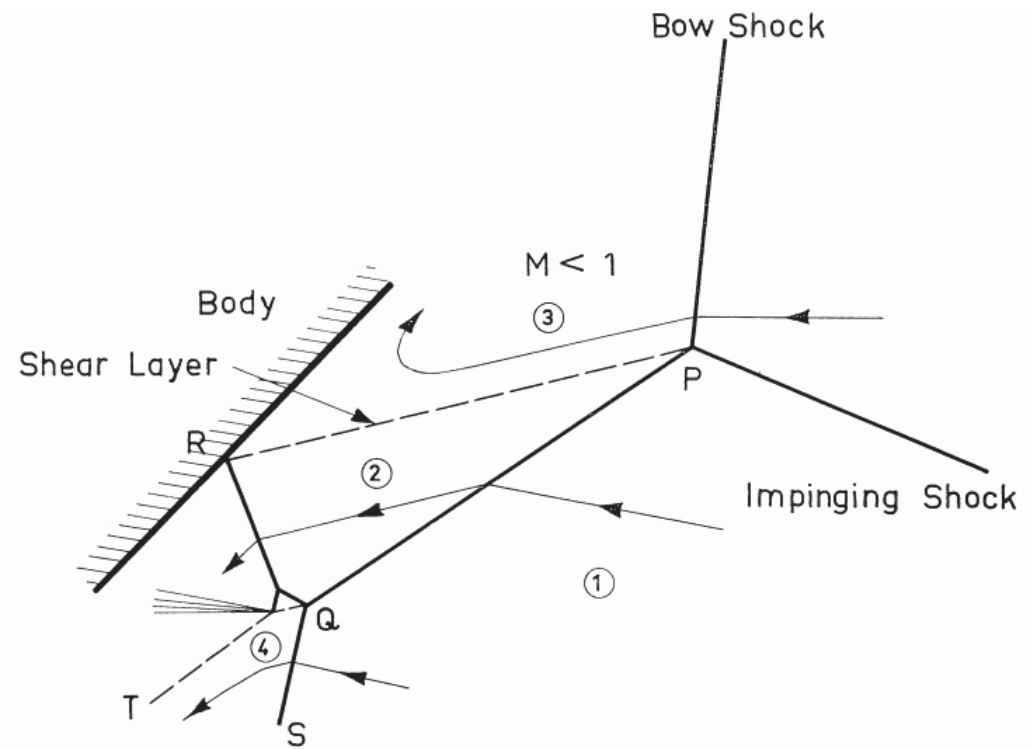


Figure 2.5: Edney Type III interference [14]. The freestream velocity is Mach 4.6, with a 5° wedge creating the impinging shock. The blunt body is a hemisphere cylinder with a radius of 30 mm. Flow is from right to left.

downwards through an oblique shock. A supersonic jet is formed (technically it is a supersonic sheet, but is referred to as a jet) which separates regions 3 and 4 (shown in figure 2.7). Because of the difference in pressure in regions 3 and 4, the jet curls up, hitting the model surface by way of a shock, denoted UV in the figure below. The angle between the jet and the body at the impingement point, the flow can either deflect fully upwards, or separate into two streams: UX and VY. The supersonic jet is bounded by a shear layer on either side and starts with the flow from region 2 being compressed by the shock RQ, before moving through a series of expansion fans and compressions, roughly alternating between two Mach numbers, denoted M_5 and M_6 . The pressure of impingement here can be catastrophically high, as the pressure in region 5 is already very high and $M_5 > 1$. For the fairly low

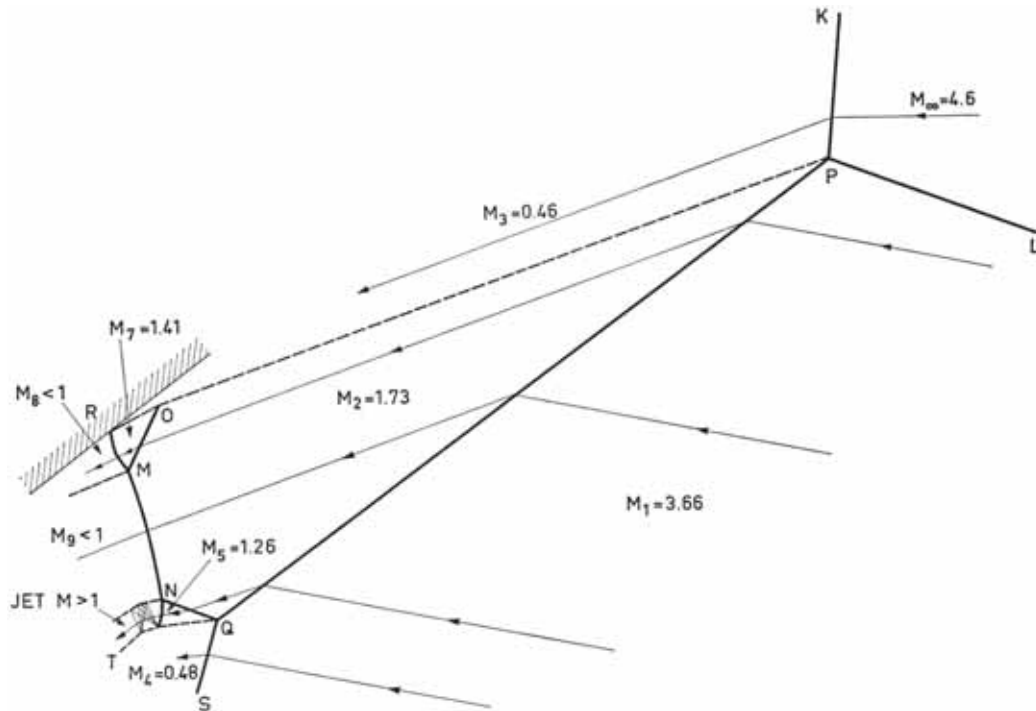


Figure 2.6: Detailed depiction of Edney Type III interference [14]. The flow conditions are the same as in figure 2.5.

speed case shown in figure 2.7, $M_5 = 1.26$. Edney shows that the maximum value of M_5 is 2.6, for $M_\infty < 20$ and $\gamma = 1.4$.

The shear layer denoted by PRV transitions to turbulence first - at the latest, it has reached a fully turbulent state by the shock RQ. However, the lower shear layer, denoted by QTV, is laminar, up to the point T, where the expansion waves help it to transition to turbulent. The amount of curl up experienced by the supersonic jet increases as the impingement point moves up the model and the thickness decreases as well. The thickness of the supersonic jet will affect the increase in local heating, but Edney was not able analytically to predict the peak heat transfer for all cases. He measured the peak heat transfer to be approximately nine times that expected from the conditions in region 2, with the pressure increase from region 2 being about 4.5 times.

Either side of the supersonic jet, the flow deflects upwards or downwards,

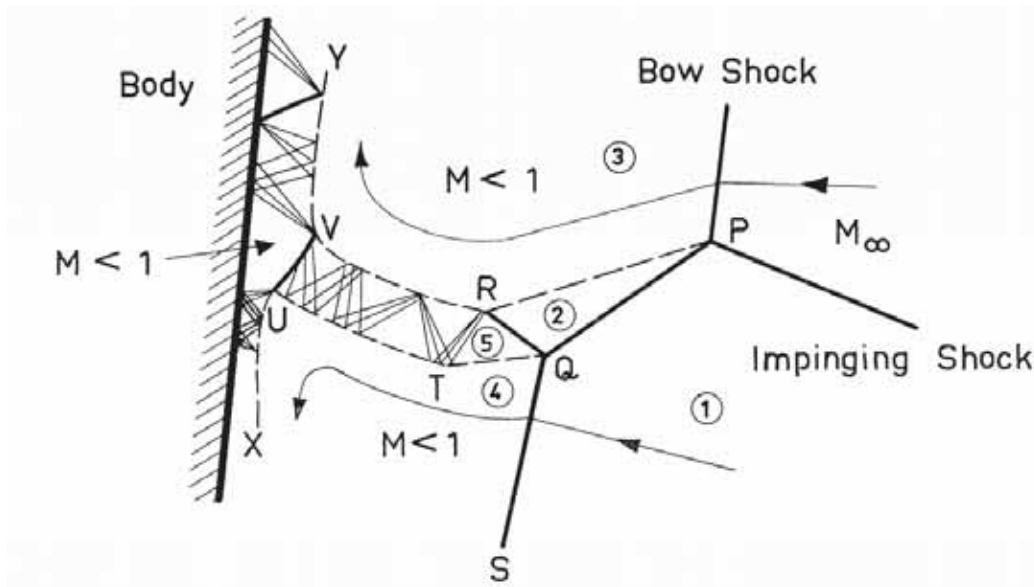


Figure 2.7: Edney Type IV interference [14]. The freestream velocity is Mach 4.6, with a 5° wedge creating the impinging shock. The blunt body is a hemisphere cylinder with a radius of 30 mm. Flow is from right to left.

depending on the position. Type IV interference is responsible for the highest pressure and temperature increases seen experimentally and in flight - the catastrophic destruction observed by Watts [3] was almost certain due to a Type IV interference pattern. Figures 2.8 and 2.9 below are more detailed analyses that Edney calculated for Type IV interference. Both of them demonstrate the cyclical nature of the flow speed in the supersonic jet by giving the actual numbers for M_5 and M_6 . In figure 2.9, despite having the same wave angle for the impinging shock, the resulting shockwave system looks more stretched out than the lower speed diagram in figure 2.8. In these cases, the difference can be attributed to a lower pressure differential between regions 3 and 4 in the higher speed case.

The shock polar in figure 2.10 is valid both for Type III and IV interference patterns and displays the pressure increase found in region 5. The curves demonstrate the reason for the large pressure increase; the shock polar for Type I interference (shown in figure 2.2) has a similar turning angle for the bow shock, but because the oblique shock impinges in the subsonic region, the pressure in the impact region is approximately eight times higher.

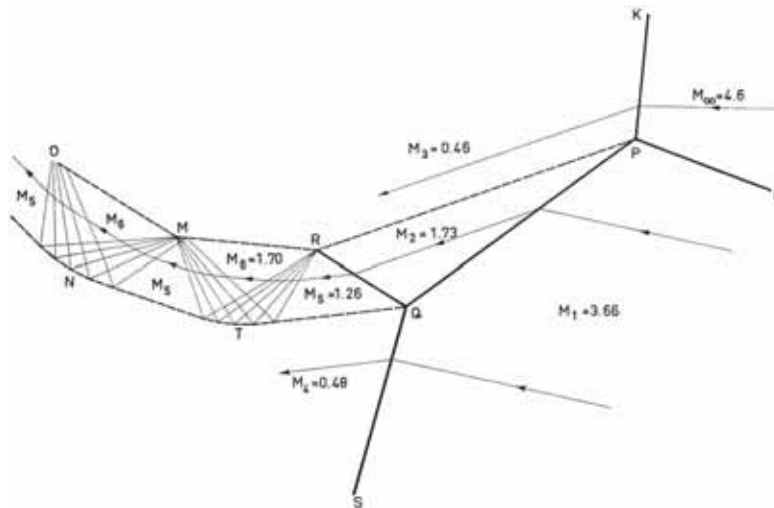


Figure 2.8: Detailed depiction of Edney Type IV interference [14]. The flow conditions are the same as in figure 2.7.

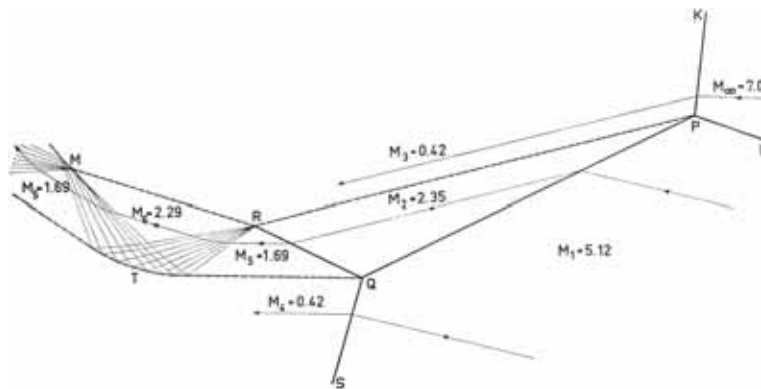


Figure 2.9: Higher speed detailed depiction of Edney Type IV interference [14]. The freestream velocity is Mach 7.0, with a 5° wedge creating the impinging shock. The blunt body is a hemisphere cylinder with a radius of 30 mm. Flow is from right to left.

2.2.5 Type V Interference

Type V interference occurs when the oblique shock impinges just above the upper sonic line of the bow shock. Although analogies can be drawn between

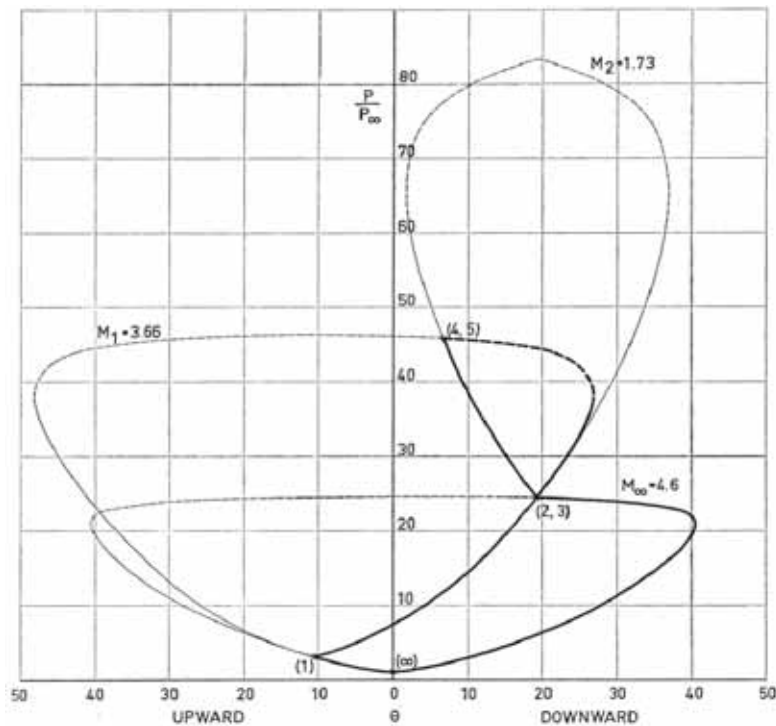


Figure 2.10: Shock polar for an Edney Type III/IV interference [14]. The vertical axis is pressure ratio, relative to the freestream static pressure. The horizontal axis shows the flow deflection; deflection downward is displayed on the positive side, upward deflection on the negative side. Bold lines indicate flow paths, dashed lines indicate subsonic regions.

Type V and Type II interference, there are significant differences between them. In Type V interference, a supersonic jet is formed at the impingement point, which has the characteristics of alternating expansion and compression waves found in the Type IV jet, but this one is much thinner. As in Type II interference, a shear layer is formed at the point Q (similar to Type II, lies between the sonic point and the impingement point). This shear layer converges with the supersonic jet at the point where the subsonic flow in region accelerates from subsonic to supersonic. When the shear layer and supersonic jet meet the body, they do not have the same effect on the heat transfer as for Type IV interference. What will have a noticeable effect on the heat transfer will be the shock QR, as seen in figure 2.11. The strength

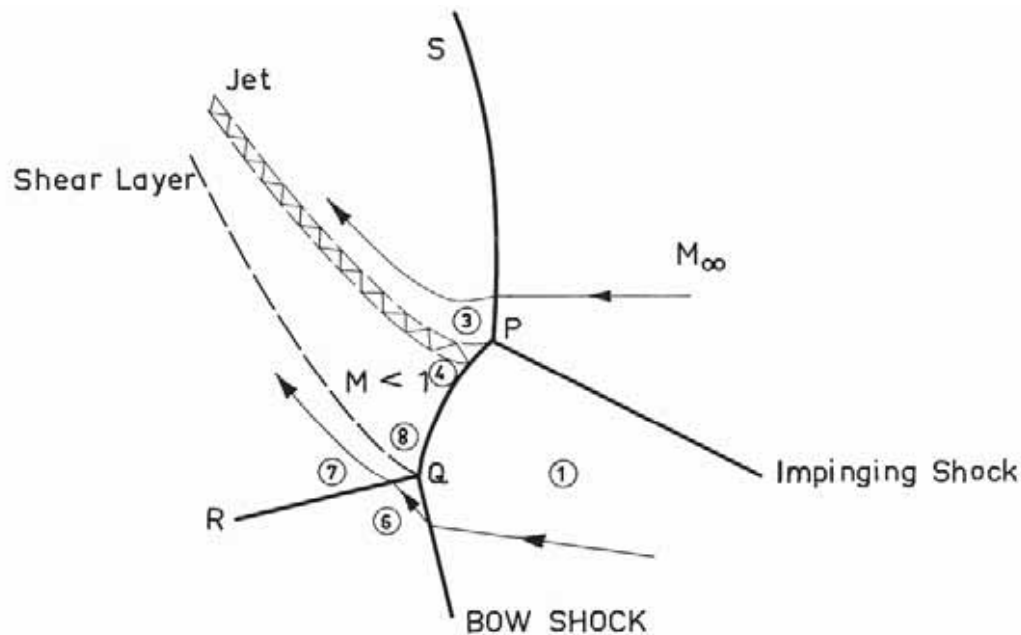


Figure 2.11: Edney Type V interference [14]. The freestream velocity is Mach 4.6, with a 5° wedge creating the impinging shock. The blunt body is a hemisphere cylinder with a radius of 30 mm. Flow is from right to left.

of this shock is such that it can promote transition to turbulence within the boundary layer or even separation.

The shock polar for Type V interference is shown in figure 2.12. This diagram demonstrates two key attributes of the interaction pattern. Firstly, the flow after the oblique shock has both upwards and downwards deflection, depending on which part of the shock system it interacts with. This can be seen by the fact that the heart curve for the oblique shock flow is entirely in bold. Secondly, despite having the same downward deflection flow as the shock polar for Type III/IV interferences (figure 2.10), the impact on the heat transfer is not anywhere near as great. This is due to the shear layer/supersonic jet not impinging on the model in the same flow speed location (ie: not in the subsonic region).

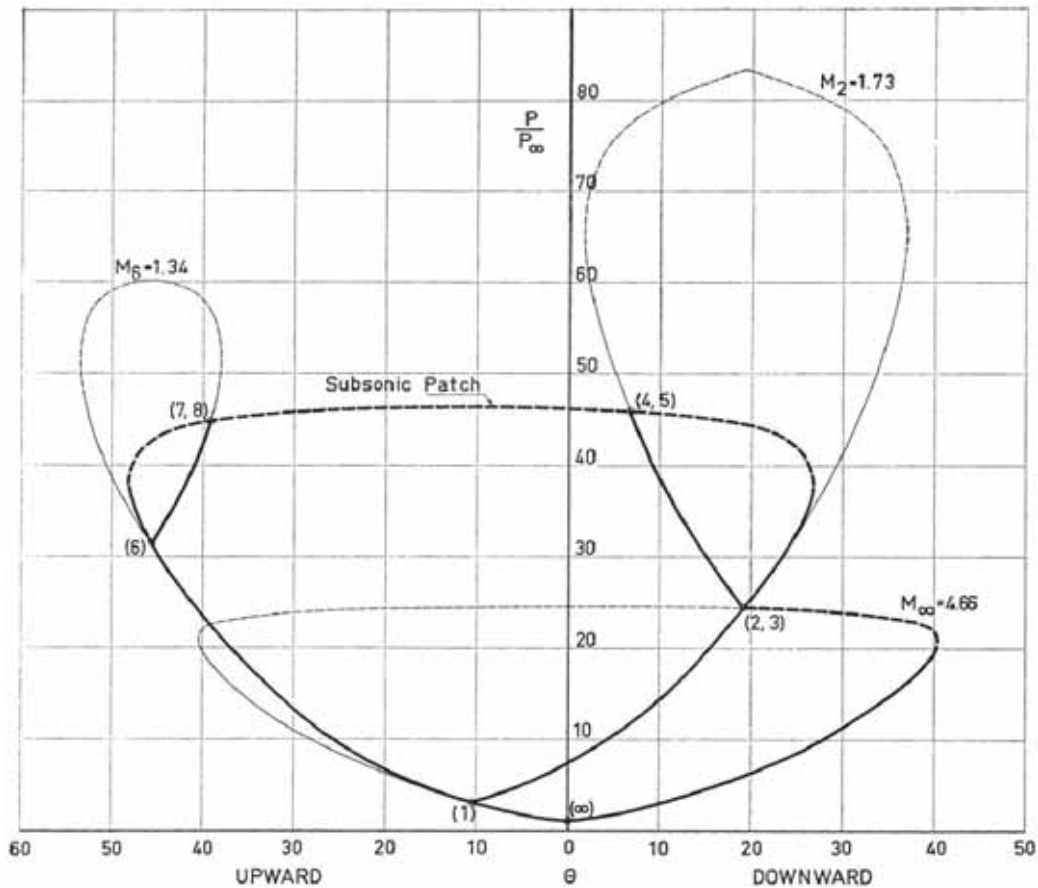


Figure 2.12: Shock polar for an Edney Type V interference [14]. The vertical axis is pressure ratio, relative the to freestream static pressure. The horizontal axis shows the flow deflection; deflection downward is displayed on the positive side, upward deflection on the negative side. Bold lines indicate flow paths, dashed lines indicate subsonic regions.

2.2.6 Type VI Interference

Type VI interference happens when the oblique shock impinges well above the upper sonic line of the bow shock. Below the impingement point P, the bow shock is undisturbed from what it would be at the free stream conditions of region 1 in figure 2.13. As with all other interference patterns, there is a shear layer originating at the impingement point. However there also is an

expansion from region 2 (after the bow shock, below the impingement point) to region 4 (after bow shock, starting at impingement point, bounded by the shear layer). Edney found that the shear layer and expansion fan had no noticeable effect on the heat transfer at the surface of the model (even assuming they interact with the surface). The only factors which change the heat transfer are those which would be expected in normal flow (Reynolds number, surface condition, etc), as they indicate flow regime and the transition point in the boundary layer.

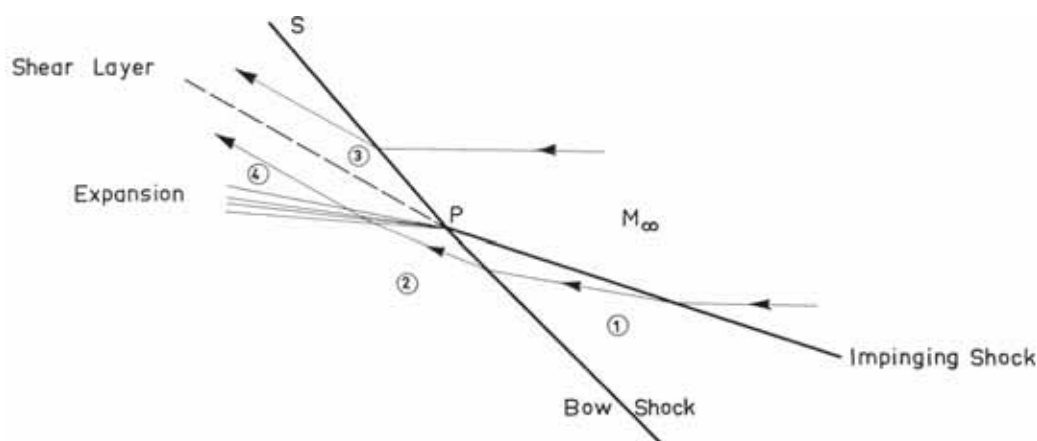


Figure 2.13: Edney Type VI interference [14]. The freestream velocity is Mach 4.6, with a 5° wedge creating the impinging shock. The blunt body is a hemisphere cylinder with a radius of 30 mm. Flow is from right to left.

The shock polar for Type VI is shown in figure 2.14. This diagram shows that Type VI interference is significantly different from every other interference type in that it only deflects flow upwards. This fact also means that Type VI interference is a relatively simple pattern. It also marks the first time flow jumps across the curves - showing the expansion from region 2 to region 4 flow. If point 2 were to move upwards along the curve $M_1 = 3.66$, it would demonstrate that the bow shock below the impingement point is increasing in strength, due to the impingement point moving downwards. Once the flow has progressed along the $M_1 = 3.66$ curve so that it is past the intersection point with the $M_\infty = 4.6$ curve, the expansion can no longer occur, and Type V flow will be seen instead.

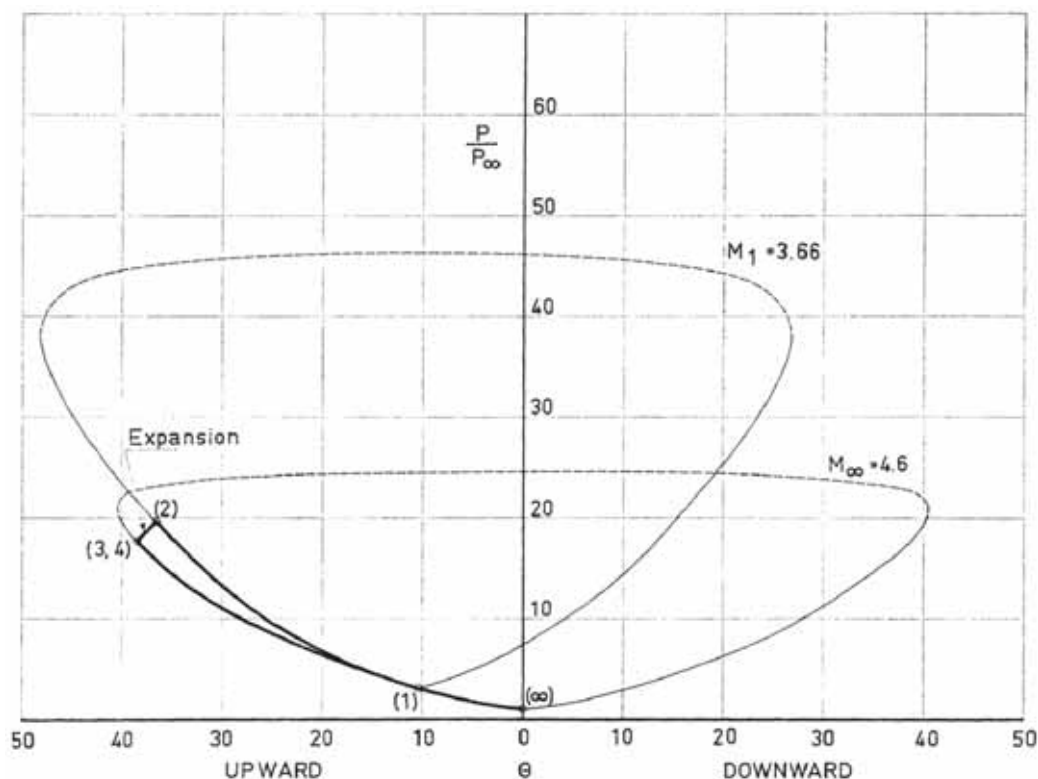


Figure 2.14: Shock polar for an Edney Type VI interference [14]. The vertical axis is pressure ratio, relative to the freestream static pressure. The horizontal axis shows the flow deflection; deflection downward is displayed on the positive side, upward deflection on the negative side. Bold lines indicate flow paths, dashed lines indicate subsonic regions.

2.2.7 Edney's Findings

After characterizing each of the six different interference types qualitatively (with some quantitative information given as well), Edney gave a more general description of the types of interactions seen. Types I, III and VI show weak shock interactions, while Types II, IV and V demonstrate strong shock patterns. Edney noted that there are four different physical phenomena which factor into the increase in heat transfer and pressure seen in shock-shock impingement. They are: shock-boundary layer interactions (seen in Types I, II and V), shear layer stability and attachment (Type III), impinge-

ment of supersonic jet (Type IV) and vorticity amplification (Types IV and V). When considering a swept fin with shock impingement, the sweep angle was observed to be a factor in determining the interference type as well. Edney found that Type IV interference was seen for low or zero sweep angles, Type V for angles up to 30° and Type VI for angles above 30° . Even so, he stated that this area of shock interference required much more study, both experimental and numerical. Figure 1.1, shown in section 1.1 gives an overview of the demarcations along a bow shock for the different interference types.

2.3 Edney Interactions - Further studies

Having now classified what the key elements are in shockwave interference heating, and the interaction type which will give rise to the catastrophic failure seen by Watts [3], more studies of Edney interactions were undertaken, both experimentally and numerically. At first, these studies sought to provide a more comprehensive framework of understanding of the phenomenon itself, but as time progressed, passive and active control methods, especially for type IV interactions, have been investigated as well. One of the first attempts at a parametric study was undertaken by Keyes and Hains [4], using a Mach number range of 6 to 20, unit Reynolds number varying from $3 \times 10^6/\text{m}$ to $25.6 \times 10^6/\text{m}$ and four different test gases. The gases used were air, nitrogen (these both have $\gamma = 1.40$), helium ($\gamma = 1.67$) and tetrafluoromethane ($\gamma = 1.27$). As well as using different test gases, they also used four different models for the shock to impinge upon: 50 mm hemisphere cylinder, 25 mm hemisphere cylinder, 25 mm swept cylinder fin and a 30° wedge. Type IV interference patterns were found for all models - air at Mach 6 was used in tests for each model apart from the 25 mm hemisphere cylinder. However, because they were not able to obtain different Mach numbers for the same test gas, it is hard to define a trustworthy trend from their results. Their calculated results, using code presented by Morris and Keyes [15], are only consistently accurate for air.

Wieting and Holden [16] varied Reynolds number, Mach number and shock strength, focussing on the effect this had on Type IV interference. Mach numbers of 6.3, 6.5 and 8.0 were used, with Reynolds numbers/metre of $1.6 \times 10^6/\text{m}$ (Mach 6.5), $2.5 \times 10^6/\text{m}$ (Mach 6.3 and 8), $5.08 \times 10^6/\text{m}$ ($M = 6.3, 8$) and $12.5 \times 10^6/\text{m}$ ($M = 6.3, 8$). All tests were conducted in air, total

temperatures ranging from 1200 to 1900 K. The shock strength was varied by changing the angle of the shock generator - angles of 10° , 12.5° and 15° were used. Wieting and Holden found that the pressure rise increased with increasing shock strength, but the same trend didn't hold for the heat transfer increase. Edney [14] stated that the square of the heat transfer increase due to a Type IV interference is proportional to the peak pressure amplification multiplied by the ratio of the radius of the body to the jet width. For the experiments conducted by Wieting and Holden, the jet width increased with shock strength faster than the pressure ratio, so at the highest shock strength (15° shock generator), the heat transfer decreases compared to the value from the 12.5° shock generator. They found that the peak pressure and heat transfer ratio increased with Mach number, but that the size of the interaction region with the surface decreased. Changing the Reynolds number was found to have no real impact on the amplification of heat transfer and pressure. The only effect it did have was to change the shear layer from laminar to turbulent. In Wieting's doctoral thesis [17], which is the precursor to the paper published by Wieting and Holden, he recommends that future investigations take high frequency samples (the data presented was limited to 20 Hz), that three dimensional effects be considered, non-intrusive measurement techniques be utilized (especially helpful for computational fluid dynamics) and that the effectiveness of cooling techniques be considered under shockwave interference conditions, especially Type IV.

Holden, Moselle and Lee [18] furthered the work of Wieting and Holden [16], who had three main areas of investigation - single shock impingement, double shock impingement and effect of sweep on shock impingement. They improved on [16] by using a larger range and number of Mach numbers - 6.5, 8.0, 11.7, 15.6, 16.3, 18.9, each of which had different Reynolds numbers. Their goal was to investigate the effect of Mach number change and flow regime on the peak heating under Type III and Type IV interference. At the lower two Mach numbers, the shear layers/jet were turbulent. At Mach 11.7 and 16.3, some of the interactions were characterized as transitional, and between Mach 11.7 and 18.9, the interactions were classified as fully laminar. Secondly, they were interested in seeing the difference in interference due to multiple oblique shocks interfering with the bow shock - this would roughly simulate an oblique shock generated due to a double ramp. Their results show that with an increase in Mach number, there is a corresponding increase in the peaks for pressure and heating at the model surface. Turbulent or transitional flows enhance the heating, due to the extra heat transfer from

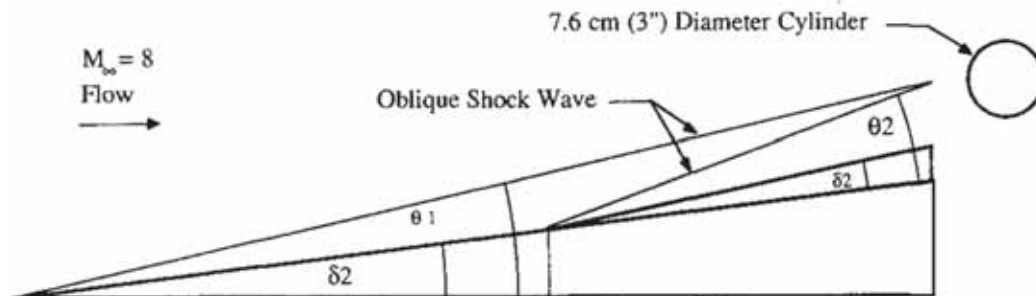


Figure 2.15: Experimental setup of Wieting's [19] multiple shock impingement experiments. Flow is from left to right.

the turbulence in the stagnation region; laminar flows do not show the same amount of enhancement. Holden et al. believe the decrease in heating for laminar flows is due to the stronger viscous effects, particularly in the region of the jet. Multiple shocks impinging on the bow shock either side of the sonic line reduce the peak heating below that of a single shock of similar strength. However, when two shocks coalesce before impingement, this generates the largest peak heating that Holden et al. saw experimentally.

Wieting [19] continued Holden et al's work [18] on multiple shock-shock interactions, with flow conditions at Mach 8 and a Reynolds number per metre of $4.9 \times 10^6/\text{m}$. His motivation was to provide insight into the complex multiple shock interactions in hypersonic engine design - specifically the double compression ramp and the leading edge of the cowl. The experimental setup Wieting used is shown below in figure 2.15.

The first generator angle, δ_1 , was 7.5° for the double ramp cases, and the second angle, δ_2 was 5 or 6° . Wieting also ran a case with a generator angle of 12.5° , conditions identical to a run with the 7.5° ramp and the 5° ramp. He found, as Holden et al. [18] did, that coalesced incident shocks increase the peak heating on the model surface, with multiple impinging shocks decreasing the peak heating. The comparison between the single ramp and double ramp with total turning angle of 12.5° showed that the coalesced shock had peak heating which was 21% higher. Typical multiplication values found for Type IV interference with a coalesced impinging shock were 13 times higher than stagnation for pressure and at least 30 times higher for heating. Wieting concluded that one way to reduce the destructive capability of Type IV

interactions would be to compress the impinging shock through a number of small angled wedges into a number of shocks that would be hindered from coalescing.

As experimental studies of the Edney interactions were taking place, researchers [20–34] began to undertake numerical simulations as well. At first, the researchers were able only to confirm what previous experimental work had done, essentially demonstrating that it was possible to perform reasonably accurate numerical simulations of Edney interactions. As computing power progressed, along with better numerical models and theoretical understanding of the Edney type phenomena, the numerical studies were increasingly able to give physical insight into the mechanisms behind Edney type IV interactions. The most recent work demonstrates that the use of numerical analysis in conjunction with good experimental results is a viable path forward to greater understanding.

From the beginning, Edney Type Interactions, specifically Edney Type IV interactions, have been an object of much research. At first, the objective was merely to characterize and understand the potentially catastrophic phenomenon, but as the understanding grew, researchers started to glimpse ways to mitigate the destructive power of these shockwave interactions.

2.4 Control Techniques - Energy Deposition

Energy deposition, whether by laser, plasma or electric discharge has been shown to decrease the drag in front of a blunt body in supersonic flow. Numerical work by Riggins et. al [35, 36] demonstrated that energy deposition in front of a hemisphere cylinder at hypersonic speeds can reduce the baseline drag by as much as 50%. They calculated an efficiency (thrust power reduction over power input) over 30 for their cases. Soloviev et. al. [37] found that using plasma filaments for supersonic flow control past a cone cylinder was not as effective as using a stationary energy deposition - their calculated efficiency rose to a maximum of 1.5 at Mach 5, and only became greater than unity at Mach 2.5. Bushnell [38] reported work from Yuriev et. al and Zaidi et. al (the original papers were unavailable to the current author) which indicated that pulsed energy deposition was more effective than continuous at reducing drag.

Myrabo et. al [39] conducted experiments using electric discharge in flow at Mach 10, with a disk-shaped model of radius 76 mm. They used a

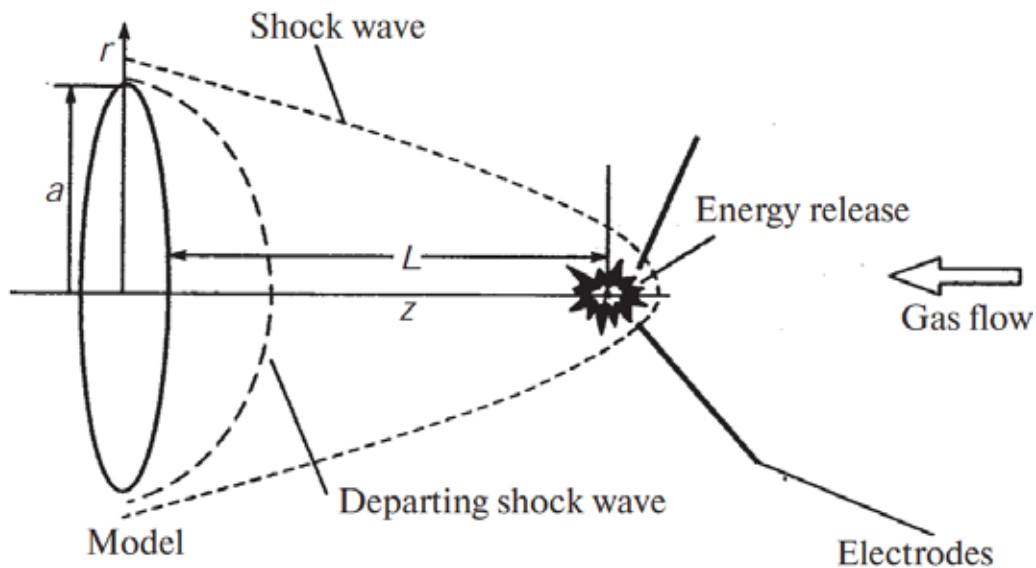


Figure 2.16: Experimental setup of Myrabo et. al's [39] energy deposition experiments. Flow is from right to left.

shock tunnel with a run time of 1-4 ms, whereas the discharge gave constant current and voltage for at least 13 ms. In this setup, the energy addition can be considered to be continuous. Additionally, although they were able to measure the total electrical power, they could not get a measurement of the power input to the flow. They estimated that approximately a quarter of the total electrical power in any situation was actually delivered to the flow; this was tested at powers ranging from 7.5 kW to 62 kW. The effectiveness of the drag reduction ranged from 5.4 to 7.7, depending on the amount of electrical input. However, the greatest effectiveness in drag reduction doesn't come at the highest amount of electrical energy, the reasons for which are not adequately address by Myrabo et. al. An image of their experimental setup is shown in figure 2.16.

Although the flow in figure 2.16 is specifically for energy deposition by electrical discharge, it demonstrates roughly what the setup would appear like for other types of energy deposition, notably laser energy deposition. One of the parameters which can be seen from the image is the distance from the model that the energy is deposited, L . Myrabo et. al attempted to provide some quantifiable insight into this parameter, but could only give

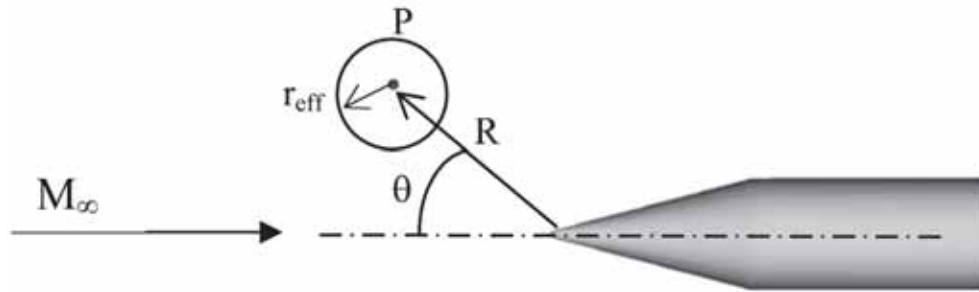


Figure 2.17: Numerical setup of Girgis et. al's [40] energy deposition studies. Flow is from left to right. The dark spot in the middle of the circle denotes the location of energy deposition.

some guidelines for continuous electrical discharge. Numerical work done by Girgis et. al [40] investigated the effect of the position of energy input by looking at off-axis addition of heat to Mach 3 flow around a cone cylinder. By situating the energy deposition at angle and distance above the centre axis of the cone (shown in figure 2.17), Girgis et. al were able to obtain not only a drag reduction for the body, but also an increase in lift. These effects were found to increase in strength as the Mach number increased.

Apart from the recent studies [39,40] briefly discussed, not much work has come to light regarding the optimization of the location of energy deposition, whether off-axis positioning or the centreline distance from the model. These important parameters remain a key component in the use of energy deposition for drag reduction which require further quantification.

Other work has shown that counterflow jets are another viable method for drag reduction on blunt bodies in hypersonic flight. Research by Shang [7] has shown that drag can be reduced by up to 44 % by use of a counterflow jet from a hemisphere cylinder. Similar results have been reported by Shang et. al [41], Fomin et. al [42], Venukumar et. al [43], Daso et. al [44] and Shah et. al [2]. Schlieren produced by Daso et. al [44] and Shah et. al [2] demonstrate that a counterflow jet has a disruptive effect on the bow shock similar to that seen by laser energy deposition. A comparison between the disruptive effect of laser energy deposition and a counter flow jet is seen in Figure 2.18. Their work also saw a reduction in the heat transfer to the blunt body.

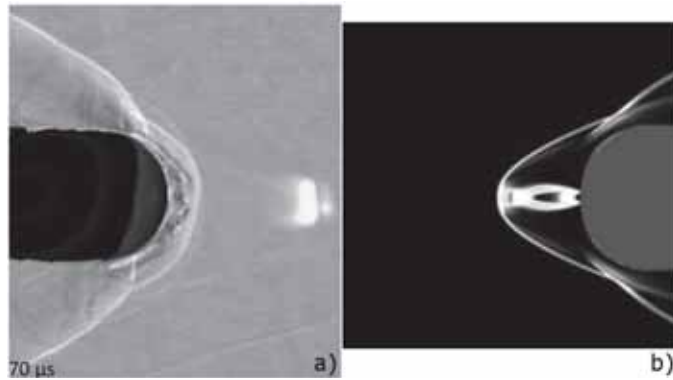
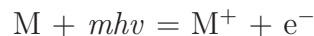


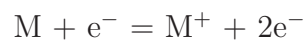
Figure 2.18: A) Schlieren image of hemisphere cylinder, 70 μs after laser energy deposition had occurred. Flow is from right to left [1]. B) Numerical schlieren image of a hemisphere cylinder with a counterflow jet. Flow is from left to right [2].

2.4.1 Laser Energy Deposition

When a high-powered pulsed laser is focused to a small volume in air or onto a target surface, an energy release occurs, ejecting plasma and a pressure wave. This has been used in a number of different aerospace applications - although the main one of interest is for flow control, specifically drag reduction [35,36]. The following steps occur in laser energy deposition: multiphoton ionization release of electrons, gas ionization in the focal region due to the cascade release of the electrons, absorption of the laser energy by plasma, rapid plasma expansion, formation of a detonation wave, and movement of the resulting shockwave into the surrounding gas [5]. Multiphoton ionization describes the ionization of a molecule by a number of photons, such that electrons are emitting. This is most commonly described by this reaction:



In this equation, $m h\nu$ represents the energy, $h\nu$, from m photons, added to a Molecule, which then ionizes the molecule and releases electrons. These electrons then absorb the laser energy, and if they absorb more energy than the ionization level of the gas, they release more electrons - known as cascade release. This reaction is described by the following reaction:



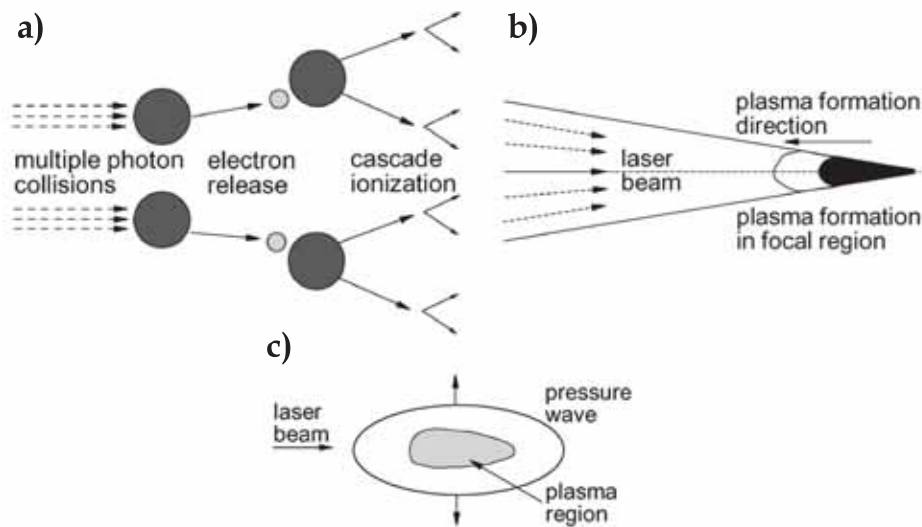


Figure 2.19: Diagram of the process of Laser energy deposition. In a), the multiphoton ionization, leading to the electron cascade can be seen. The absorption of the laser energy by the resulting plasma is seen in b), and finally, the build-up and subsequent release of pressure through a pressure wave can be seen in c). [5]

The ionized molecules result in a plasma being formed, which subsequently absorbs the laser energy - the region absorbing the energy is larger than the initial focal volume. Once the pulse has ended, the plasma, which has been heated considerably by the addition of the laser energy, recombines. Due to the increase in heat, the pressure also has increased, which is released through a pressure wave. The process is illustrated in figure 2.19.

Using laser energy deposition to reduce drag has been numerically and experimentally investigated by a number of researchers. Within this field of study, some of the key parameters to consider are: laser pulse energy, pulse width and the wavelength of light. Work by Oliveira et. al [45] was conducted at Mach 7, using a laser with 7 J/pulse, a pulse width of 120 ns at 1064 nm. They found that the laser disrupted the flow around a hemisphere cylinder for approximately 50 μ s. They also theorized that were the laser direction to be parallel to the flow, this disruption time could be increased to approximately 140 μ s. Their results did not quantify the amount of drag reduction - instead they demonstrated the disruption to the bow shock using a series of schlieren

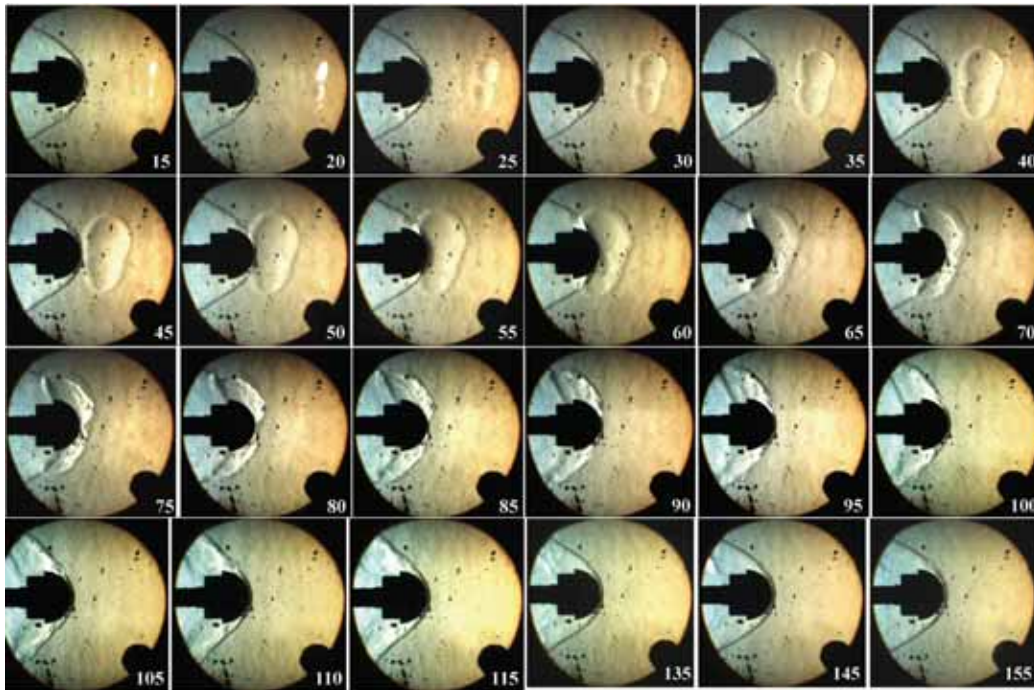


Figure 2.20: Schlieren images taken by Oliveira et. al [45] of laser energy deposition in front of a hemisphere cylinder in Mach 7 flow. The numbers under each figure refer to the number of microseconds after the laser had been fired.

images, which are copied below as figure 2.20. The timestamps under each figure refer to the number of microseconds after the laser had been fired.

In figure 2.20, the shockwave resulting from the energy deposition can be seen as early as $20 \mu\text{s}$ after firing. The shockwave grows, expanding so that two separate shockwaves coalesce. By $50 \mu\text{s}$ after the laser has fired, the shockwave has reached the bow shock, and has disrupted it, lowering the pressure on the leading surface. This continues until at least $100 \mu\text{s}$, and even by $145 \mu\text{s}$, the expansion waves behind the leading surface still have not returned.

Other researchers did quantify the drag reduction found with laser energy deposition. Sakai et. al [46] used a laser with 450 mJ/pulse , 9 ns pulse width in Mach 3 flow, in front of a square surface. A single laser pulse was used for each measurement run. An initial sharp increase in pressure was found, followed by a drastic decrease, which lasts for approximately $80 \mu\text{s}$. During

the 80 μs , an average drag reduction of approximately 86% was found. The initial increase in pressure is due to the shockwave reflection off the flat wall, with the decrease that follows resulting from the bow shock deforming and mixing with the high temperature region of the energy deposition. Approximately 250 μs after the laser has fired, the flow returns to the undisturbed state. The results presented by Sakai et. al [46] have the potential to provide some insight the mechanics of drag reduction by laser energy deposition, but many of the processes described by them are too dependent on their flat geometry, which makes it difficult at best to apply their understanding to a more generalized case. Work by Sasoh et. al [47] used a similar geometry to Sakai et. al [46], but with a laser that had a pulse energy of approximately 12 mJ, a pulse width of 10 ns and a repetition rate of 10 kHz. Under these conditions, Sasoh had hoped fully to disrupt the bow shock, since the work of Sakai et. al [46] and Oliveira et. al [45] had demonstrated that the flow took approximately 100 μs to return to the original state after the laser pulse. However, Sasoh et. al didn't see the same amount of drag reduction as Oliveira et. al and Sakai et. al, partially due to the great reduction in pulse energy used. Even so, they observed a time averaged drag reduction of 3%, with an overall efficiency of 10 (power saved over power input). This result highlights one of the issues of high-powered lasers - high pulse energy means a fairly low repetition rate, otherwise the system will catastrophically overheat.

As can be seen by the above work, laser energy deposition can play a key role in reducing drag at supersonic and hypersonic speeds. It even could be used to provide greater lift to the aerobody whilst still reducing the drag, as shown by [40]. However, some areas still remain where greater understanding is needed. A recent survey by Knight [48] highlighted two such areas. Firstly, many of the simulations performed assume ideal gas behaviour, which doesn't account for effects like the dissociation of oxygen. Secondly, although many researchers give a value for the efficiency, this is not taking into consideration the extra size and weight which would be required to implement the devices and their complex control systems on actual aerobodies.

In parallel with research into using laser energy deposition to reduce drag, work has been done looking at the application of laser energy deposition to controlling and mitigating the high pressure and temperature increases associated with Edney Type IV interactions. Kandala et. al [5] noted in their paper that Edney Type IV interactions could be controlled using laser energy deposition, but did not provide numerical data to back up their assertion.

Adelgren et. al [1] looked at Mach 3.45 flow, using a Nd:YAG laser with a pulse width of 10 ns, a wavelength of 532 nm and a pulse energy between 13 mJ and 283 mJ. They achieved a surface pressure reduction of approximately 30%, because of the way the laser energy deposition thermally interacts with the bow shock and oblique shock upstream of the hemi-sphere cylinder. Adelgren et. al also ran experiments with just the hemi-sphere cylinder, allowing a comparison of bow shock mitigation with and without the Edney Type IV interaction. Without the Edney Type IV interaction, the pressure reduction was approximately 40%. In figure 2.21, the temporal change in the bow shock due to laser energy deposition can be seen.

These images produced by Adelgren et. al [1] give some more helpful details which are not found in the work of Oliveira et. al [45] in the interaction between laser energy deposition and drag reduction in front of a blunt body. The image after 50 μ s shows the interaction of the three dimensional thermal region with the three dimensional bow shock of the hemisphere, causing streamwise vorticity.

Even more useful, however, are the images Adelgren et. al. [1] produce of how laser energy deposition interacts with an Edney Type IV interaction. A set of images detailing the transient interaction phenomenon can be seen in figure 2.22.

In these images, the laser energy spot first interacts with the impingement point, then continuing to disrupt the jet structure and bow shock. The thermally heated region which gives rise to the initial increase in heat transfer noted by Kandala et. al [5] can be seen after 40 μ s, remaining for approximately 10-15 μ s. The disruption of the bow shock by the deposited laser energy lasts for about 70-80 μ s, a similar timeframe seen for disruption of the bow shock without an Edney Type IV interaction. By 160 μ s after the laser has fired, Adelgren et. al. [1] report that steady state flow has resumed, with the reformation of the Edney Type IV interaction. It is also of note that the prime location for energy deposition found by Adelgren et. al. [1] was just above the axis of the hemisphere cylinder.

2.4.2 Counter-Flow Jet

Some of the earliest work with counter-flow jets was performed by Romeo and Sterrett [49], who investigated the effect of a counter-flow jet on the bow shock from a blunt body at Mach 6 and a unit Reynolds number of $22.6 \times 10^6/\text{m}$. They varied the stagnation pressure ratio of the jet to free

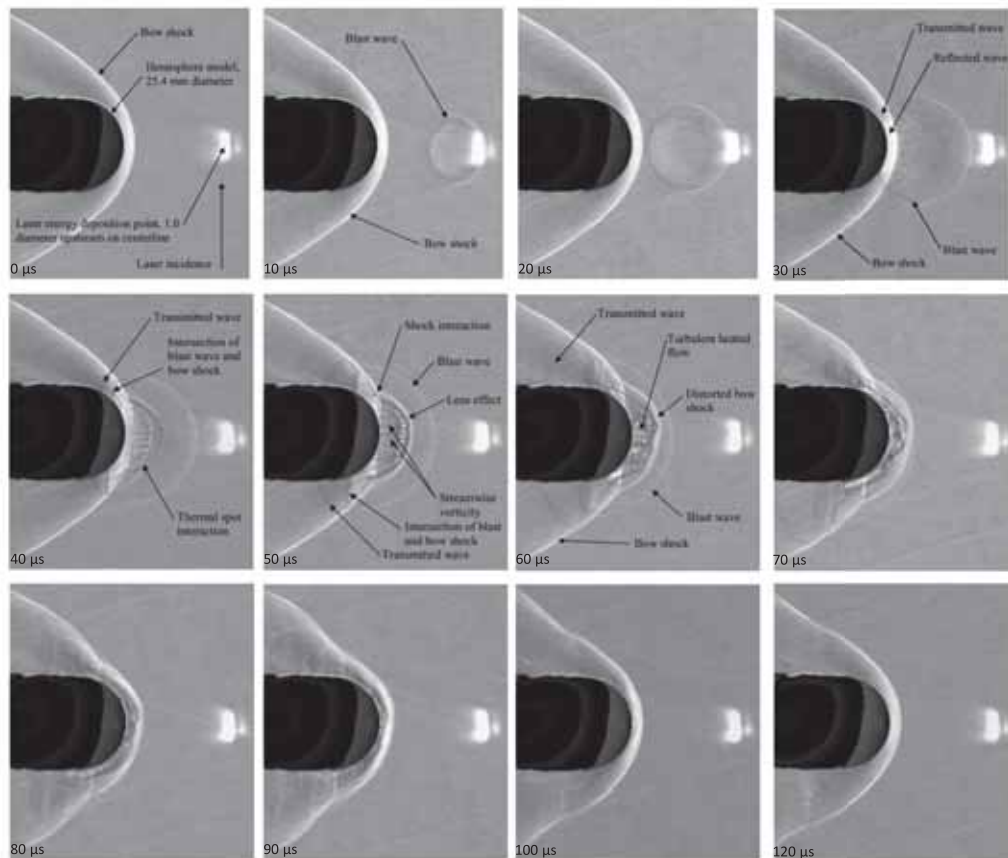


Figure 2.21: Schlieren images taken by Adelgren et. al [1] of laser energy deposition in front of a hemisphere cylinder in Mach 3.45 flow. The numbers under each figure refer to the number of microseconds after the laser had been fired.

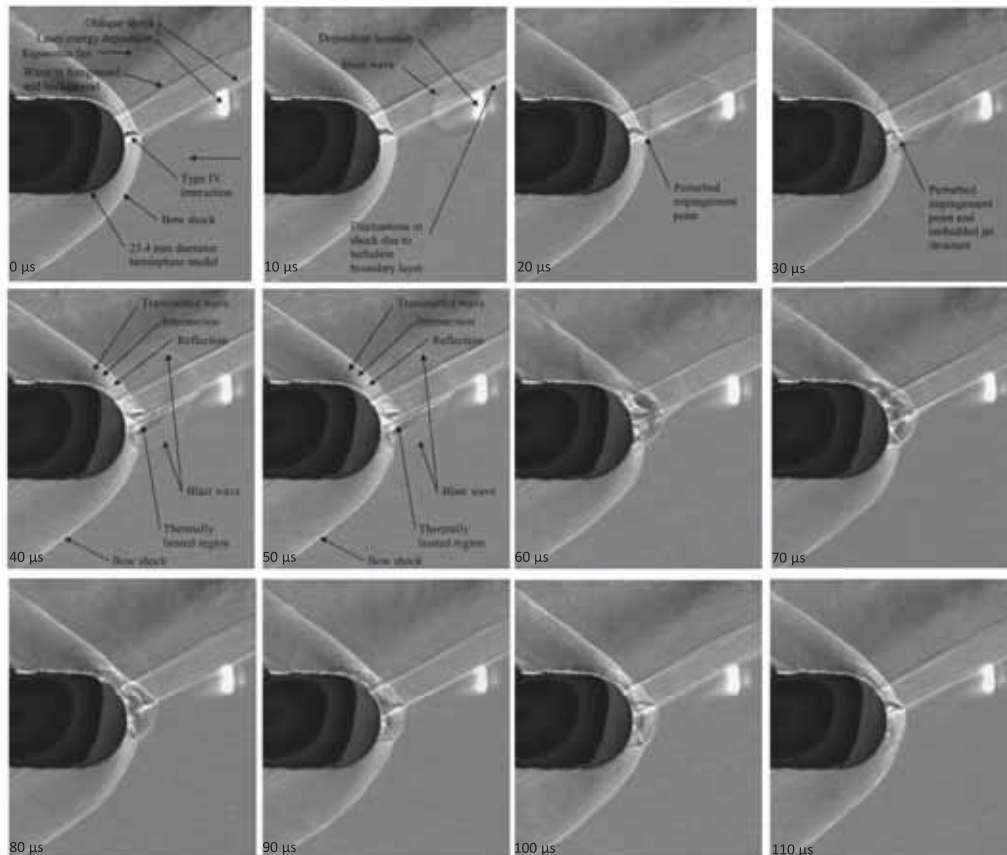


Figure 2.22: Schlieren images taken by Adelgren et. al [1] of laser energy deposition in front of a hemisphere cylinder experiencing an Edney Type IV interaction in Mach 3.45 flow. The numbers under each figure refer to the number of microseconds after the laser had been fired.

stream from 0.03 (no flow case) to 2.5. They also changed the jet diameter to body diameter ratio from 1.12 to 55.6, with angles of attack ranging from 0° to 35° . As the pressure ratio increased, the jet pushed the bow shock further away from the blunt body until the distance increased such that the bow shock became highly unstable. This effect was observed to fall off quite sharply as the angle of attack increased. Since this study used only Schlieren and high speed images of the flow, no quantitative conclusions about the consequence of counter-flow jets on the flow can be drawn. Finley [50] ran experiments using a free stream Mach number of 2.5 ($Re/m = 27.6 \times 10^6/m$), with a hemisphere cylinder as the blunt body. Finley's main contribution was to describe the flow interactions due to the counter-flow jet, providing diagrams like figure 2.23. This diagram was constructed by analysis of Schlieren images. Finley was able to corroborate previous findings (like those of Romeo and Sterrett [49]) through his work, and also recommended that further investigations look into the practical applicability of counter-flow jets to drag reduction and heat transfer reduction for high speed flights. Although he didn't specifically mention Edney interactions, it is clear that they would benefit from reduction in the peak heating and pressure found. Shang et. al. [41] used a hemisphere cylinder at Mach 6 to investigate and quantify the drag reduction given by counter-flow jets. They found that the bow shock was split into two parts, with the jet having the same effect as a spiked tip, which first creates a weaker shock. This weaker shock is more efficient at reducing wave drag, and especially at the centreline, could be significant in Edney Type IV flows. Drag reduction values up to 40% were found by Shang et. al. The reason for the drag reduction stems from the splitting of the bow shock into several shocks, which although might produce the same pressure rise, the entropy increase will be much less, as it is proportional to the third power of the pressure increase. However, Shang recommends more investigation into the unsteady oscillations which were briefly described by Romeo and Sterrett [49] be undertaken, as these oscillations have large enough amplitudes to induce unsteady motion of the model. Venukumar et. al [43] used a large angle blunted cone at Mach 8 in a shock tunnel to investigate drag reduction. Under their test conditions, drag reduction between 30 and 45% was found to exist. They found, as might be expected, that the greatest drag reduction was found for the highest total jet pressure to pitot pressure. Daso et al. [44] undertook a study using a highly angle blunted cone in Mach 3.48 and 4.0 flow. Their jet size ranged from 0.25 inches to 0.5 inches, with five different nozzle designs: three sonic and two supersonic. Similar to Shang

et. al [41], they found that the bow shock was split into many compression waves, which would then merge into a very weak bow shock as the jet flow rate increased. The measured heat transfer gave promising results for use with Edney Type IV interactions - heat flux at the surface was significantly reduced, by about 50 % at low jet flow rates, and even reaching negative heat flux for some very high jet mass flow conditions. This indicated that the flow was actually cooling the model, which would be extremely beneficial to apply to Edney Type IV interactions.

The above studies show the potential to apply counter-flow jets to disrupting Edney interactions, greatly reducing the peak heating and pressure. However, to date, no work has been done investigating the applicability of counter-flow jets to control of Edney Type IV interactions.

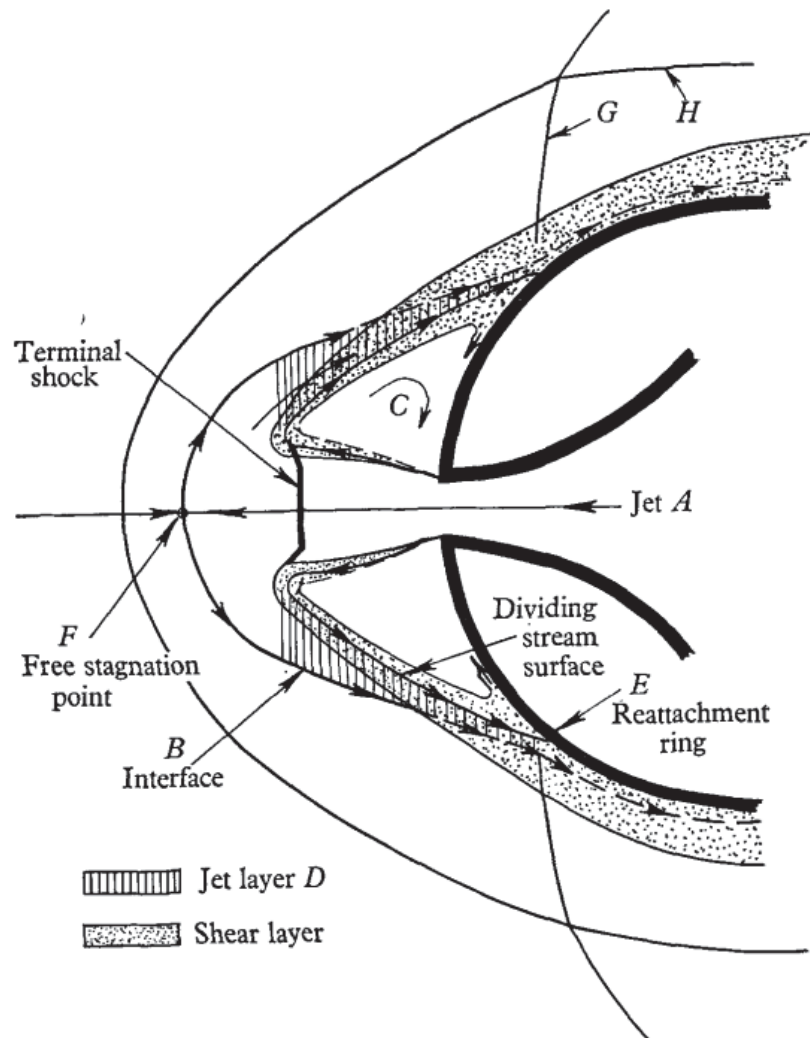


Figure 2.23: Diagram showing the flow characteristic in a counter-flow jet, produced by Finley. Flow is from left to right, at a free stream Mach number of 2.5. [50]

2.5 Conclusions

It is obvious from the literature surveyed that Edney Type interactions are themselves a dangerous phenomenon if not properly understood and controlled. The work done by Edney in quantifying the types, their causes and their effect on the flow around blunt bodies was crucial to advancing the knowledge of the field. Initial work using laser energy deposition to control these interactions has proved promising overall, but more detailed analysis is needed to understand the best way to implement a solution to this problem. Initial work will also be undertaken to investigate the usefulness of applying counter-flow jets as a method of controlling the peak heating. A combination of the two methods will be attempted as the final part of the investigation.

Chapter 3

Methodology

3.1 Introduction

Use of laser energy deposition to control Edney Type IV interactions requires a number of different systems to interact and work well together. These include the wind tunnel in which the experiments will be run, the experimental program, various flow diagnostic techniques and the experimental models themselves. All of the above have various limitations which must be understood so that the best possible data can be obtained in the experimental process.

3.2 Hypersonic Tunnel

The high speed wind tunnel which will be used for this research is an intermediate blow-down hypersonic tunnel, using dry air as the working fluid, with a test time of approximately 7.5 seconds. The system is comprised of a high pressure vessel, an electric heater, an axisymmetric nozzle, the working section, vacuum tanks and auxiliary systems. The auxiliary systems are mainly pressure supply, water cooling and pumping. For this research, a Mach 5 nozzle will be used, giving an axisymmetric nozzle exit diameter of 152 mm. The working gas temperature may be heated from 375 K to 700 K - this is to avoid condensation in the test section. The usable stagnation pressure range is 6 to 8 bar. By varying these two settings, unit Reynolds numbers between 4.5 to $15 \times 10^6/\text{m}$ may be obtained. The test section itself has a 325 mm square cross section and is 900 mm in length, with a diffuser placed 0.4

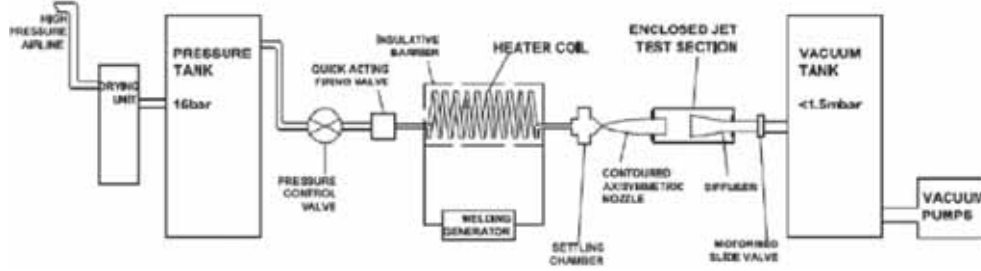


Figure 3.1: Schematic of Hypersonic Wind Tunnel, taken from [51]

metres after the nozzle exit. Optical access from the side is provided by two 195 mm quartz windows, with two windows on the top as well. A schematic of the tunnel is shown in figure 3.1.

The tunnel schematic shows some of the important aspects of the HSST at the University of Manchester. Air is passed through a drying unit and stored in a high pressure (16 bar) vessel. A dome valve then controls the pressure that the tunnel will be operating at. There is an insulated box housing a heater with a 30 m long coil to ensure no liquefaction is present in the air, as well as controlling the stagnation pressure, up to a maximum of 700 K. After the heater, the settling chamber is designed to give a uniform flow distribution in the working section of the wind tunnel - subsequent tests by Dr. Erdem [52] have demonstrated that this is effectively accomplished. A slide valve separates the working section from the vacuum tanks, meaning that the vacuum tanks won't get pressurized while making adjustments to the working section. Flow is controlled by use of a fast acting ball valve, located between the dome valve and heater coil.

3.2.1 Hypersonic Tunnel Calibration

When the hypersonic wind tunnel started operating at relatively high capacity, a calibration test was performed [52] to gauge the performance utilizing the Mach 5 nozzle with 152 mm exit diameter. These tests determined the useful running time of the tunnel, useful space available and how uniform the flow was. A pitot rake was attached to a sting mounted on an arc system; this rake is shown below in figure 3.2. The calibration was performed with the following flow conditions: $P_{supply} = 175$ Psi, $T_{supply} = 375^\circ$ K, $M_\infty = 5.0$,

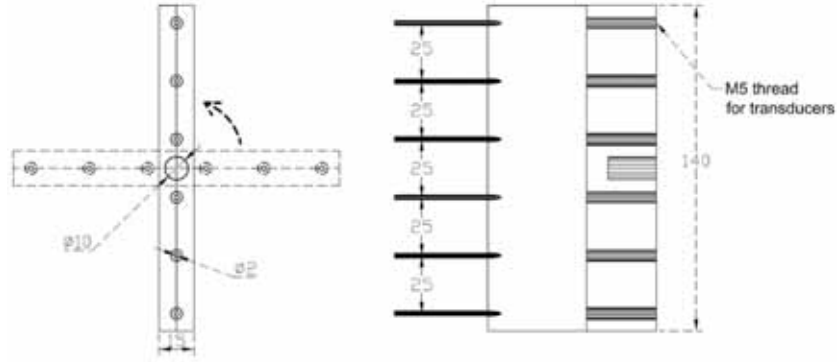


Figure 3.2: Schematic of pitot rake used to calibrate Hypersonic Wind Tunnel, taken from [52].

$P_0 = 6450$ mbar, $T_0 = 372^\circ$ K and $Re/m = 13.1 \times 10^6/m$.

Figure 3.3 shows the time traces of static and stagnation pressure as well as stagnation temperature in the HSST. The pressure signals show the sharp increase in pressure as the tunnel starts - the normal shock travelling through the test section (assuming the area ratio is such that no blockage occurs) and disappearing into the diffuser. This then gives way to a stable plateau of pressure, lasting for roughly 7.5 seconds. After this time, due to an increase in pressure in the vacuum tanks, the normal shock travels back through the test section, ending the useful run time. It is reported that the pressure variation is less than 1% of the average value seen in the plateau region. During the run, the stagnation temperature rises from vacuum temperature to the heater temperature - the continuous rise is an artifact of the thermocouple and not actually a physical phenomenon.

All the calibration work described in the above section was conducted by Dr. Erinc Erdem [52] as part of the commissioning and setting up of the HSST at the University of Manchester. It demonstrates the precision and accuracy of this valuable research tool in conducting the research proposed and described in this initial report.

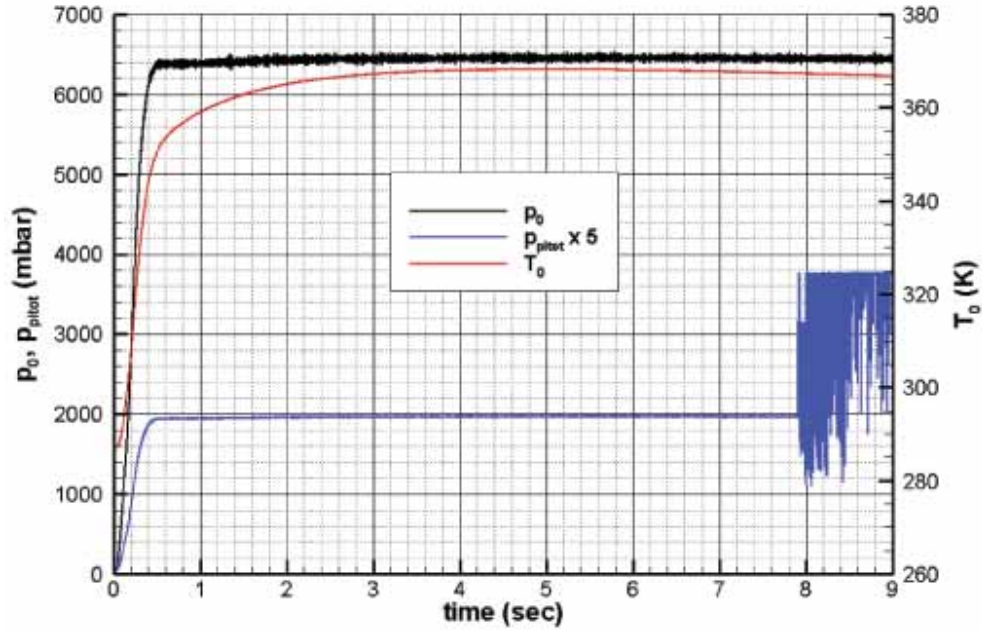


Figure 3.3: Time traces of stagnation pressure, pitot pressure and stagnation temperature for the tunnel run. Stagnation temperature axis is on the right hand side, in Kelvin, whereas the left hand axis displays pressure in millibars. The pitot pressure has been multiplied by 5 so as to be readable on the graph. Taken from [52].

3.3 Experimental Program

In order to investigate laser energy deposition and the relationship it has to mitigation of Edney Type IV interactions, a number of test types need to be run. In all of the test series, two unit Reynolds numbers will be used – $4.5 \times 10^6/\text{m}$ and $13 \times 10^6/\text{m}$. The first series of tests will be run to establish baseline drag/pressure and temperature measurements for each model. Then a series of tests will be run which establish baseline pressure/temperature readings in the presence of Edney Type IV interference. Thirdly, a series of tests will be run which investigate the effectiveness of laser energy deposition in mitigation of surface pressure and temperature without Edney Type IV interference. Finally, a series of tests will be run where laser energy deposition is used to mitigate the negative effects of Edney Type IV interference. For

the tests which utilize energy addition to the flow, on-axis and off-axis focal points will be used, as some studies have found the best mitigation to occur for energy addition above the symmetry axis of a hemisphere cylinder [1].

3.4 Diagnostic Techniques

3.4.1 Introduction

An experimental investigation into optimizing laser energy deposition for control of Edney Type IV interactions obviously needs to measure and analyze certain parameters which can be used to gauge the relative success or failure of a given setup. Parameters of interest to the investigation include the surface pressure, the surface temperature, the change in the shock structure (both spatially and temporally) and the flow field. Each of these parameters may be measured in different ways, with the constraints due to experimental facilities and flow physics meaning that some techniques may not be viable throughout the experimental program. A brief overview of the following experimental techniques will be given, and then some discussion as to potential problems in application to some or all of the experimental program: surface flow oil imagery, force measurements, pressure/temperature sensitive paints, schlieren/shadowgraph, particle image velocimetry, and infrared thermography.

3.4.2 Surface Oil Flow Imagery

Careful use of oil mixed with powder can allow one to visualise traces and extents of flow structures. These mixtures respond to changes in surface pressure or temperature as well as transition to turbulence [53]. Erdem found that the following mixture is optimal for use in hypersonic wind tunnels: 1.5g of TiO_2 powder dissolved in 8.0g of linseed oil, 2.0g of silicone 800 oil, with a couple drops of oleic acid [52]. Using oil flow imagery, the changes to the flow that laser energy deposition or a counter-flow jet are making can be visualised on the surface, although some of the more interesting flow structures expected by the counter-flow jet are impossible to visualise by surface based methods.

3.4.3 Three-component Force Balance

Measurement of drag and lift during the proposed experimental programme is a key part of understanding the flow physics and how the methods used for controlling the interactions might affect flight characteristics. One method of collecting these measurements is by use of a force balance which measures lift, drag and pitching moment. The force balance used in these experiments is manufactured by Aerotech©. An arc system which can change incidence between $\pm 20^\circ$ supports a tapered sting that holds the model. The sting has three strain gauges; one for each measurement. The sample rate of the force balance is 4-5 kHz, but data can be stored at a maximum of 300 Hz only. The uncertainty in the lift and drag measurements is ± 0.074 N [52]

3.4.4 Pressure and Temperature Sensitive Paints

Typically, pressure measurements on the surface of any model in flow have been made using pressure taps and piezo-electric sensors. Temperature measurements similarly have been made with the use of thermocouples. Both of these measurement techniques suffer from the same inherent problems. Large scale instrumentation of a model for measurement is a costly and labour intensive undertaking, and depending on the ratio of pressure taps/thermocouples to measurement channels, a test may need to be repeated twenty times in order to achieve proper measurements at each desired location with enough repeats to ensure that the data can be trusted. Additionally, the spatial resolution achievable with these point measurements is limited by the size of the taps or thermocouples. Pressure and temperature sensitive paints (PSPs and TSPs) are valuable non-invasive surface measurement techniques. Unlike traditional methods, they do not require the same amount of labour and cost in setting up the instrumentation. They also are able to provide a measurement map of the surface, reducing the number of repeats needed to achieve data which may be trusted [54,55].

Although there are different equations, the same general principle governs the usage of PSP and TSP. Luminescent molecules (luminophores) are deposited onto the desired surface, via a soluble polymer coating or absorption of the molecule onto a highly porous surface. The polymer coating can most often be dissolved in a solvent, so that the luminescent molecules may be applied as a paint. When the solvent evaporates, the molecules are bound in place on the surface. When light of the correct wavelength illuminates

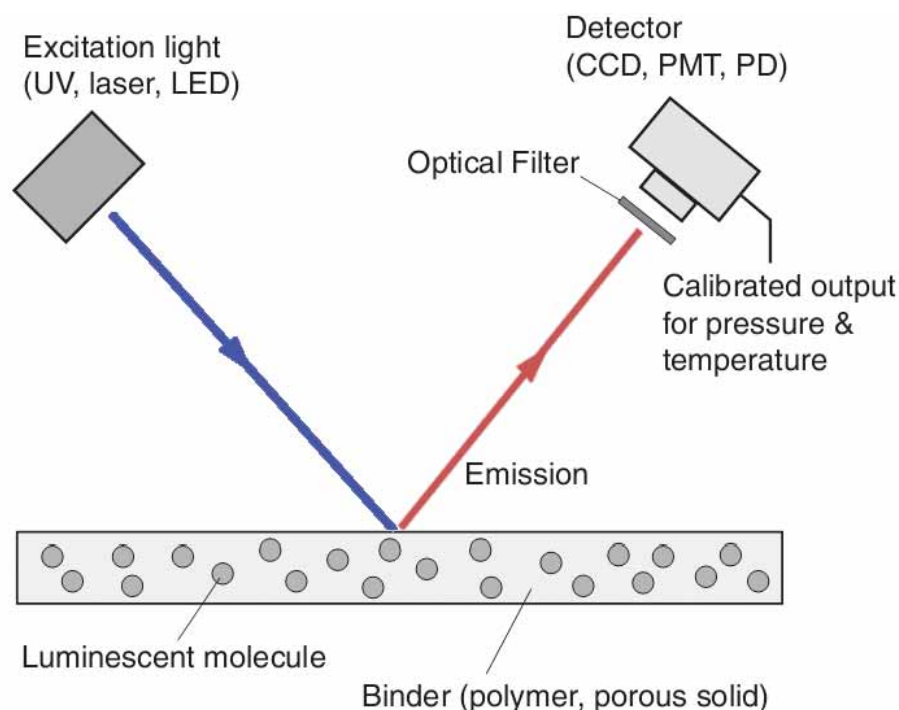


Figure 3.4: General schematic of pressure sensitive paint/temperature sensitive paint on a surface [55].

the paint, the luminescent molecules become excited, and light of different wavelength is emitted. The difference between the excitation wavelength and the emission wavelength is known as the Stokes shift. A larger Stokes shift is desirable, as it becomes easier to separate the two signals. This process is roughly sketched in figure 3.4

In the case of PSP, the molecules are sensitive to oxygen quenching - a process by which the luminescence intensity decreases as the concentration of oxygen molecules increases, which is related to the air pressure through partial pressures. For TSP molecules, the intensity of the luminescence decreases as the temperature increases, a process known as thermal quenching. TSP is only sensitive to temperature, as the polymer binder is impermeable to oxygen, whereas PSP is also sensitive to temperature due to thermal quenching. Once the paints are properly calibrated, a pressure/temperature map of the surface may be obtained [54–57].

The way pressure sensitive paints will be used require a reference image to be taken at a known pressure - known as the wind-off image. This eliminates any non-uniformity in the distribution of the luminophores or in the incident light. The intensity and pressure are related through an equation known as the Stern-Volmer equation [54–57].

$$\frac{I_{ref}}{I} = A(T) + B(T) \left(\frac{P}{P_{ref}} \right)$$

where I is the intensity, P is the pressure, and $A(T)$ and $B(T)$ are coefficients, obviously functions of temperature. The coefficients are always experimentally determined. Calibration also will involve the use of piezo-electric pressure sensors mounted on the leading surface, so that a relationship between the measured intensity and the known pressure can be evaluated. This is known as in-situ calibration, as opposed to a priori, which takes place in a laboratory before the experimental models are in the wind tunnel. This calibration may prove difficult at times, due to the increased pressure which is expected from the Edney Type IV interaction.

A similar relationship between intensity and temperature can be written for TSPs [55].

$$\ln \frac{I(T)}{I(T_{ref})} = \frac{E_{nr}}{R} \left(\frac{1}{T} - \frac{1}{T_{ref}} \right)$$

where I is the intensity, T is the temperature, E_{nr} is the activation energy for a non-radiative process, R is the universal gas constant and T_{ref} is a reference temperature in Kelvin. Unlike PSP, this equation clearly has no pressure dependency, which allows TSP to be used in conjunction with PSP to calibrate out the temperature dependency inherent in the pressure calibration equation [55, 58, 59].

Given the high temperature dependency even of the baseline case, due to the curved nature of the models, a methodology which coats half of the model in PSP and half in TSP will be attempted. It is hoped that by this method, a temperature map may be obtained which can then be matched to a calibration plane for the TSP, allowing a pressure map also to be obtained. Since all models are symmetric about the vertical axis, the temperature map obtained should be applicable to the other side, and the same with the pressure map. In order for the proposed method to be a viable solution, both luminophores should be excited at the same wavelength but emit at different enough wavelengths so they may be separated. It is not yet known whether

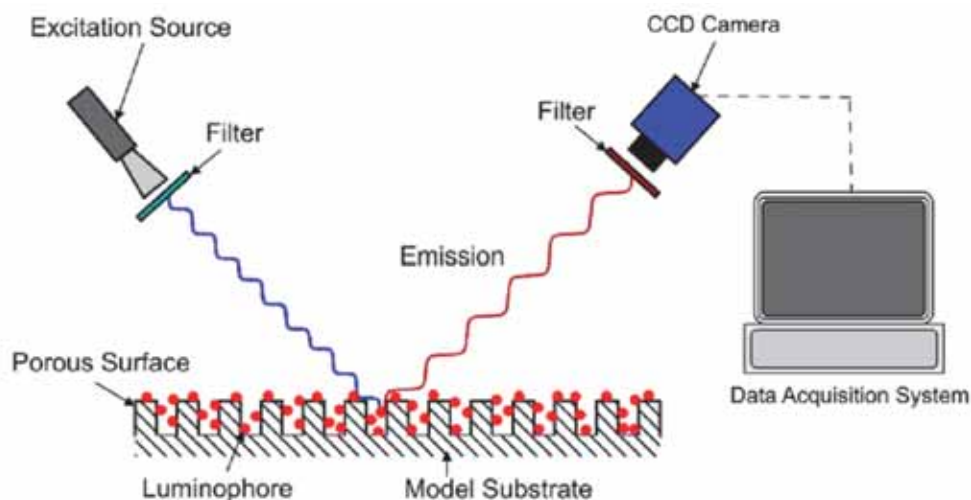


Figure 3.5: Porous-based schematic of pressure sensitive paint/temperature sensitive paint on a surface [54]. The original image is to demonstrate porous-based pressure sensitive paint, but the same process may be applied to temperature sensitive paint.

the high temperatures expected from Edney Type IV interactions are enough to render this solution unviable.

Both the PSP and TSP would be applied using the porous based method, where aluminium is anodized by phosphoric acid. As noted by Quinn et. al. [54], the pore size and depth (controlled by the voltage and time in the acid) have a strong effect on the response time of the anodized aluminium. A diagram of the porous-based method of PSP and TSP is shown in figure 3.5.

As part of the calibration of the TSP paint, an absorption and emission spectrum is shown in figure 3.6. The red line shows the absorption spectrum, with two specific peaks at 346 nm and a smaller peak at 488 nm. The paint's emission peak is highest between 588 and 618 nm. This was measured using a 1 kW Xenon arc lamp with a blue dichroic filter that cuts off light above 550 nm. The receptor had an orange long pass filter in front of it that cuts off any light with a lower wavelength than 530. This closely mimics what the experimental setup would be with this TSP.

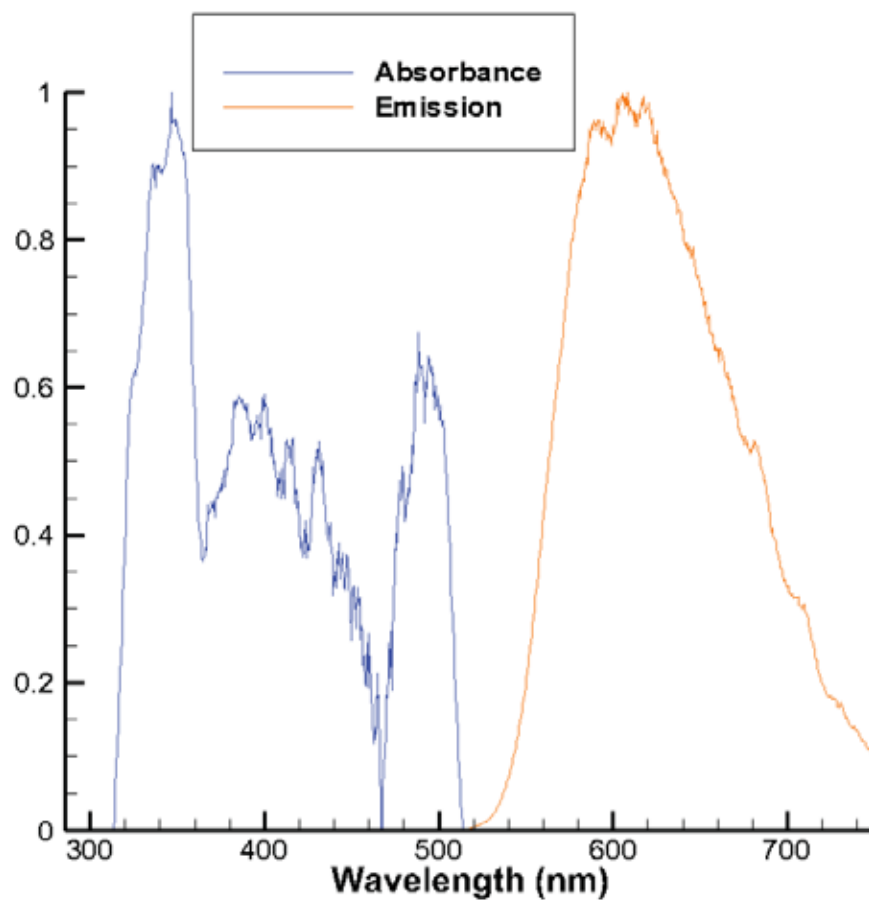


Figure 3.6: Absorbance and Emission spectrum for the TSP being used. The x-axis shows the light wavelength in nanometres and the y-axis is arbitrary units of intensity.

3.4.5 Schlieren and Shadowgraph

The use of optical methods to detect changes in density within fluids was first discovered and reported by Robert Hooke in *Micrographia* [60], specifically observation LVIII. He used this to explain a number of different phenomena: stars twinkling, convection within fluids, heat haze, turbulent mixing, mirages and stratified flows. One of the key observations he made involved veins (streaks or schlieren) in glass. Using a candle as a light source, and another candle near a focusing lens to refract some of the incident light rays away, even with the naked eye, the transparent convective plume from the first candle may be seen. This technique has been refined so as to give greater clarity, but the principle stems from Hooke's original observations. Hooke also explained that the plume from a lit candle could also be seen from its shadow, describing the modern shadowgraph technique [60,61].

Both of these techniques will be used to visualize the shockwave systems within the test section, and previous figures presented have been of schlieren images. The basic operating principle of a modern schlieren system is that collimated light passes through a slit, then through an optical system consisting of lens and or mirrors, with the desired visualization region occurring before the light reaches a knife edge which cuts out some of the light. The resulting image is passed through a lens to a camera. This is shown in figure 3.7, where the knife edge is positioned to cut half the image off that the slit lets through. However, a change in the refractive index at position S could make the light either miss the knife edge and produce a lighter patch on the photograph, or be further blocked by the knife edge, and produce a darker spot on the photograph. A clear picture of the gradient of the refractive index at position S is produced by this technique.

The sensitivity of a schlieren system can be adjusted by changing the slit width or the position of the knife edge, as this fractionally changes how much or little light the knife edge deflects away. When a smaller amount of light is allowed to pass through to the camera, the system will be more sensitive to changes in density, but will also produce a darker image. Balancing this is key to producing clear schlieren images of the phenomenon under investigation. Additionally, since large lenses without blemish are extremely expensive, the schlieren setup which will be used is shown in figure 3.8. This system utilizes two concave mirrors in what is commonly referred to as a z-configuration.

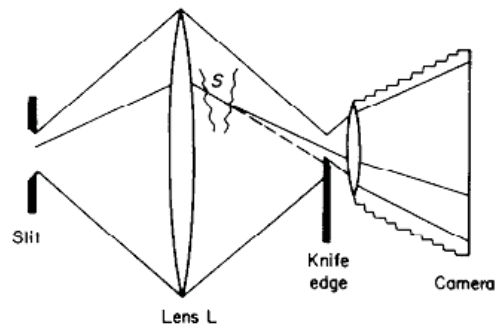


Figure 3.7: Basic schlieren setup diagram [62].

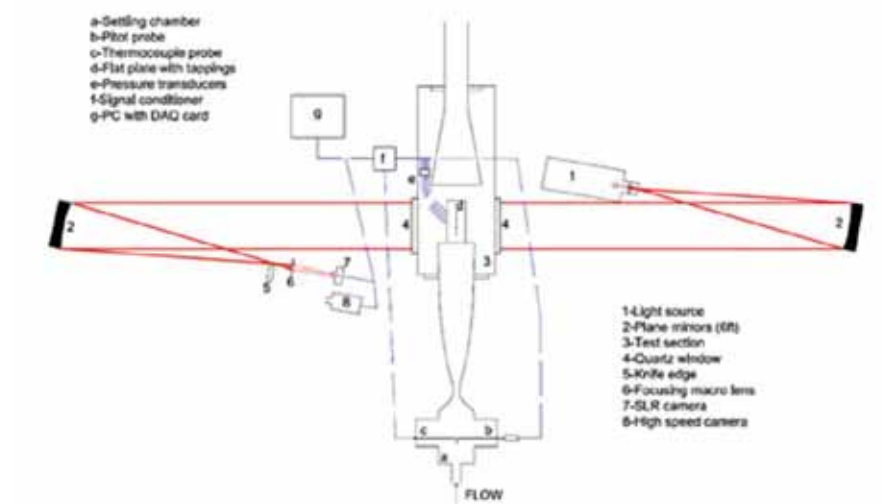


Figure 3.8: Experimental schlieren system diagram [63].

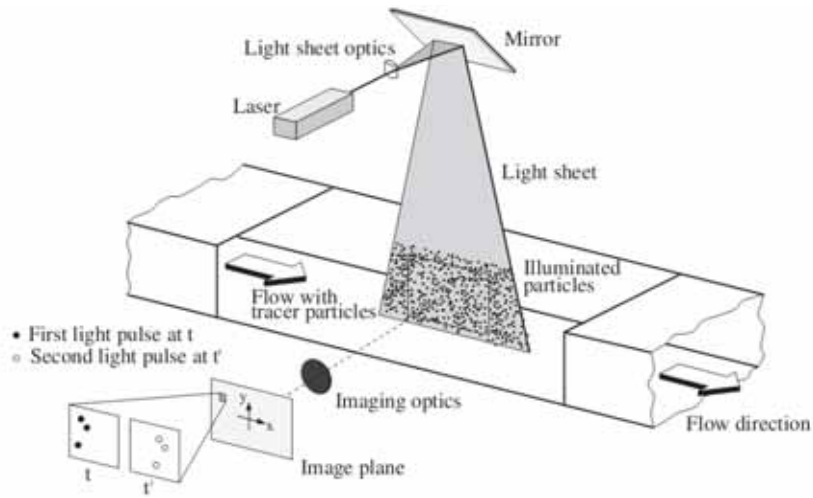


Figure 3.9: Typical PIV system setup [64].

3.4.6 Particle Image Velocimetry

Particle image velocimetry (PIV) is a flow diagnostic technique where micro or nano scale particles are released into the flow, with an illumination source lighting a plane within the flow. Two or more images are taken in rapid succession, recording the light scattered by the particles. Using a sophisticated software algorithm, two subsequent images are compared by breaking each image down into smaller domains, known as interrogation areas. Using statistical means such as cross and auto correlation, the local displacement vector is calculated for the images of the tracer particles within each interrogation area. It is assumed that each particle moves with the localized flow velocity, and that particles within an interrogation area have moved uniformly between snapshots [64–67]. An image of a velocity field calculated using PIV is shown in figure 3.10 and an image of a typical PIV setup is shown in figure 3.9.

Particle image velocimetry is not a technique that can be applied to all the test series outlined in the experimental program. For any flow that includes laser energy deposition, the presence of particles in the flow will mean that the laser will breakdown around any one of the particles earlier than the desired deposition location. Additionally, it has been demonstrated that the presence of impurities in the flow lowers the required power density to achieve

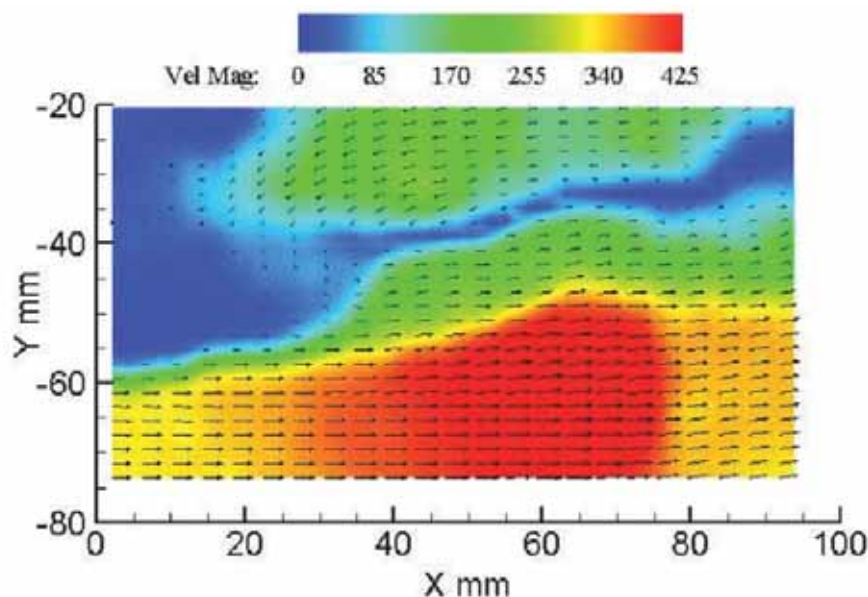


Figure 3.10: Sample PIV velocity field [65]. The flow being investigated is in a shocktube with a sharp splitter separating the top and bottom flows. The bottom half was driven at an initial Mach number of approximately 1.66, and the top half was initially a freestream jet.

breakdown in air [68]. As such, any analysis of the flow using PIV will have to be in one of the two baseline cases.

3.4.7 Infrared Thermography

Infrared thermography is a technique which allows non-intrusive measurement of surface temperature in fluid flow and heat transfer. An infrared camera captures an image which is representative of the thermal radiation emitted by a heated surface in the IR band. Using a calibration law, the temperature of the surface may be calculated [69–72]. Infrared thermography can be as sensitive as 20 mK and have a response time as low as 20 μ s and the nature of the diagnostic means that a 2-D temperature map can be obtained. This makes it an ideal sensing technique for use in transient flows ranging from natural convection to hypersonic problems [70, 73]. Recent literature has shown that use of a novel 3-D mapping technique coupled with infrared thermography can produce an accurate temperature map of a

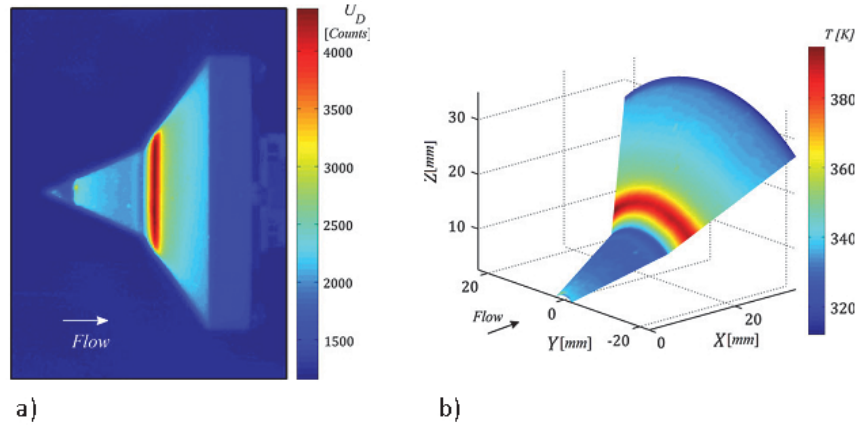


Figure 3.11: a) Sample IR image of double cone with Edney Type IV interaction [70]. b) 3-D image of the Ir map of the double cone imaged in a). Due to the model being axisymmetric, this result can reasonably be applied to the whole surface.

double cone experiencing an Edney Type IV interaction [70]. This is shown in figure 3.11.

3.5 Experimental Models

There will be two sets of experimental models; a hemisphere cylinder with a diameter of 25 mm, and a swept cylinder with a diameter of 25 mm. The swept cylinder will have sweep angles of $\pm 45^\circ$, $\pm 30^\circ$, $\pm 15^\circ$ and 0° . This will be accomplished by utilizing an invertible fin with a swept cylindrical leading edge at the specified angles. Within the set of swept-cylinder fins, there are two types of attachments - an attachment manufactured from aluminium and an attachment manufactured from Macor. Each attachment connects to a holder and base which allows for movement parallel to the flow direction within the hypersonic blowdown tunnel at the University of Manchester.

The aluminium attachment has three pressure taps drilled into the leading surface, at the centreline, parallel to the overall flow direction. This model will be used in conjunction with pressure sensitive paints, temperature sensitive paints and piezo-electric pressure sensors. A rendition of the model is produced in figure 3.12.

The Macor attachment has a smooth leading surface, and will be used



Figure 3.12: Rendering of the 45° aluminium swept-cylinder fin to be used for pressure/temperature sensitive paint measurements and piezo-electric pressure sensing.

with infrared thermography to obtain further temperature mapping of the surface. Macor was chosen as an ideal material for use in these tests because it has quite a low thermal conductivity and diffusivity ($1.46 \text{ W/m}^\circ \text{C}$ and $7.3 \times 10^{-7} \text{ m}^2/\text{s}$ at 25°C), a high operating temperature of approximately 800°C [74] and a high emissivity [70]. This makes it highly unlikely to melt under the increased heat from the Edney Type IV interactions as well as retaining heat on the surface long enough for infrared thermography to map the transient temperature. A rendering of the Macor attachment is produced in figure 3.13

The hemisphere cylinder will be attached to a force balance which can vary the angle of attack between $\pm 20^\circ$. There are two models - an aluminium model for pressure/temperature sensitive paints and a Macor model for infrared thermography. Apart from the material, the two models are identical. A rendering of the aluminium model is given in figure 3.14. Additionally, a set of models with a centreline hole have been produced, one manufactured from aluminium and one manufactured from ertalyte. These models will be used to understand the effectiveness and physics of counter-flow jet in controlling drag/peak heat transfer, with the ultimate objective

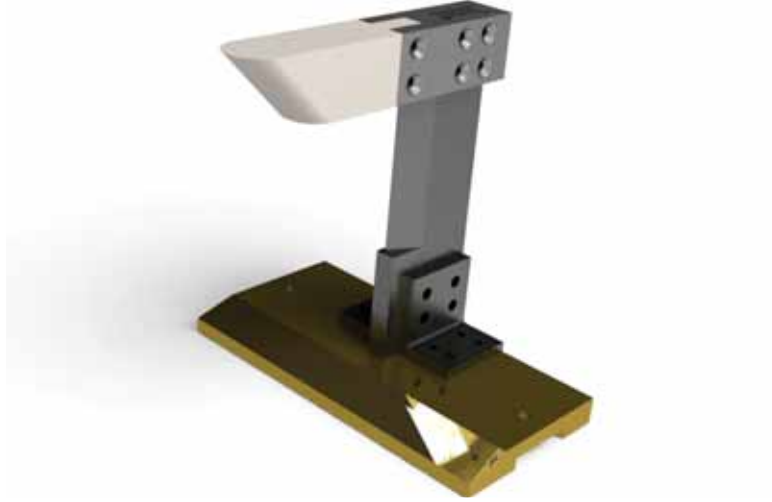


Figure 3.13: Rendering of the 45° Macor swept-cylinder fin to be used for infrared thermography.



Figure 3.14: Rendering of the aluminium hemisphere cylinder to be used for pressure/temperature sensitive paint measurements.

of applying a counter-flow jet to a system experiencing an Edney Type IV interaction. The ertalyte model has been produced as another method for obtaining quantitative infrared thermographic measurements.

In order to achieve the desired Edney Type IV interactions, a shock generator must be used. This shock generator has a turning angle of 15° , and



Figure 3.15: Rendering of the aluminium shock generator to be used in all experiments where Edney Type IV interactions are desired.

has a range of settings from 0° to 12° , at approximately 3° increments. Similarly to the swept-cylinder fins, the shock generator is mounted on a platform which can move parallel to the direction of flow. This enables the operator to setup the oblique shock to impinge as close to the centreline of the test model as possible. The shock generator is manufactured from aluminium. A rendering of the shock generator, complete with supports and mounting system may be seen in figure 3.15.

Chapter 4

Experimental Tests

4.1 Introduction

A number of baseline cases were run in the hypersonic blowdown tunnel, utilizing the hemisphere cylinder model, attached to a three component force balance. This force balance includes a measurement sting and support arc, with possible incidence angles ranging between -20° and 20° . Further description of this test facility may be found in Erdem et. al. [75,76] and in the Ph.D Thesis of Dr. Erdem [52]. The unit Reynolds numbers were $13 \times 10^6/\text{m}$ and 4.6×10^6 , with lift measurements being taken during each run. Schlieren images were captured for $\text{Re}/\text{m} = 13 \times 10^6/\text{m}$ only, as the simple cases being studied are highly unlikely to result in significant differences between the two Reynolds numbers. Four tests were run at an incidence angle of 0° , with two tests run at the following angles: 5° , 10° , 15° , -5° and -10° . The lift results are presented below, along with representative time-averaged schlieren data for each $\text{Re}/\text{m} = 13 \times 10^6/\text{m}$ case. Additionally, Quantitative Infrared Thermography (QIRT) images were captured for each run/case, which allows the time averaged heat transfer to be calculated.

4.2 Measured Data

Figure 4.1 shows a graph of Heat Transfer vs Position along the centreline of the hemisphere cylinder. The heat transfer has been calculated using a weighted time averaging algorithm, assuming a 1-D semi-infinite body. This graph also shows the heat transfer along the centreline only - where one would

expect to see the greatest heat transfer. Due to the optical arrangement of the QIRT, the stagnation point is hidden from the camera. This means that the lines shown are a continuous drop from a higher value which cannot be seen. The red line shows $Re/m = 4.6 \times 10^6$, where the maximum shown is at about $28\,500\text{ W/m}^2$, whereas the blue line shows $Re/m = 13 \times 10^6$, with a maximum shown at about $9\,800\text{ W/m}^2$. As one would expect, the heat transfer rate drops rapidly over distance as one moves away from the tip of the hemisphere cylinder. By the time one has moved the radius of the cylinder (12.5 mm), both Reynolds number runs show that the heat transfer has dropped to less than half the peak shown. In fact, the high Reynolds number case has essentially plateaued at a low value by a distance of one radius from the tip. The low Reynolds number run also demonstrates a different behaviour in the low heat transfer rate section (after about 18 mm), as it never plateaus, and even shows a sharp drop in heat transfer rate at the end. This is due to the low Reynolds number case having a much higher stagnation temperature in the flow, which means that after the bow shock, it still is able to heat the cylinder, even though flow isn't impinging on it. Theoretical heat transfer rate from [77] is calculated to be about $140\,000\text{ W/m}^2$ for $Re/m = 13 \times 10^6$ and about $151\,000\text{ W/m}^2$ for $Re/m = 4.6 \times 10^6$.

Figure 4.2 shows the Lift force vs angle of attack for both Reynolds numbers: $Re/m = 13 \times 10^6$ and $Re/m = 4.6 \times 10^6$. In both cases, there is a linear increase in lift as angle of attack increases, with both lines showing no lift when the angle of attack is zero, as would be expected. The lift calculated at $\pm 5^\circ$ angle of attack is fairly similar for both Reynolds numbers (although the High Reynolds number, for both positive and negative, has a greater value). However, moving to the case of angle of attack = ± 10 or $\pm 15^\circ$, the higher gradient for the higher Reynolds number case can be seen. This result comes from the density decreasing for the low Reynolds number case, due to the much higher static temperature experienced. It also can be seen that the higher Reynolds number cases were slightly more precise at greater angles of attack. The same force balance used for the lift measurement should be capable of measuring drag as well, but for all but one case, the result given did not correspond to what should be physically expected, and so repairs are needed to ensure accurate drag measurements may be taken.

Figure 4.3 shows Schlieren images for angles of attack of 15° , 10° , 5° , 0° , -5° and -10° at $Re/m = 13 \times 10^6$. The shock standoff distance is calculated to be 2.08 mm, which compares very well with the theoretical value of 2.03 mm.

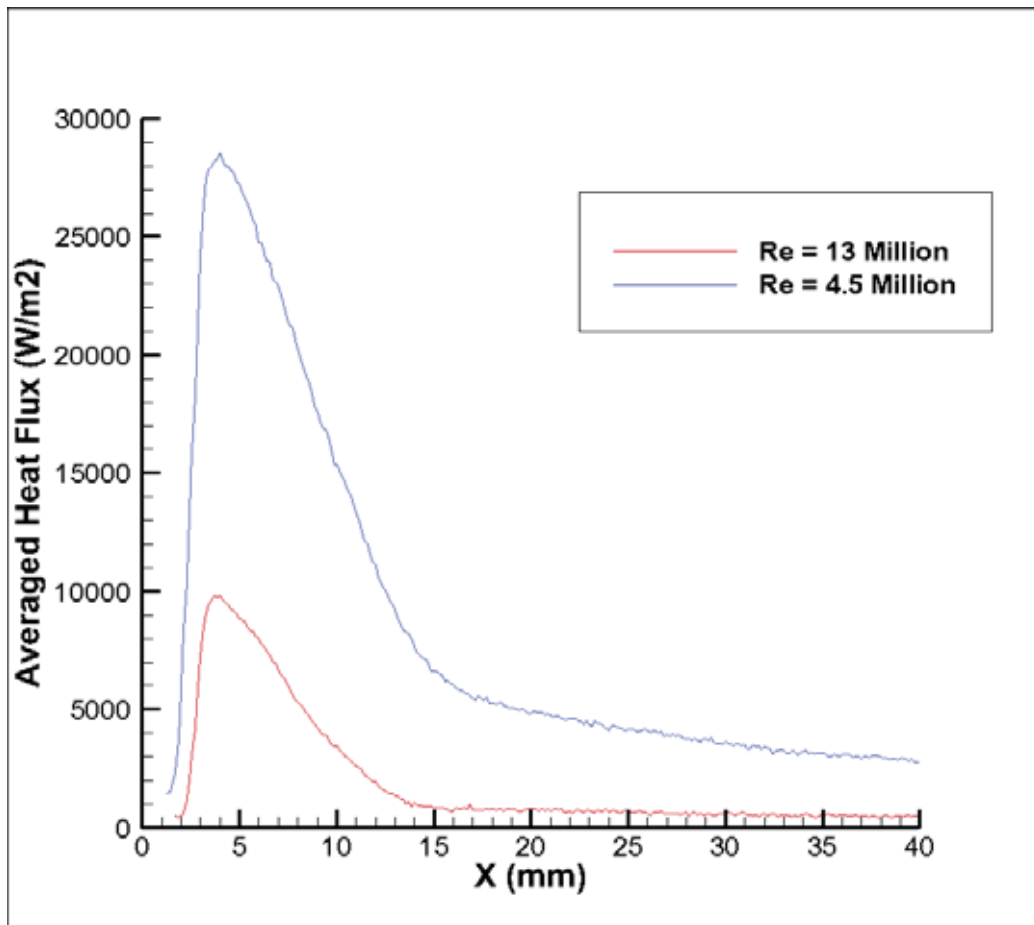


Figure 4.1: Baseline Surface Heat Transfer (W/m^2) along the centreline (X position in mm) of hemisphere cylinder.

All of the results shown above are baseline results, useful in establishing that the analytical methods being used are implemented correctly, as well as giving a number to normalise results with shock interaction and energy deposition.

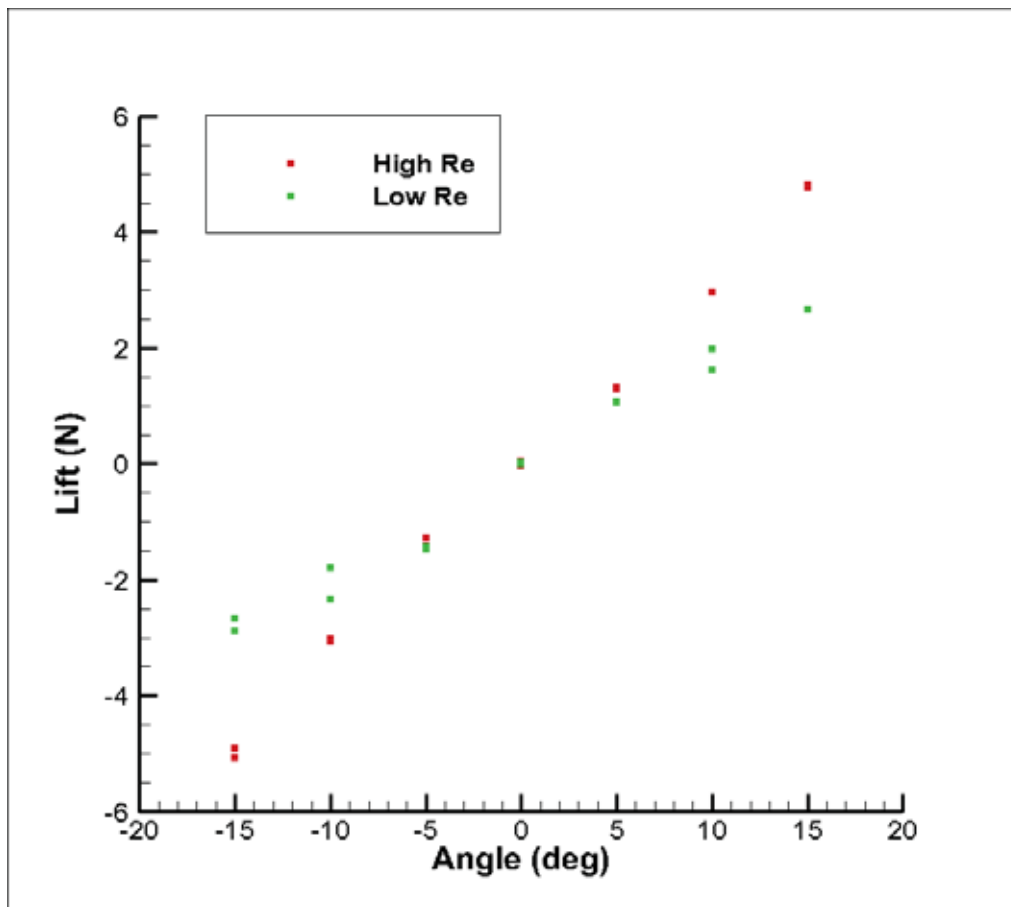


Figure 4.2: Lift Force (N) vs Angle of Attack ($^{\circ}$). High Re = 13×10^6 and Low Re = 4.6×10^6 .

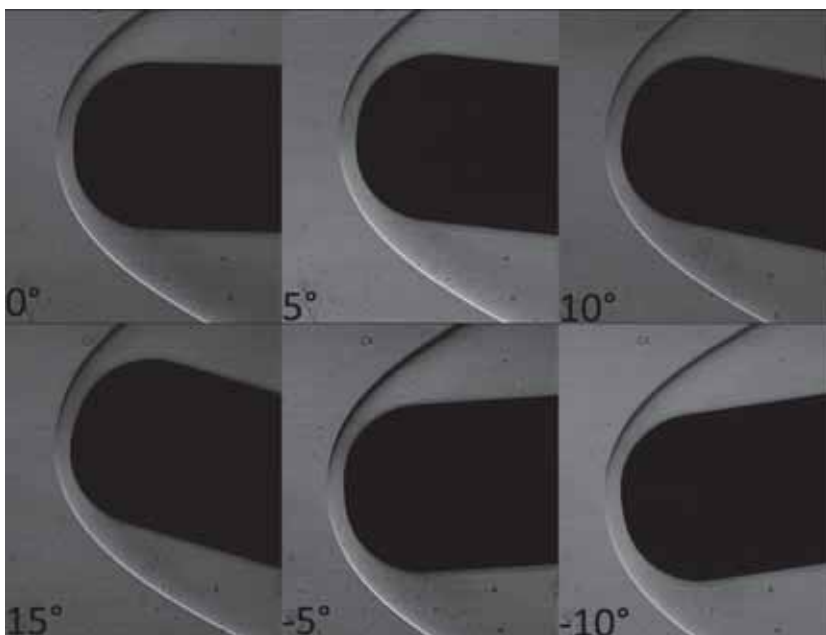


Figure 4.3: Schlieren images of hemisphere cylinder at different angles of attack. Flow is from left to right, $Re/m = 13 \times 10^6$.

Chapter 5

Future Work

5.1 Work plan for Years 2 and 3

As can be seen from the scope of the proposed work, there is much work to be done in the coming year to accomplish the desired goals. This includes, but is not limited to the following:

- Baseline tests of the Hemisphere Cylinder model, gathering drag, PSP/TSP, IR and Schlieren data
- Baseline tests of the Swept-Cylinder models, gathering PSP/TSP, IR and Schlieren data
- Baseline tests of Edney Type IV interactions with the Hemisphere Cylinder and Swept-Cylinder models
- Baseline tests of Counter-Flow Jet, with and without shock impingement.
- Characterise and quantify the laser discharge.
- Laser Energy Deposition with Hemisphere Cylinder.
- Laser Energy Deposition with Swept-Cylinder model.

The proposed timeline for the above tasks is shown in the Gantt Chart (Figure 5.1) on the following page.

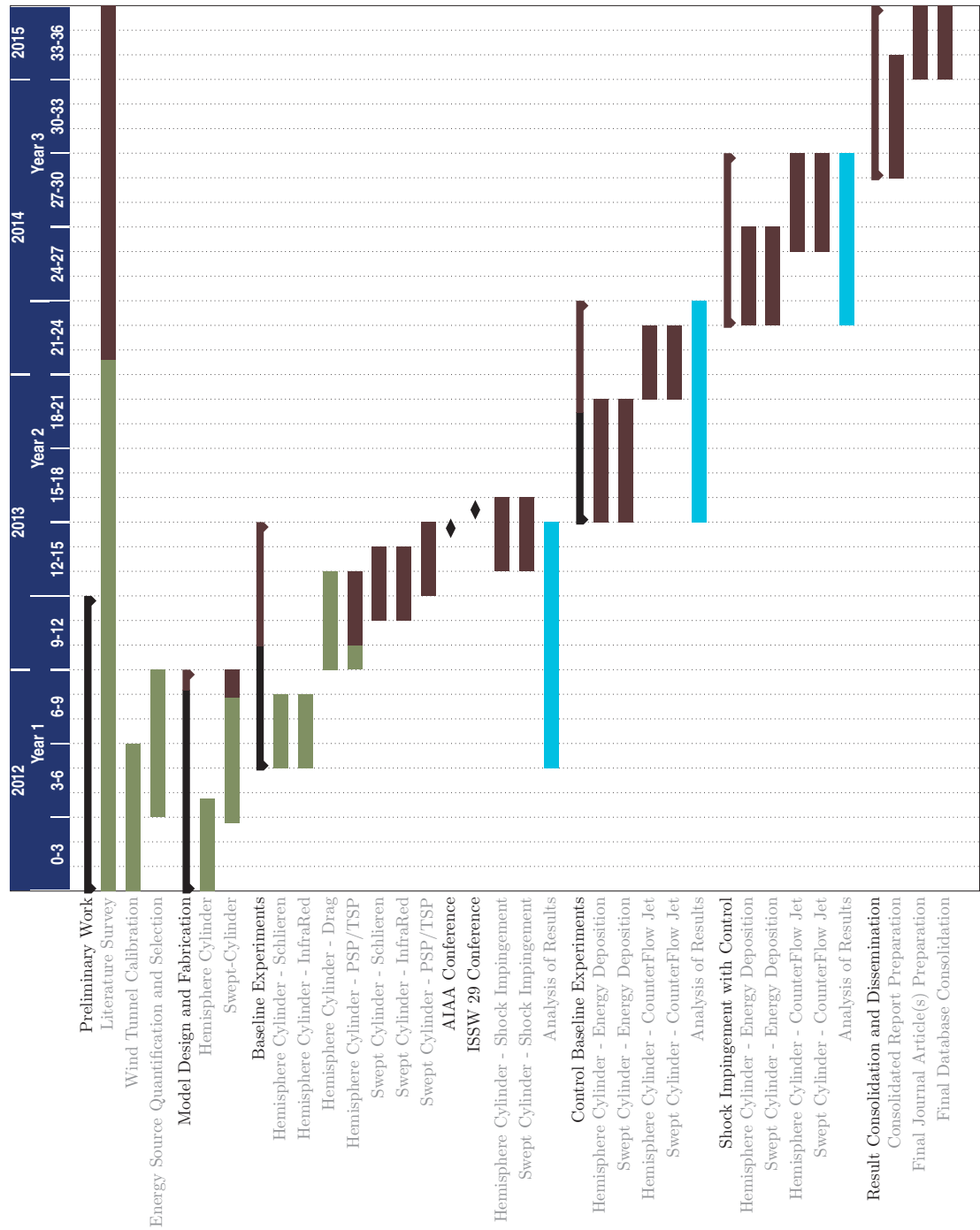


Figure 5.1: Proposed timeline of work for the coming year.

Bibliography

- [1] R. Adelgren, H. Yan, G. S. Elliott, D. D. Knight, T. J. Beutner, and A. A. Zheltovodov, “Control of edney iv interaction by pulsed laser energy deposition,” *AIAA journal*, vol. 43, no. 2, pp. 256–269, 2005.
- [2] S. B. H. Shah, S. Zahir, and I. Ahmed, “Numerical investigation on the effect of shock standoff distance due to counterflow jet injection from a hemispherical cylinder,” in *International Bhurban Conference on Applied Sciences and Technology*, (Islamabad, Pakistan), pp. 1–7, 2011.
- [3] J. Watts, “Flight experience with shock impingement and interference heating on the x-15-2 research airplane,” tech. rep., NASA TM X-1669, 1968.
- [4] J. Keyes and F. Hains, “Analytical and experimental studies of shock interference heating in hypersonic flows,” tech. rep., NASA TN D-7139, 1973.
- [5] R. Kandala and G. V. Candler, “Numerical studies of laser-induced energy deposition for supersonic flow control,” *AIAA journal*, vol. 42, no. 11, pp. 2266–75, 2004.
- [6] K. Anderson and D. Knight, “Thermal and aerodynamic effect of energy deposition on blunt body in supersonic flow,” in *49th AIAA Aerospace Sciences Meeting*, (Orlando, Florida), pp. 1–12, 2011.
- [7] J. S. S. Shang, “Shared knowledge in computational fluid dynamics, electromagnetics, and magneto-aerodynamics,” *Progress in aerospace sciences*, vol. 38, no. 6, pp. 449–467, 2002.

- [8] R. A. Newlander, "Effect of shock impingement on the distribution of heat-transfer coefficients on a right circular cylinder at mach numbers of 2.65, 3.51 and 4.44," tech. rep., NASA TN D-642, 1961.
- [9] H. S. Carter and R. E. Carr, "Free-flight investigation of heat transfer to an unswept cylinder subjected to an incident shock and flow interference from an upstream body at mach numbers up to 5.50," tech. rep., NASA TN D-988, 1961.
- [10] I. Beckwith, "Experimental investigation of heat transfer and pressures on a swept cylinder in the vicinity of its intersection with a wedge and flat plate at mach number 4.15 and high reynolds numbers," tech. rep., NASA TN D-2020, 1964.
- [11] R. A. Jones, "Heat-transfer and pressure investigation of a fin-plate interference model at a mach number of 6," tech. rep., NASA TN D-2028, 1964.
- [12] R. S. Hiers and W. J. Loubsky, "Effects of shock-wave impingement on the heat transfer on a cylindrical leading edge," tech. rep., NASA TN D-3859, 1967.
- [13] D. Bushnell, "Effects of shock impingement and other factors on leading edge heat transfer," tech. rep., NASA TN D-4543, 1968.
- [14] B. Edney, "Anomalous heat transfer and pressure distributions on blunt bodies at hypersonic speeds in the presence of an impinging shock," tech. rep., Aeronautical Research Institute of Sweden, FFA Report 115, 1968.
- [15] D. Morris and J. Keyes, "Computer programs for predicting supersonic and hypersonic interference flow fields and heating," tech. rep., NASA TM X-2725, 1973.
- [16] A. Wieting and M. S. Holden, "Experimental shock-wave interference heating on a cylinder at mach 6 and 8," *AIAA journal*, vol. 27, no. 11, pp. 1557–1565, 1989.
- [17] A. R. Weiting, *Experimental study of shock wave interference heating on a cylindrical leading edge*. PhD thesis, 1987.

- [18] M. S. Holden, J. R. Moselle, and J. Lee, "Studies of aerothermal loads generated in regions of shock/shock interaction in hypersonic flow," tech. rep., NASA CR-181893, 1991.
- [19] A. Wieting, "Multiple shock-shock interference on a cylindrical leading edge," *AIAA journal*, vol. 30, no. 8, pp. 2071–2079, 1992.
- [20] D. Gaitonde and J. Shang, "On the structure of an unsteady type iv interaction at mach 8," *Computers and fluids*, vol. 24, no. 4, pp. 469–485, 1995.
- [21] C. A. Lind and M. J. Lewis, "Unsteady characteristics of a hypersonic type iv shock interaction," *Journal of aircraft*, vol. 32, no. 6, pp. 1286–1293, 1995.
- [22] C. Lind and M. J. Lewis, "Computational analysis of the unsteady type iv shock interaction of blunt body flows," *Journal of propulsion and power*, vol. 12, no. 1, pp. 127–133, 1996.
- [23] C. Lind, "Effect of geometry on the unsteady type-iv shock interaction," *Journal of aircraft*, vol. 34, no. 1, pp. 64–71, 1997.
- [24] J. Olejniczak, M. J. Wright, and G. V. Candler, "Numerical study of inviscid shock interactions on double-wedge geometries," *Journal of fluid mechanics*, vol. 352, p. 1, 1997.
- [25] M. Frame and M. J. Lewis, "Analytical solution of the type iv shock interaction," *Journal of propulsion and power*, vol. 13, no. 5, pp. 601–609, 1997.
- [26] F. Grasso, C. Purpura, B. Chanetz, and J. Dlery, "Type iii and type iv shock/shock interferences: Theoretical and experimental aspects," *Aerospace science and technology*, vol. 7, no. 2, pp. 93–106, 2003.
- [27] V. N. Gusev and A. Y. Chinilov, "Interference of a bow shock with an oblique shock and an isentropic compression wave," *Fluid dynamics*, vol. 38, no. 4, p. 612, 2003.
- [28] V. Gusev and A. I. Erofeev, "Oblique shock/bow shock interference in rarefield flow past a cylinder," *Fluid dynamics*, vol. 39, no. 5, pp. 827–835, 2004.

- [29] Z. M. Hu, R. S. Myong, C.-H. Wang, T. H. Cho, and Z. L. Jian, "Numerical study of the oscillations induced by shock/shock interaction in hypersonic double-wedge flows," *Shock Waves*, vol. 18, no. 1, p. 41, 2008.
- [30] V. V. Riabov and A. B. Botin, "Numerical and experimental studies of shock interference in hypersonic flows near a cylinder," in *26th International Congress of the Aeronautical Sciences*, (Anchorage, Alaska, USA), 2008.
- [31] S. Shah, R. Martinez, N. Fernandez, and N. J. Mourtos, "Double wedge shockwave interaction flow characterization," in *Thermal and Fluids Analysis Workshop*, (San Jose), 2008.
- [32] Z. M. Hu, R. S. Myong, Y. R. Yang, and T. H. Cho, "Reconsideration of inviscid shock interactions and transition phenomena on double-wedge geometries in a $M=9$ hypersonic flow," *Theoretical and computational fluid dynamics*, vol. 24, no. 6, p. 551, 2010.
- [33] G. Tchien, Y. Burtschell, and D. E. Zeitoun, "Numerical study of the interaction of type ivr around a double-wedge in hypersonic flow," *Computers and fluids*, vol. 50, no. 1, pp. 147–154, 2011.
- [34] Y.-B. Chu and X.-Y. Lu, "Characteristics of unsteady type iv shock/shock interaction," *Shock Waves*, vol. 22, no. 3, pp. 225–235, 2012.
- [35] D. Riggins, H. Nelson, and E. Johnson, "Blunt-body wave drag reduction using focused energy deposition," *AIAA journal*, vol. 37, no. 4, pp. 460–467, 1999.
- [36] D. W. Riggins and H. F. Nelson, "Hypersonic flow control using upstream focused energy deposition," *AIAA journal*, vol. 38, no. 4, pp. 723–5, 2000.
- [37] V. Soloviev, V. Krivtsov, and A. M. Konchakov, "Drag reduction by plasma filaments over supersonic forebodies," *AIAA journal*, vol. 41, no. 12, pp. 2403–2409, 2003.
- [38] D. M. Bushnell, "Shock wave drag reduction," *Annual Review of Fluid Mechanics*, vol. 36, pp. 81–96, 2004.

- [39] L. Myrabo, Y. P. Raizer, M. Shneider, and R. Bracken, "Reduction of drag and energy consumption during energy release preceding a blunt body in supersonic flow," *High temperature*, vol. 42, no. 6, pp. 890–899, 2004.
- [40] I. Girgis, M. Shneider, S. Macheret, G. L. Brown, and R. B. Miles, "Steering moments creation in supersonic flow by off-axis plasma heat addition," *Journal of spacecraft and rockets*, vol. 43, no. 3, pp. 607–613, 2006.
- [41] J. Shang, J. Hayes, W. Strang, and K. Wurtzler, "Jet-spike bifurcation in high-speed flows," *AIAA Journal*, vol. 39, no. 6, pp. 1159–1165, 2001.
- [42] V. Fomin, A. Maslov, A. Shashkin, T. Korotaeva, and N. Malmuth, "Flow regimes formed by a counterflow jet in a supersonic flow," *Journal of Applied Mechanics and Technical Physics*, vol. 42, no. 5, pp. 757–764, 2001.
- [43] B. Venukumar, G. Jagadeesh, and K. Reddy, "Counterflow drag reduction by supersonic jet for a blunt body in hypersonic flow," *Physics of fluids*, vol. 18, pp. 118104: 1–4, 2006.
- [44] E. O. Daso, V. E. Prichett, T.-S. Wang, D. K. Ota, I. M. Blankson, and A. H. Auslender, "Dynamics of shock dispersion and interactions in supersonic freestreams with counterflowing jets," *AIAA Journal*, vol. 47, no. 6, pp. 1313–1326, 2009.
- [45] A. Oliveira, M. Minucci, P. Toro, J. C. Jr, L. Myrabo, and H. Nagamatsu, "Bow shock wave mitigation by laser-plasma addition in hypersonic flow," *Journal of spacecraft and rockets*, vol. 45, no. 5, pp. 921–927, 2008.
- [46] T. Sakai, Y. Sekiya, K. Mori, and A. Sasoh, "Interaction between laser-induced plasma and shock wave over a blunt body in a supersonic flow," *Proceedings of the Institution of Mechanical Engineers; Part G; Journal of Aerospace Engineering*, vol. 222, pp. 605–617, 2008.
- [47] A. Sasoh, Y. Sekiya, T. Sakai, J.-H. Kim, and A. Matsuda, "Supersonic drag reduction with repetitive laser pulses through a blunt body," *AIAA journal*, vol. 48, no. 12, pp. 2811–2817, 2010.

- [48] D. Knight, "Survey of aerodynamic drag reduction at high speed by energy deposition," *Journal of propulsion and power*, vol. 24, no. 6, pp. 1153–1167, 2008.
- [49] D. J. Romeo and J. R. Sterrett, "Exploratory investigation of the effect of a forward-facing jet on the bow shock of a blunt body in a mach number 6 free stream," tech. rep., NASA TN D-1605, 1958.
- [50] P. Finley, "The flow of a jet from a body opposing a supersonic free stream," *Journal of Fluid Mechanics*, vol. 26, no. 2, pp. 337–370, 1966.
- [51] L. Yang, E. Erdem, H. Zare-Behtash, K. Kontis, and S. Saravanan, "Pressure-sensitive paint on a truncated cone in hypersonic flow at incidences," *International Journal of Heat and Fluid Flow.*, vol. 37, pp. 9–21, 2012.
- [52] E. Erdem, *Active Flow Control Studies at Mach 5: Measurement and Computation*. PhD thesis, University of Manchester, 2011.
- [53] K. Kontis, *Projectile Aerodynamics: Measurement and Computation*. PhD thesis, Cranfield College of Aeronautics, 1997.
- [54] M. Quinn, L. Yang, and K. Kontis, "Pressure-sensitive paint: Effect of substrate," *Sensors*, vol. 11, pp. 11649–11663, 2011.
- [55] T. Liu and J. P. Sullivan, *Pressure and Temperature Sensitive Paints*. Experimental Fluid Mechanics, Berlin: Springer-Verlag, 2005.
- [56] H. Zare-Behtash, N. Gongora-Orozco, C. Lada, and K. Kontis, "Application of pressure sensitive paint measurements to complex flows," in *46th AIAA Aerospace Sciences Meeting and Exhibit*, 2008.
- [57] H. Zare-Behtash, N. Gongora-Orozco, K. Kontis, and S. Holder, "Application of novel pressure-sensitive paint formulations for the surface flow mapping of high-speed jets," *Experimental thermal and fluid science*, vol. 33, no. 5, pp. 852–864, 2009.
- [58] M. I. J. Stich, S. Nagl, O. S. Wolfbeis, U. Henne, and M. Schaeferling, "A dual luminescent sensor material for simultaneous imaging of pressure and temperature on surfaces," *Advanced Functional Materials*, vol. 18, no. 9, pp. 1399–1406, 2008.

- [59] M. I. J. Stich, O. S. Wolfbeis, and U. Resch-Genger, “Fluorescence sensing and imaging using pressure-sensitive paints and temperature-sensitive paints standardization and quality assurance in fluorescence measurements i,” vol. 5 of *Springer Series on Fluorescence*, pp. 429–461, Springer Berlin Heidelberg, 2008.
- [60] R. Hooke, “Micrographia,” 1665.
- [61] G. Settles, *Schlieren and Shadowgraph Techniques: Visualizing Phenomena in Transparent Media*. Berlin: Springer-Verlag, 2001.
- [62] T. P. Davies, “Schlieren photography-short bibliography and review,” *Optics and laser technology*, vol. 13, no. 1, pp. 37–42, 1981.
- [63] E. Erdem, K. Kontis, and L. Yang, “Steady energy deposition at mach 5 for drag reduction,” *Shock Waves*, pp. 1–14, 2012.
- [64] M. Raffel, C. E. Willert, S. T. Wereley, and J. Kompenhans, *Particle Image Velocimetry*. Berlin: Springer-Verlag, 2007.
- [65] N. Gongora-Orozco, H. Zare-Behtash, and K. Kontis, “Particle image velocimetry studies on shock wave diffraction with freestream flow,” in *48th AIAA Aerospace Sciences Meeting Including the New Horizons Forum and Aerospace Exposition*, 2010.
- [66] F. F. J. Schrijer, F. Scarano, and B. W. van Oudheusden, “Application of piv in a mach 7 double-ramp flow,” *Experiments in fluids*, vol. 41, pp. 353–363, 2006.
- [67] F. Scarano, *Overview of PIV in supersonic flows Particle image velocimetry : new developments and recent applications : Topics in applied physics*. 2008.
- [68] J. Wilson, “Laser-induced multiple breakdown in gases,” *Journal of physics. D, Applied physics*, vol. 3, no. 12, pp. 2005–2008, 1970.
- [69] D. DeWitt and G. Nutter, *Theory and practice of radiation thermometry*. New York: Wiley, 1989.
- [70] G. Cardone, A. Ianiro, G. d. Ioio, and A. Passaro, “Temperature maps measurements on 3d surfaces with infrared thermography,” *Experiments in fluids*, vol. 52, no. 2, pp. 375–385, 2012.

- [71] G. Simeonides, J. Vermeulen, H. L. Boerrigter, and J. Wendt, “Quantitative heat transfer measurements in hypersonic wind tunnels by means of infrared thermography,” *IEEE Transactions on Aerospace and Electronic Systems*, vol. 29, no. 3, pp. 878–93, 1993.
- [72] Y. L. Sant, M. Marchand, P. Millan, and J. Fontaine, “An overview of infrared thermography techniques used in large wind tunnels,” *Aerospace science and technology*, vol. 6, no. 5, pp. 355–66, 2002.
- [73] G. Carlomagno and G. Cardone, “Infrared thermography for convective heat transfer measurements,” *Experiments in fluids*, vol. 49, no. 6, pp. 1187–1218, 2010.
- [74] C. Substrates and C. Ltd, “Macor - properties.” http://www.macor.info/macor_properties.html, 2012. Online; accessed 24-September-2012.
- [75] E. Erdem, L. Yang, and K. Kontis, “Drag reduction by energy deposition in hypersonic flows,” in *16th AIAA/DLR/DGLR International Space Planes and Hypersonic Systems and Technologies Conference*, International Space Planes and Hypersonic Systems and Technologies Conferences, American Institute of Aeronautics and Astronautics, 2009. 2012/09/26 0 doi:10.2514/6.2009-7347.
- [76] E. Erdem and K. Kontis, “Numerical and experimental investigation of transverse injection flows,” *Shock Waves*, vol. 20, no. 2, pp. 103–118, 2010.
- [77] J. Fay and F. Riddell, “Theory of stagnation point heat transfer in dissociated air,” *Journal of the Aeronautical Sciences*, vol. 25, no. 2, pp. 73–85, 1958.

APPENDIX A:

Presentation on Edney Type IV Interactions

DEVELOPMENT AND APPLICATION OF LASER-INDUCED ENERGY DEPOSITION FOR FLOW CONTROL

Investigators:

Dr Erinc Erdem (PDRA)

Professor Konstantinos Kontis (PI)

Distribution A: Approved for public release; distribution is unlimited.

Objectives

- Evaluate the effect of pulse laser-induced energy deposition on the instantaneous surface heat transfer and pressure for a number of configurations including Edney IV;
- Develop a rational methodology for determining the optimal laser discharge energy and location to minimize the peak heat transfer.
- Approach: Wind tunnel tests using flow visualisation including Schlieren, PIV, pressure measurements using PSP, strain gauge balance, IR thermography.

Main Results (Year 1)

- Wind tunnel calibration; Models design and fabrication; Energy source design and fabrication; Discharge characterization and quantification; Literature survey; Preliminary model verification and initial experiments.
- Future Plans (Years 2 and 3):
- Experiments using a series of geometries; analysis of results;

Outline

- Motivation for Research
 - Description of Phenomenon
 - Project Topic
- Research Activities
 - Literature Review
 - Experimental Results
- Moving forward

Motivation for Research

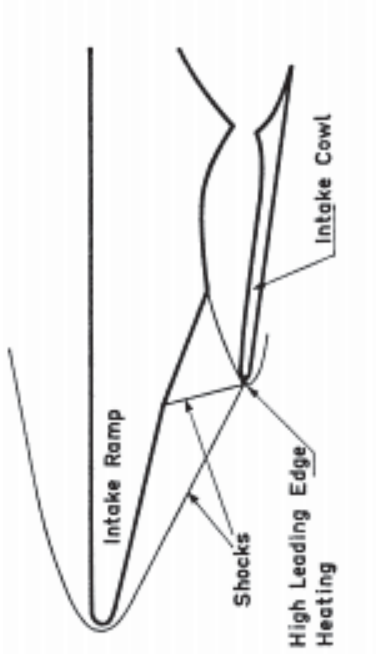
- Shock impingements cause high pressure and heat at the surface of a blunt body.
- First observed experimentally in 1964 when a blunt body was raised into Mach 4.6 flow.
- In 1967, X-15A-2 suffered catastrophic damage to a support fin due to shock impingement



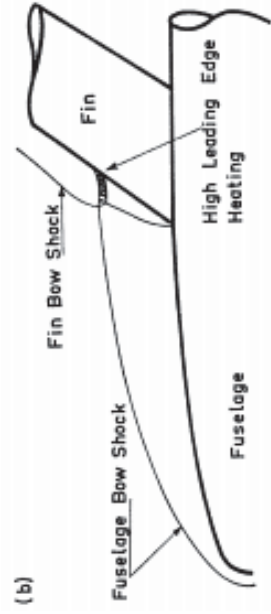
Shock impingement damage to support fin

Motivation for Research (cont'd)

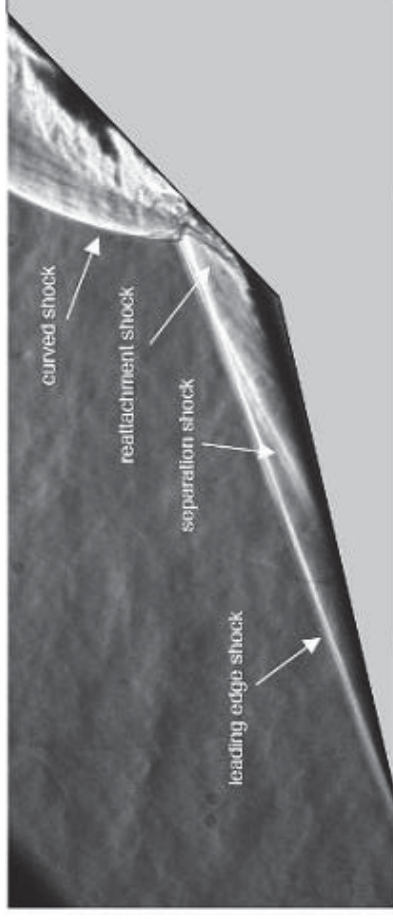
- X-15 experienced shock impingement heating on wings and cockpit canopy
- Other places of impingement:
 - Ram-jet cowl inlet
 - Booster tank on missile
 - Double wedge configurations
 - Splitter plate and fin



Ram-jet inlet impingement



Wing/fin impingement



Double wedge ramp impingement

Description of Phenomenon

- Most important work by Edney in 1968
- Looked at an oblique shock hitting a bow shock at different locations
- Classified shock interactions into six types

Type I Interaction

- Impinging shock impinges well below the lower sonic line. This causes two more shocks, as in a regular Mach reflection. A shear layer is also formed.

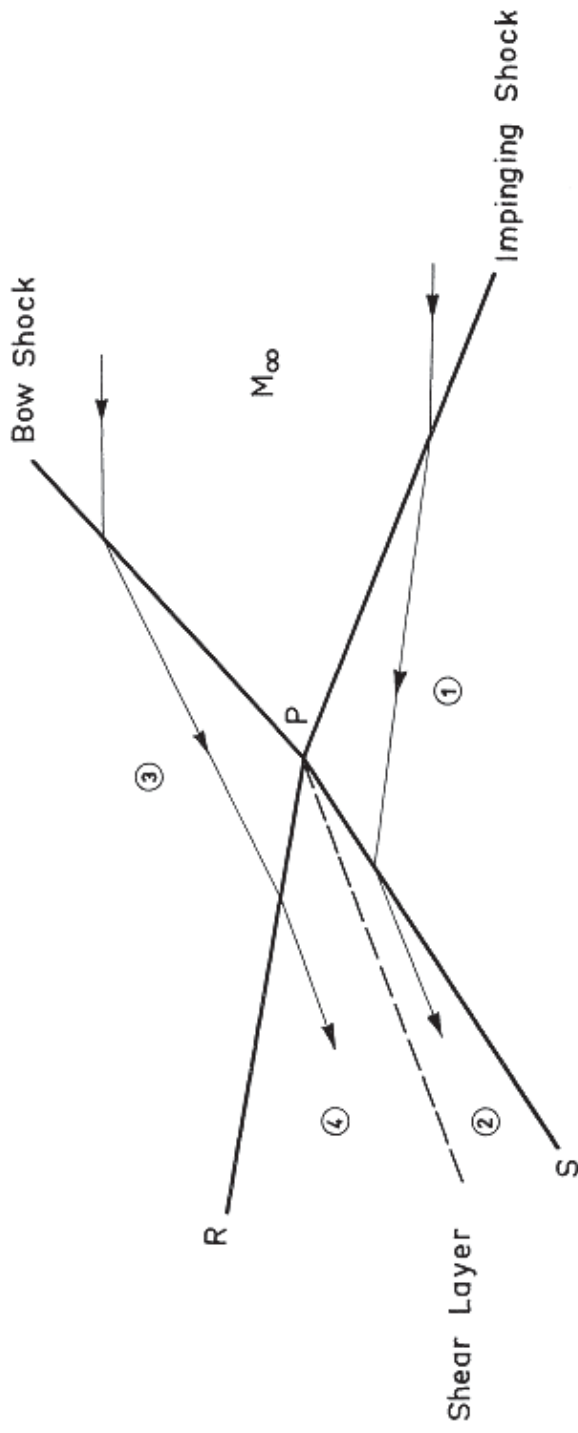


Fig. 6.1. Type I Interaction, $M = 4.6$, $\xi = 10^\circ$.

Diagram of Type I Interaction

Type II Interaction

- Incident shock impinges just below the lower sonic line. Two triple points are formed, separated by an almost normal shock. A shear layer is formed at each triple point.

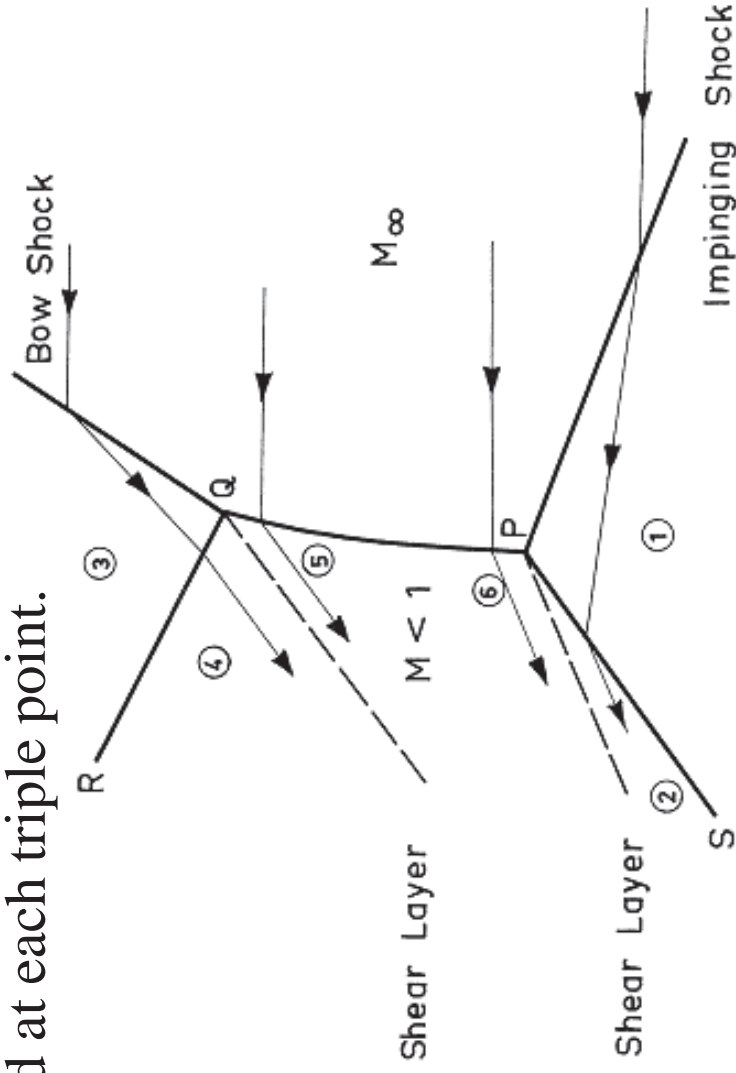
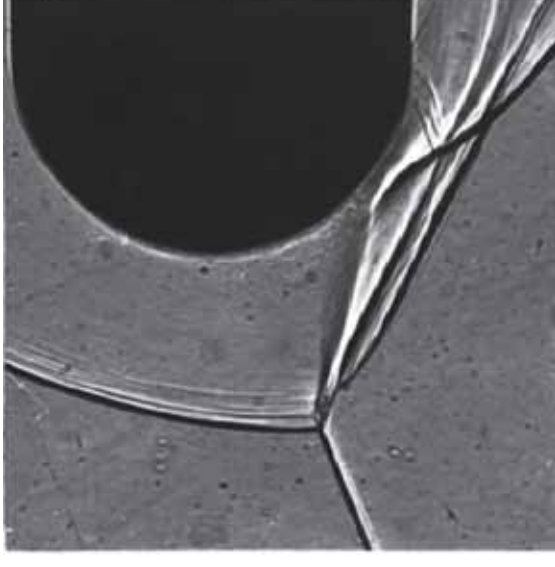


Fig. 6.6. Type II interference, $M=4.6$, $\xi=10^\circ$.

Diagram of Type II Interaction

Type III Interaction

- Incident shock impinges within subsonic region. A slip/shear layer is created which then attaches to the body. Large dynamic and thermal loads are experienced at the attachment point.



Schlieren image of Type III interaction

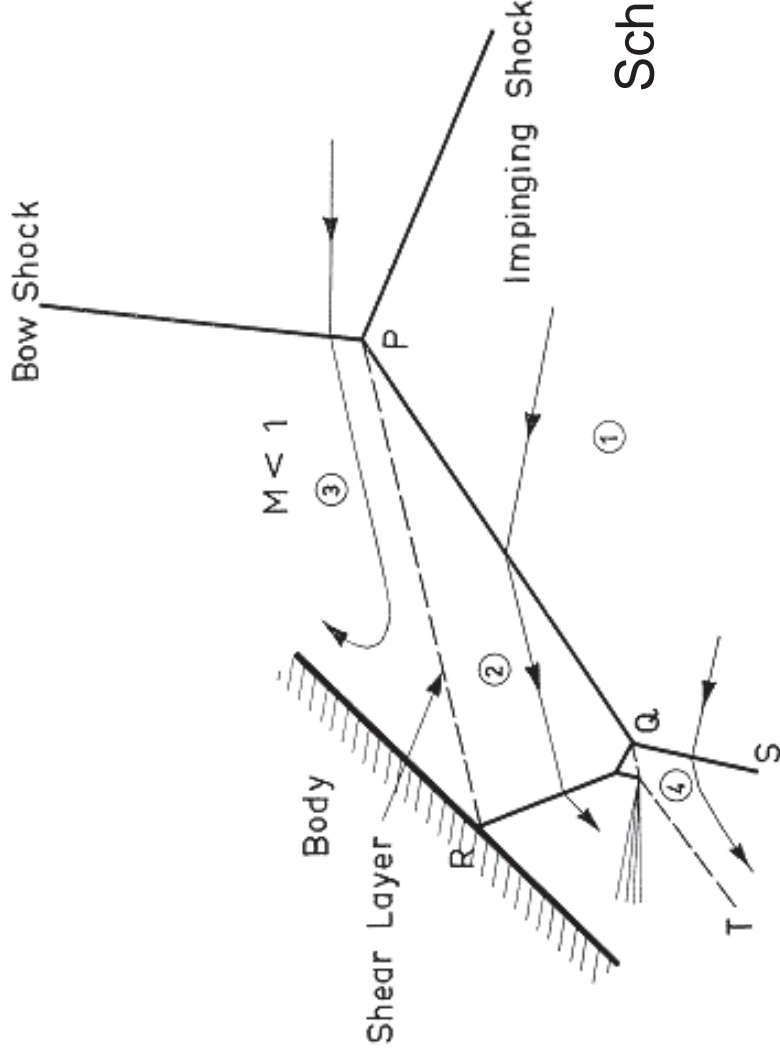


Diagram of Type III Interaction

Type IV Interaction

- Incident shock impinges within subsonic region. When the impingement point is such that reattachment is not possible, due to the high turn angle required, a supersonic jet forms and impinges on the surface, greatly increasing the pressure and heat.

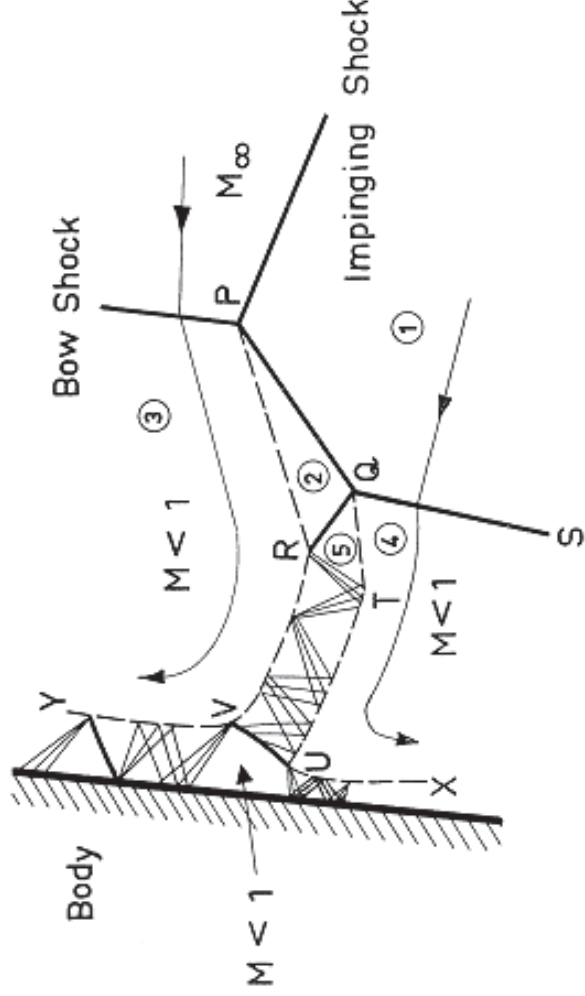
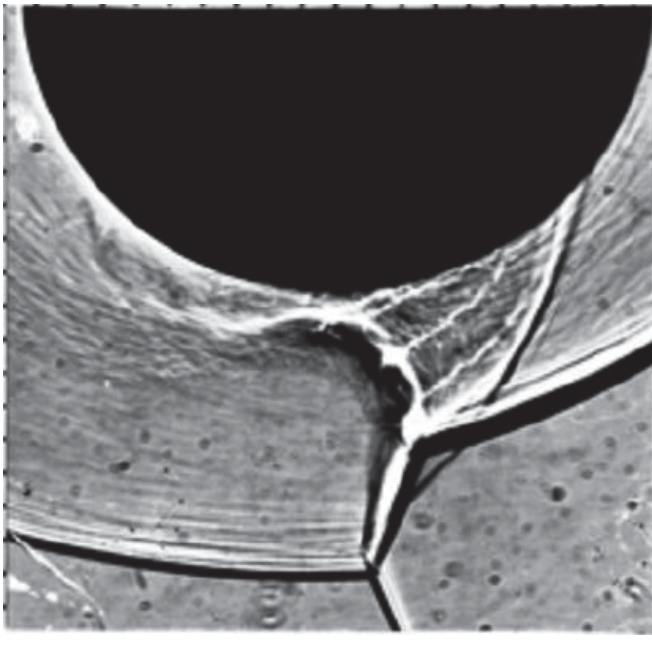


Diagram of Type IV Interaction



Schlieren image of Type IV interaction

Type V Interaction

- Incident shock impinges just about the upper sonic limit. This shock type is analogous to Type II, with the exception that jets form instead of the shear layer.

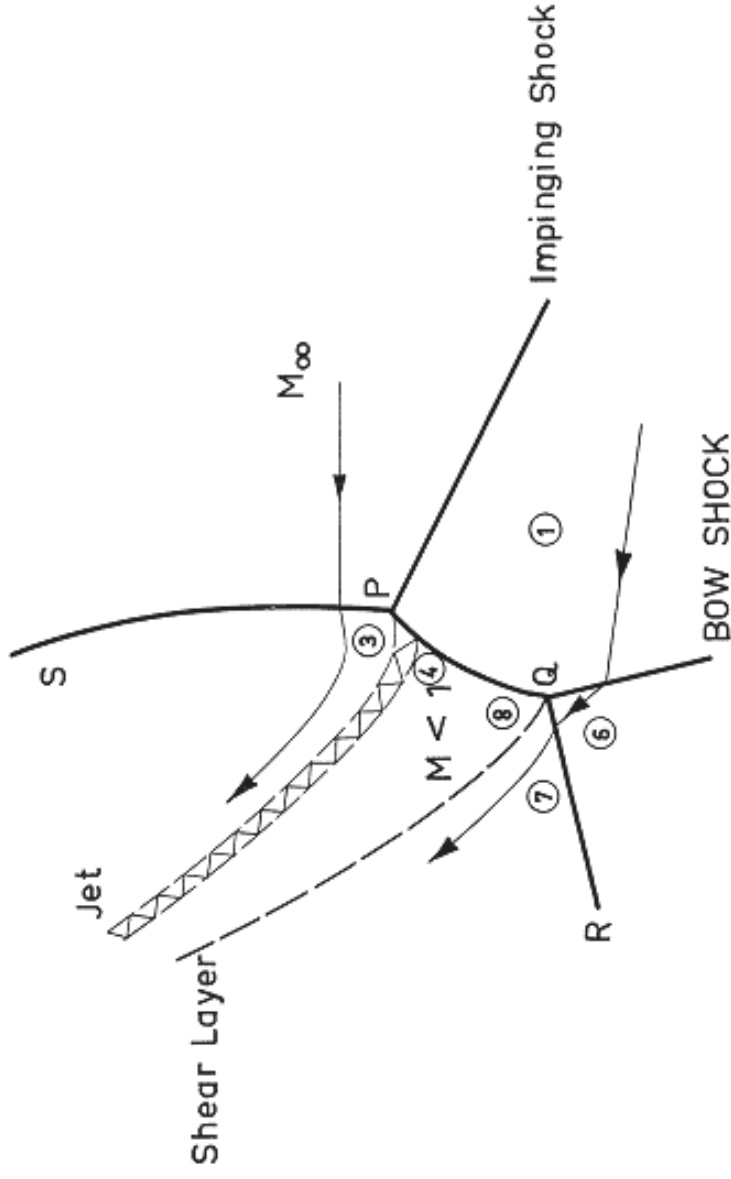


Fig. 6.1-1. Type V interference, $M = 4.6$, $\frac{h}{s} = 10^\circ$.

Diagram of Type V Interaction

Type VI Interaction

- Incident shock impinges well above the sonic limit. The impingement point produces an expansion fan as well as a shear layer.

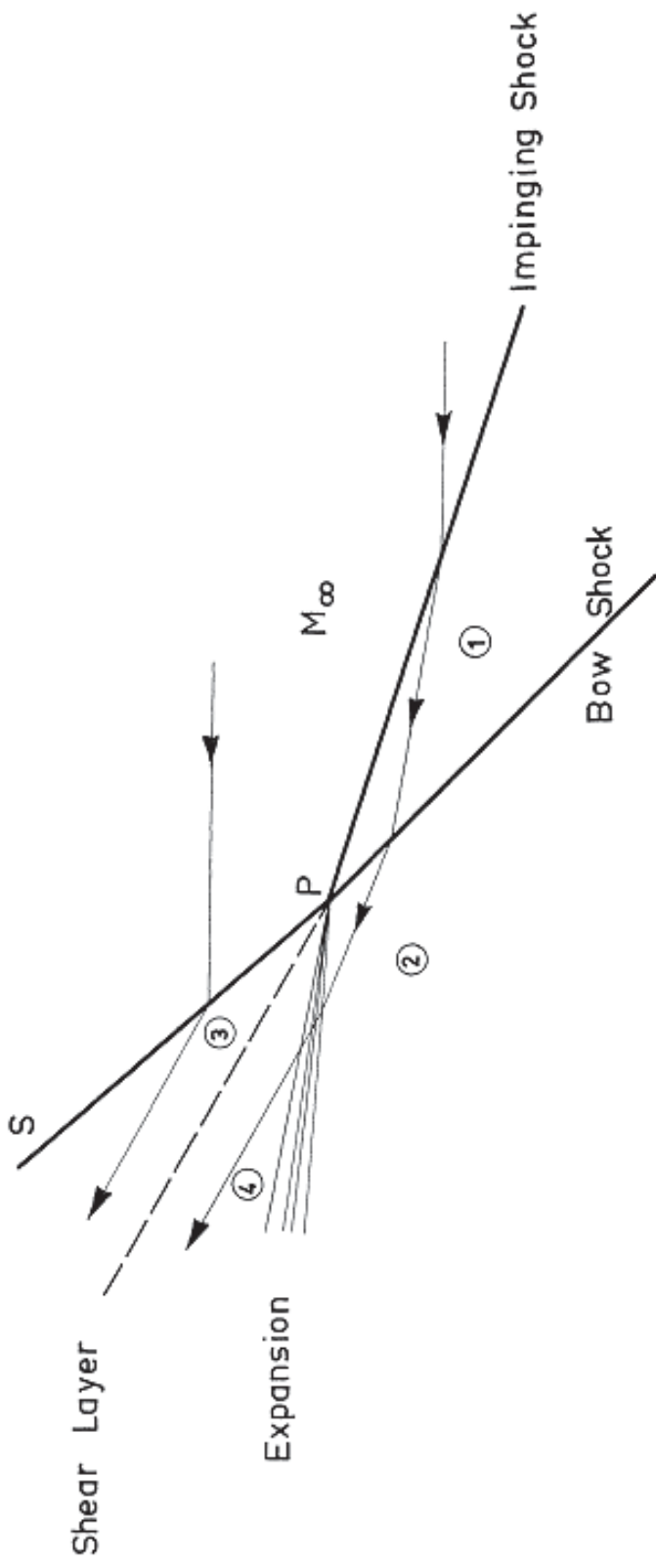
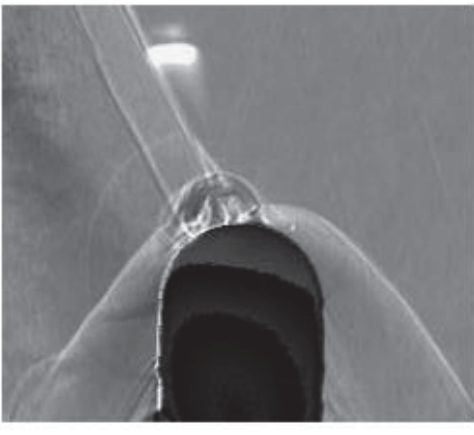


Fig. 6.16, Type VI interference, $M = 4.6$, $\xi = 10^\circ$.

Diagram of Type VI Interaction

Edney Interactions

- Most important interactions – Type III and IV
- These give greatest increase in heat and pressure
- One way to avoid these interactions is through good design
- However in off-design scenarios (roll, yaw, pitch), Edney III or IV interactions might arise
- If not controlled, the interactions could be catastrophic
- One control method is the use of Laser Energy Deposition



Laser Energy Deposition for
Edney IV Interaction

Pressure modulation

- Adelgren et al. (2007): **single** pulse yields momentary reduction in surface pressure by 40%

Ultimate goal:

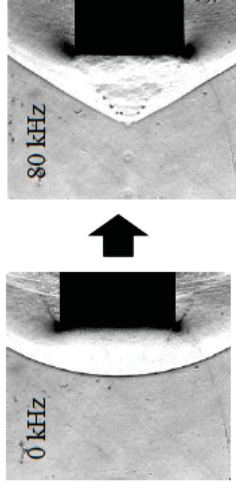
Fly By **Light** Power

- (Optical, Low & Light weight)
- non-extensive maneuvering
- high L/D
- more effective to hypersonic flow

-Knight et al. (2007): Review article

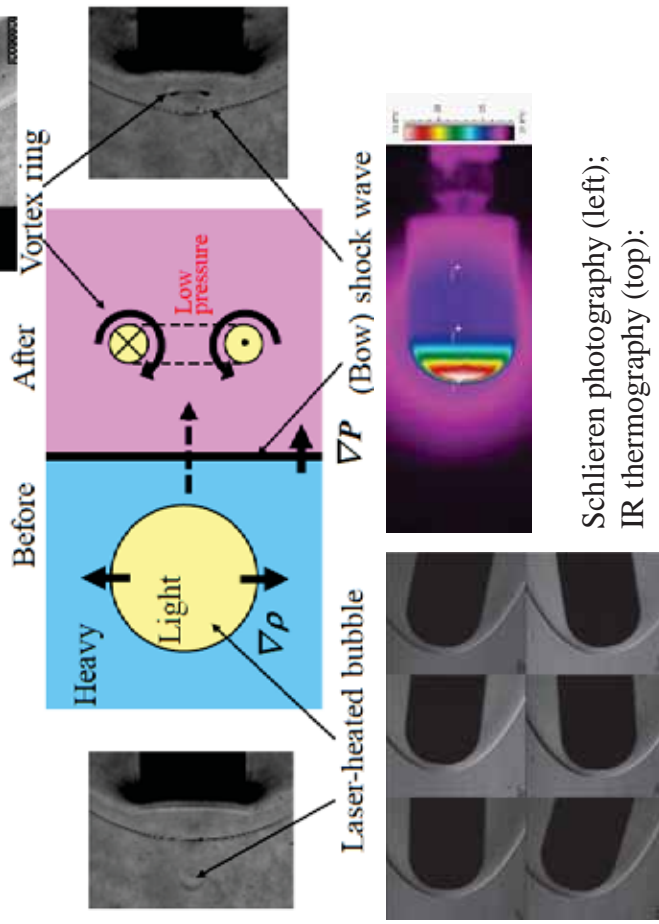
Morphing w/ **repetitive** pulses

- Tret'yakov et al. (1996): 45 % drag reduction @ $\eta < 1$, $M=2$ (argon), $f = 100\text{kHz}$
- Kim et al.(2011): 21% drag reduction @ $\eta = 6$, $M=2$ (air), $f < 80\text{kHz}$



Generation of Vortex Ring after Baroclinic Interaction

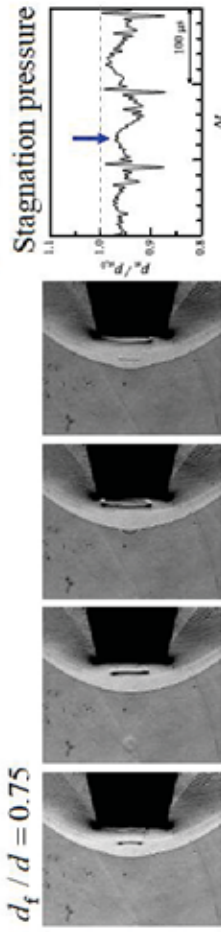
$$\frac{d\omega}{dt} = (\omega \cdot \nabla)\mathbf{u} - \omega(\nabla \cdot \mathbf{u}) + \underbrace{\frac{1}{\rho^2} \nabla \rho \times \nabla P}_{\text{Baroclinic term}}$$



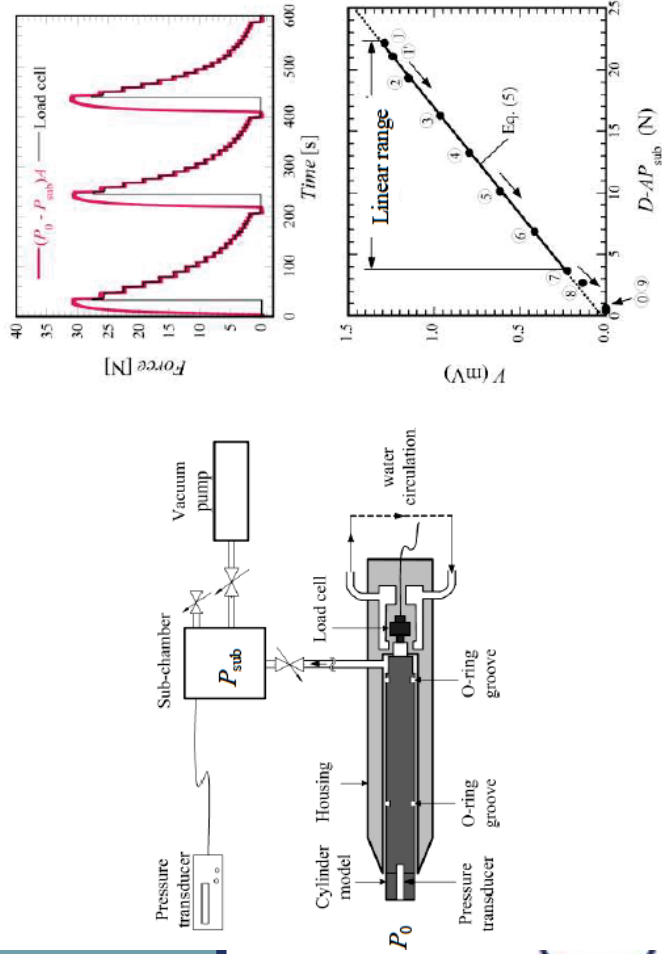
Increase in Vortex-Ring Residence Time Using Larger Base

$E=7.2\text{mJ/pulse}$, $f=10\text{kHz}$

$d_t/d = 0.75$



Drag Measurement and Calibration



Edney IV

- Controlling Edney Type IV interactions using pulsed laser energy deposition (LED)
- Want to see the best place for LED so as to control/minimize effects of Edney Type IV interactions
- Two Experimental Models
- Hemisphere-Cylinder
 - 25 mm Diameter
 - Angle of attack = $\pm 20^\circ$
- Swept Cylinder
 - 25 mm Diameter
 - Sweep angle = $\pm 45^\circ$
- Shock generator for both must be able to change angle to flow from 0 to 12 degrees

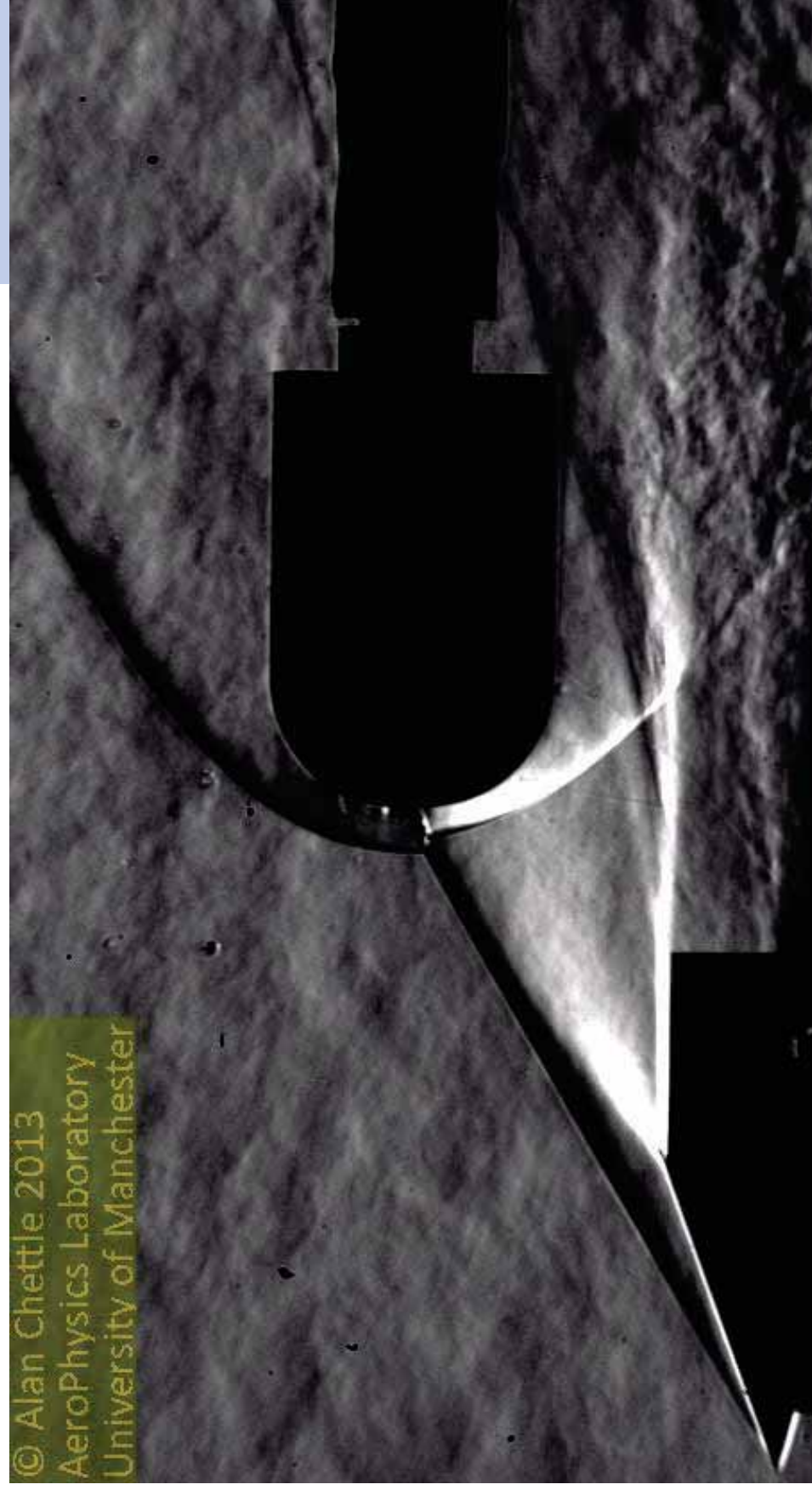
Research Activities

- Literature Review
 - Hypersonic Flow Control
 - Edney Interactions
 - Type IV Interactions
 - Laser Energy Deposition
 - Swept Cylinder (Hypersonic)
 - Hemisphere-cylinder (Hypersonic)
 - PSP/TSP,IR, Thin-film temperature gauges
 - Schlieren
 - Counter-flow jet control

Experimental Setup

- Hypersonic Wind Tunnel
 - $T_0 = 375 \text{ K}$
 - $P_0 = 6.45 \text{ Bar}$
 - $Re = 13 \times 10^6 / \text{m}$
- Hemisphere cylinder placed on three-component force balance
- Shockwave generator with variable position relative to model

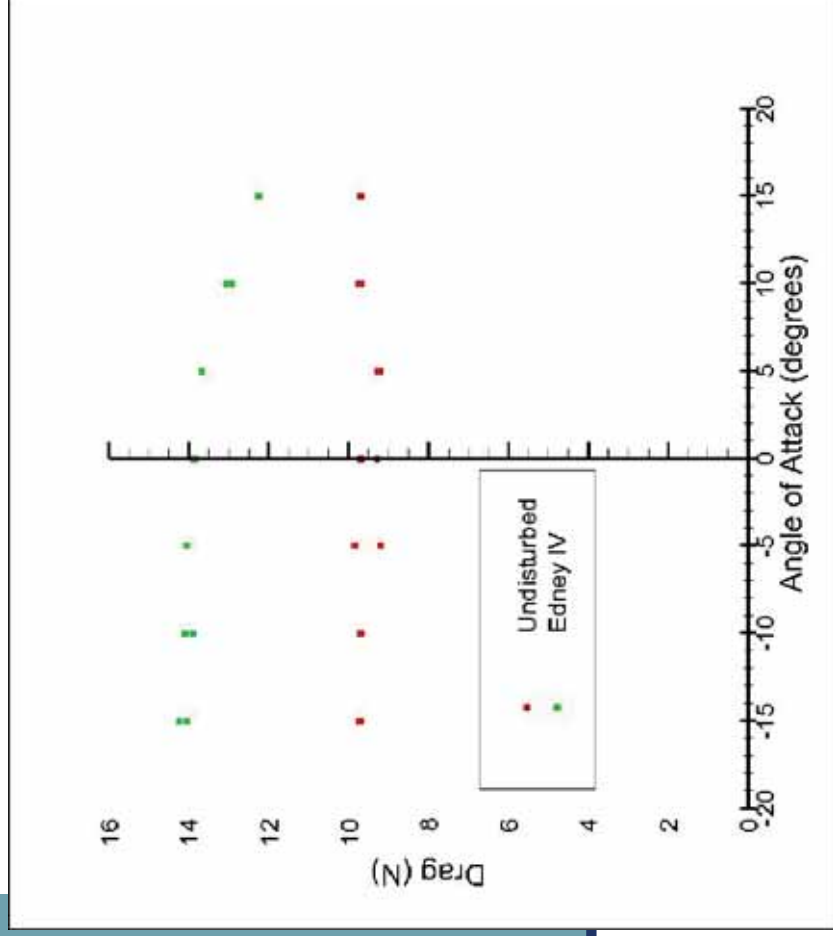
Experimental Results



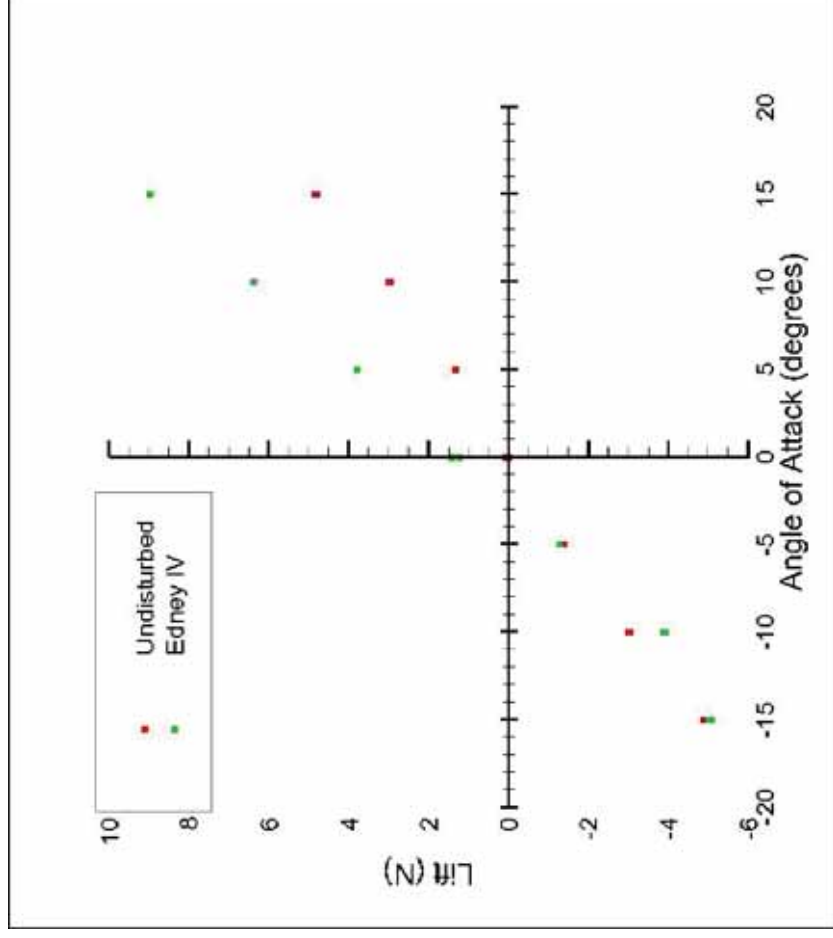
Distribution A: Approved for public release; distribution is unlimited.

Experimental Results

Drag vs Angle of Attack



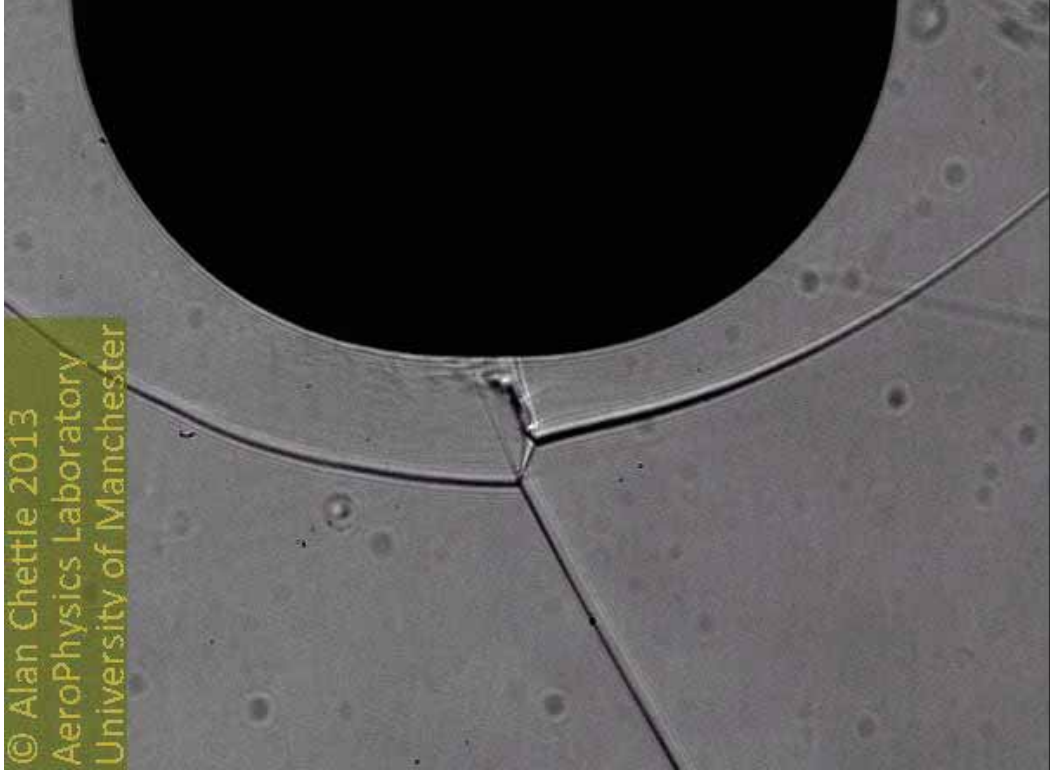
Lift vs Angle of Attack



Experimental Results

0 Degrees

© Alan Chettle 2013
AeroPhysics Laboratory
University of Manchester

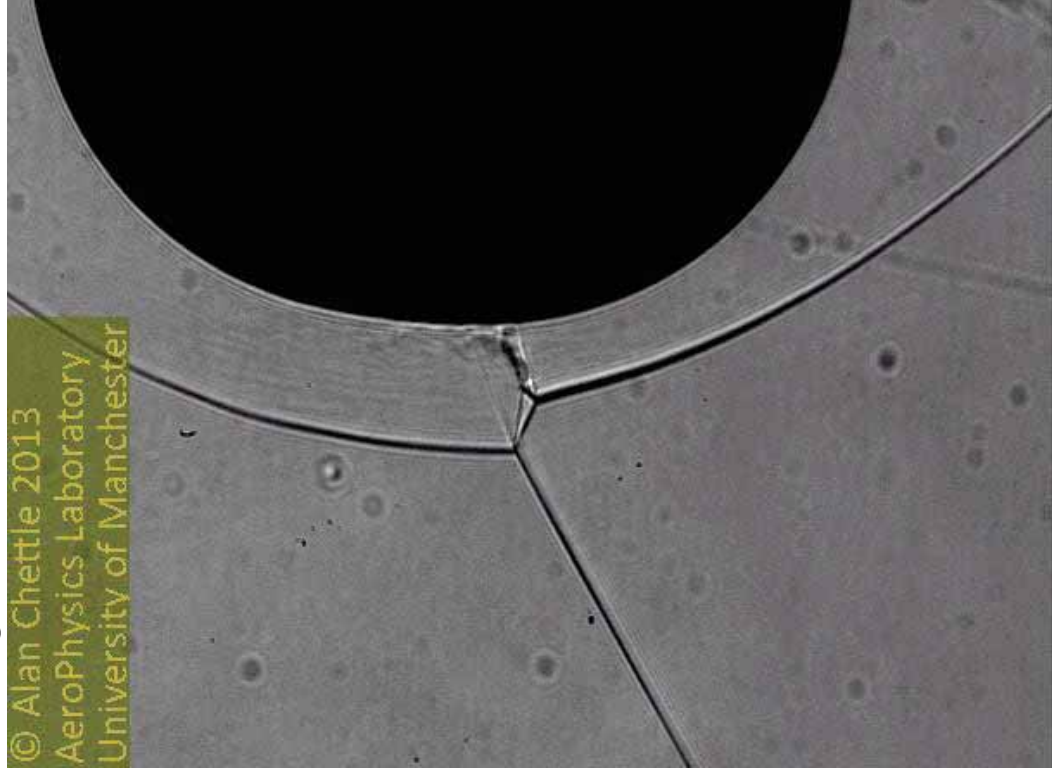


- Shadowgraph was used to capture details of Edney Type IV interaction

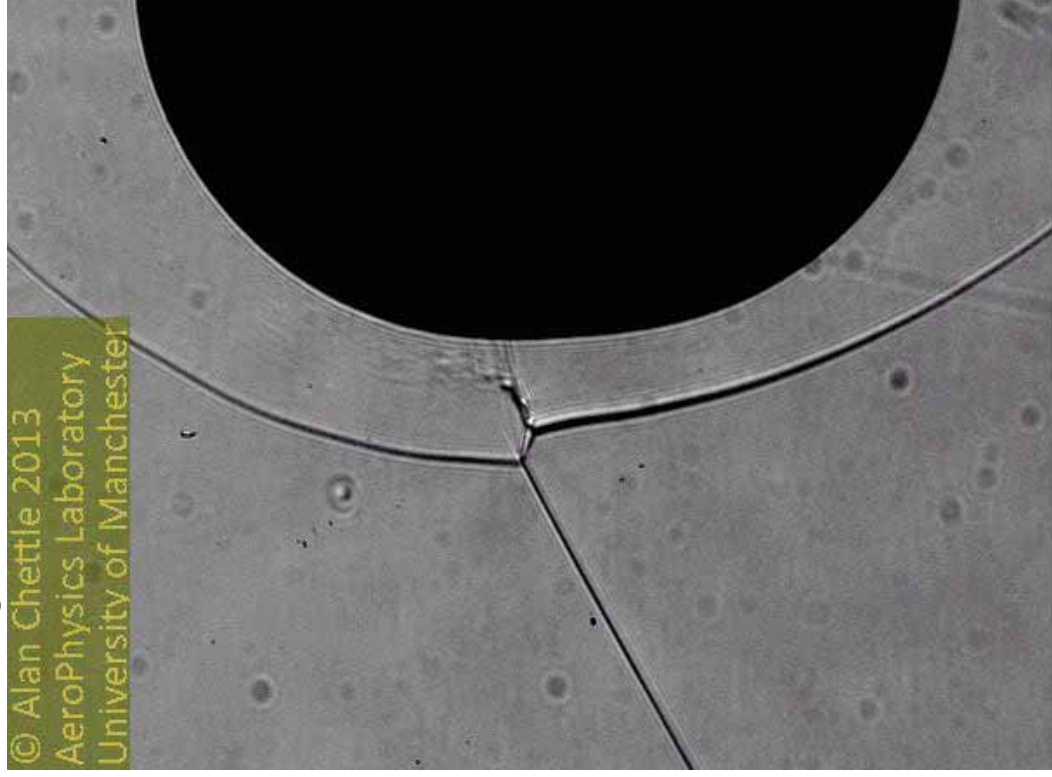


Experimental Results

5 Degrees

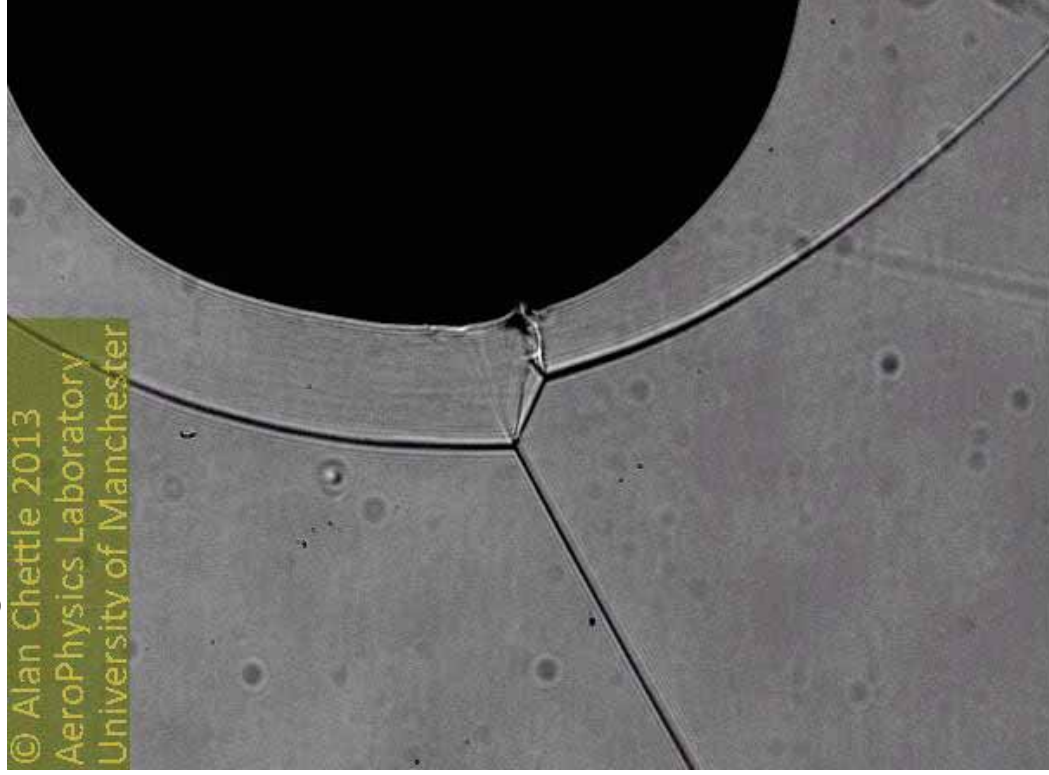


-5 Degrees

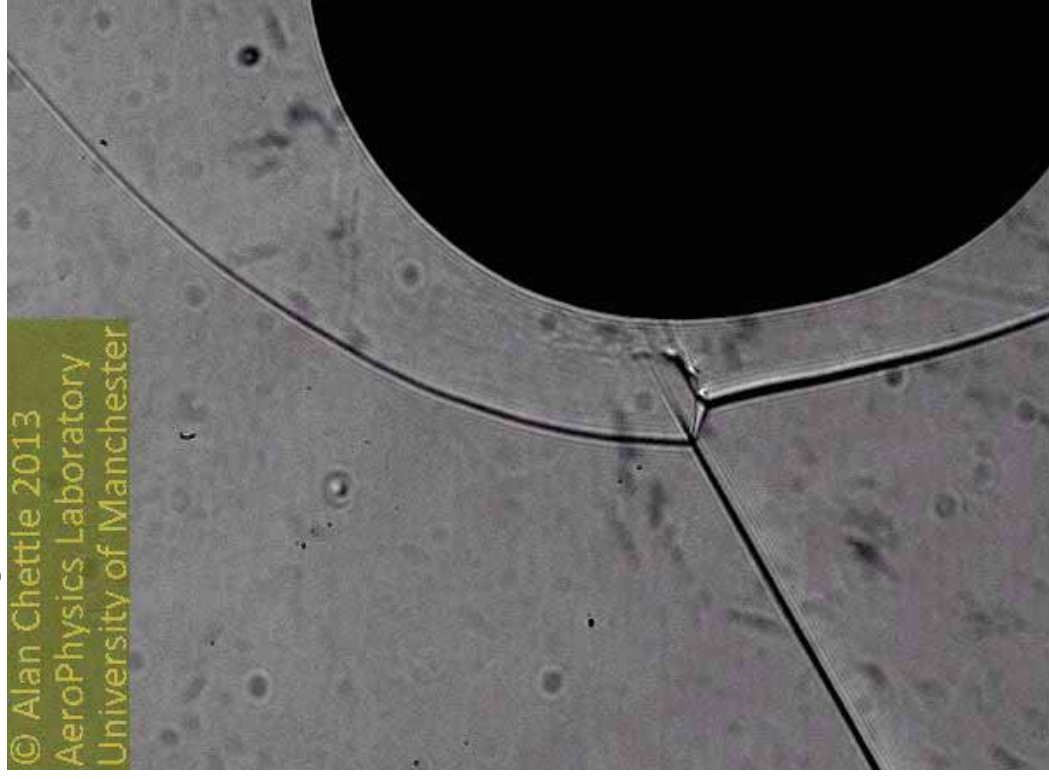


Experimental Results

10 Degrees

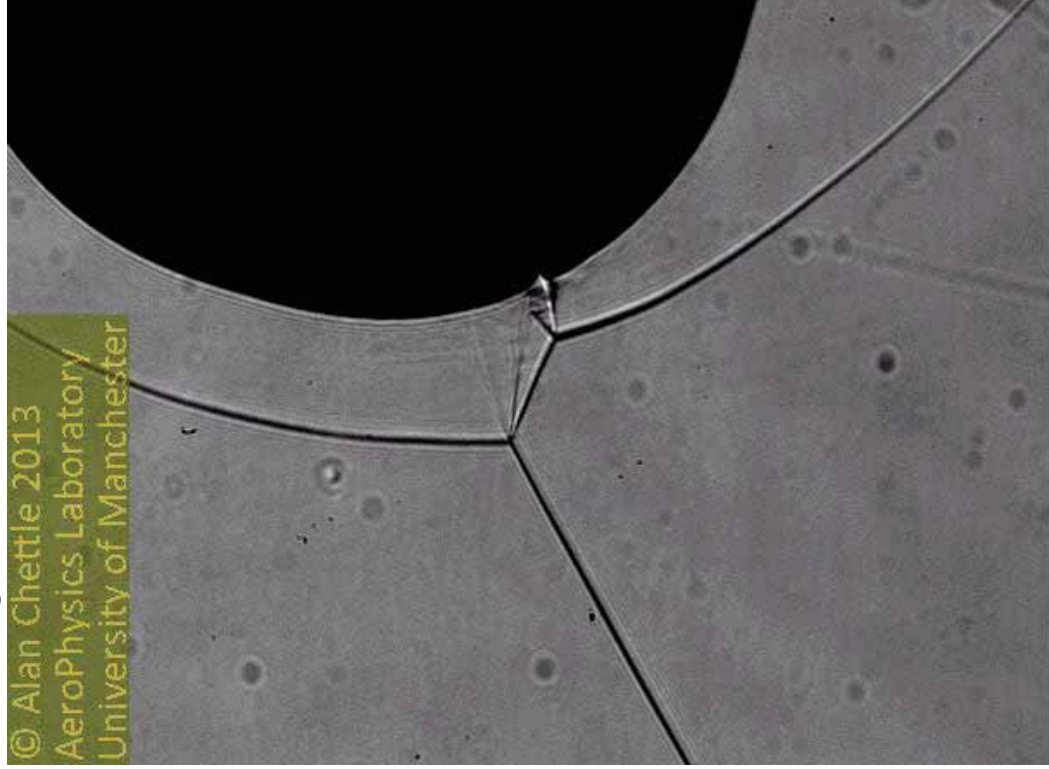


-10 Degrees

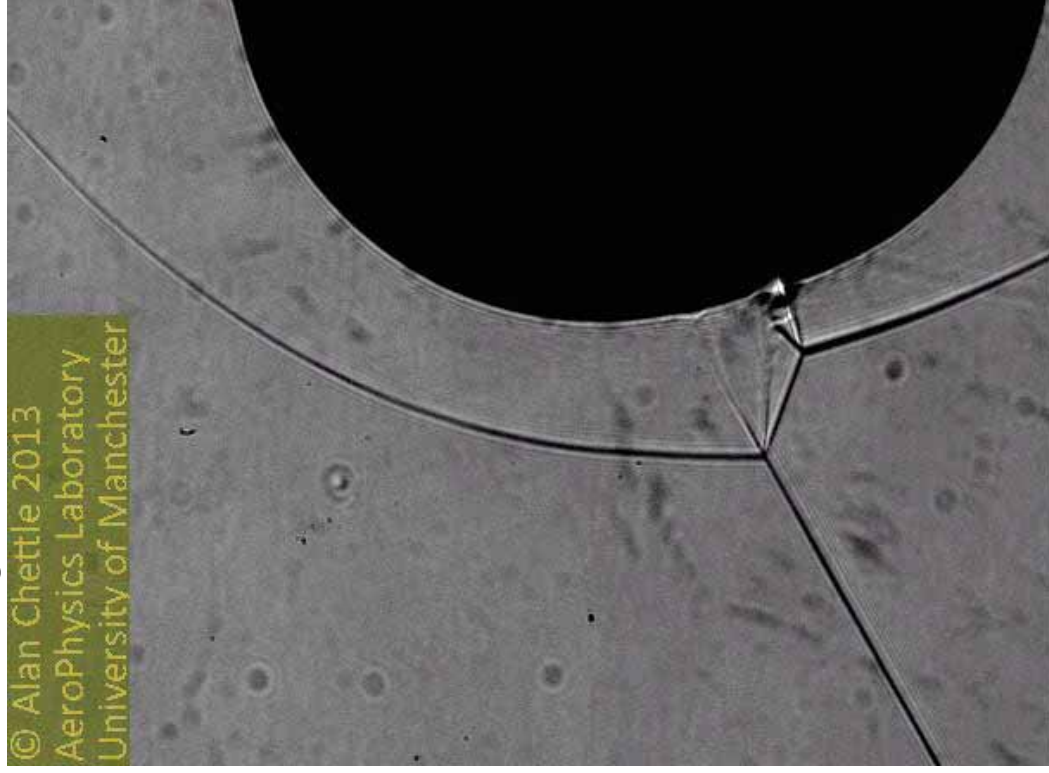


Experimental Results

15 Degrees



-15 Degrees



Moving Forward

- Continuing the experimental programme with hemisphere cylinder and swept cylinder
- This includes thin film temperature measurements at high thermal and temporal resolution
- A high powered laser (10 J, 5 Hz) will be used in the energy deposition experiments
- Tests will be conducted to evaluate effectiveness of a counter-flow jet as well

APPENDIX B:

Paper presented in the 29th ISSW,
Wisconsin, USA, July 2014

Edney IV Interactions at Mach 5: Baseline Results

A. Chettle¹, Dr. E. Erdem¹, and Prof. K. Kontis.¹

1 Introduction

The significance of Edney Type IV interactions, or shockwave interference heating as it was first labelled was seen in a flight test of the X-15 hypersonic research aircraft. A hypersonic research engine model was attached to the underside of the aircraft, and the oblique shock generated by the wing of the X-15 interacted with the bow shock of the engine support pylon [1]. This resulted in catastrophic damage to the pylon and incineration of part of the protective skin. This damage was due to an increase in the peak heat transfer and pressure at the surface of the pylon. Understanding and controlling these interactions is a key part of moving forward in creating and maintaining a viable hypersonic program.

1.1 Background

These shockwave interactions were first characterised by Barry Edney [2], where the intensity and severity of the interaction depends on where the oblique shock impinges on the bow shock. Figure 1 shows a schematic of the interaction of greatest interest - Type IV, which experiences the greatest increase in localised heat transfer and pressure. This is due to a supersonic jet impinging on the surface of the blunt body.

University of Manchester, Sackville St. M13 9PL, Manchester, United Kingdom

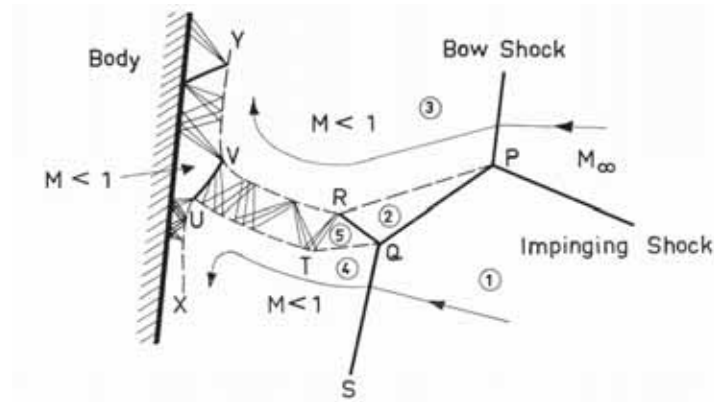


Fig. 1: Edney Type IV Interference [2]. Flow is from right to left

2 Methodology

2.1 Hypersonic Tunnel

The high speed wind tunnel used for this research is an intermediate blow-down hypersonic tunnel, using dry air as the working fluid, with a test time of approximately 7.5 seconds. The system is comprised of a high pressure vessel, an electric heater, an axisymmetric nozzle, the working section, vacuum tanks and auxiliary systems. The auxiliary systems are mainly pressure supply, water cooling and pumping. A Mach 5 nozzle is used, giving an axisymmetric nozzle exit diameter of 152 mm. The working gas is heated to 375 K - this is to avoid condensation in the test section, with a stagnation pressure of 6.45 bar. This gives a unit Reynolds number of $13 \times 10^6/\text{m}$.

2.2 Experimental Program

Two sets of tests have been performed. The first was a set of baseline experiments that established drag and lift measurements under the test conditions described in Section 2.1 for a 25 mm diameter hemisphere cylinder. The second set of tests established the same parameters in the presence of shock impingement to create Edney Type IV interference. These tests involve angles of attack of $0, \pm 5, \pm 10$ and ± 15 degrees. For the tests at $0, \pm 5, 10$ and 15 degrees, the shock generator was not moved. The tests at -10 and -15 degrees necessitated moving the shock generator to ensure Edney Type IV interaction was obtained. In both sets of tests, density based

optical techniques were employed to capture the shock interactions in the clearest manner possible.

2.3 Diagnostic Techniques

Parameters of interest to this investigation include the change in the shock structure (both spatially and temporally) and aerodynamic forces. These are obtained by use of Schlieren and Shadowgraph and a three component force balance. Schlieren results are presented where the shock structures are simple enough that the greater sensitivity given by schlieren would not be detrimental to understanding the flow characteristics. Shadowgraph results are presented for a clearer view of the shock interactions. Drag and lift measurements are obtained using a three component force balance, with a sample rate between 4-5 KHz, but maximum data storage rate of 300 Hz. The uncertainty in the lift and drag measurements is ± 0.074 N [3].

3 Results

3.1 Schlieren and Shadowgraph

An overall schlieren image (Figure 2) of the experimental setup is given here, followed by shadowgraph images (Figure 3) of the flow at different angles of attack. Shadowgraph was selected because it would more clearly show the complex shock structures expected from Edney Type IV interactions. Images of the flow without an impinging shock are not included, as the shape and structure of the bow shock is well known.

The shadowgraph images displayed in figure 3 demonstrate both that Edney IV interference is seen throughout, but also that at the different angles of attack, there is a difference in the shock structure. The most noticeable difference is in the length of the straight shock connecting the impinging oblique shock and the bow shock. With increase in angle of attack, this increases in length - it can be supposed that for continued increase, the shock interaction would become Edney III interference, but that does not occur in these images. Similarly, for an angle of attack of -5 and -10 degrees, the connecting shock is shorter, which would eventually transition to Edney V interference, but again, that transition does not take place.

3.2 *Lift and Drag Measurements*

In addition to capturing schlieren and shadowgraph images, lift and drag measurements were taken for each angle of attack, using a three-component force balance.

The lift measurements show a trend which bears deeper investigation. For negative angles of attack, the lift from Edney IV interference is quite close to the straight line obtained from the undisturbed case. However, there is a significant increase in lift starting at 0 degrees, and this trend grows as the angle of attack increases. This could be due to the shock structures moving from the centreline of the hemisphere cylinder towards the underside of the hemisphere cylinder, most prominent in figures 3c and 3d. The presence of the supersonic jet impinging on the hemisphere cylinder increases the local pressure, and with a greater pressure on the underside, a greater lift can be expected. However, this is not the case in figures 3a and 3b, where a significant increase in lift is still observed.

The drag measurements show a fairly consistent trend of a roughly flat increase in drag until the positive angles of attack are reached. For those positive angles of attack, the drag is still higher for Edney IV interactions, but the amount of increase decreases quite drastically. The reason for this change in behaviour bears further investigation, as the shock structures seen in figures 3c and 3d are very similar to that seen in figure 3g, but the drag for that case follows the trend seen for angles between -15 and 0 degrees.

References

1. J. Watts: Flight experience with shock impingement and interference heating on the X-15-2 research airplane, NASA Technical Reports, **NASA TM** (X-1669), (1968)
2. Barry Edney: Anomalous heat transfer and pressure distributions on blunt bodies at hypersonic speeds in the presence of an impinging shock, Aeronautical Research Institute of Sweden, **FFA Report** (115), (1968)
3. E. Erdem: Active Flow Control Studies at Mach 5: Measurement and Computation. Ph.D, University of Manchester, Manchester (2011)

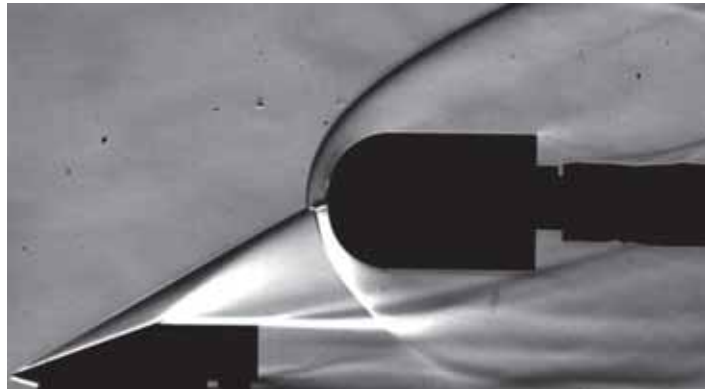


Fig. 2: Schlieren image of Edney IV interference, using a 20° shock generator and a 25 mm hemisphere cylinder. Flow is from left to right

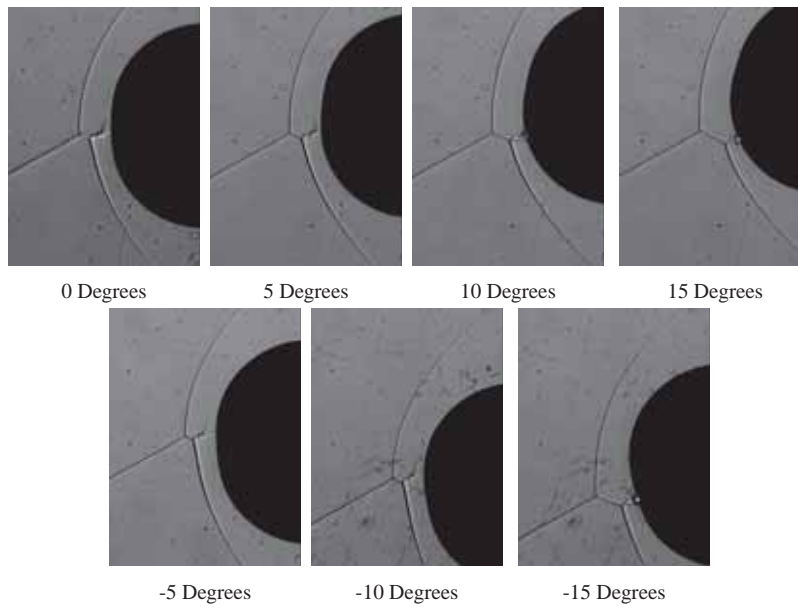


Fig. 3: Shadowgraph of Edney Type IV interactions on a hemisphere cylinder at different angles of attack.

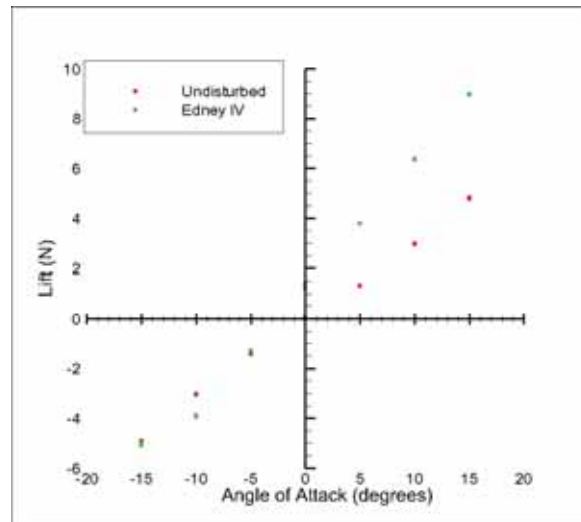


Fig. 4: Lift data for Edney Type IV interference and an undisturbed bow shock. The y-axis displays the lift in newtons and the x-axis displays the angle of attack in degrees

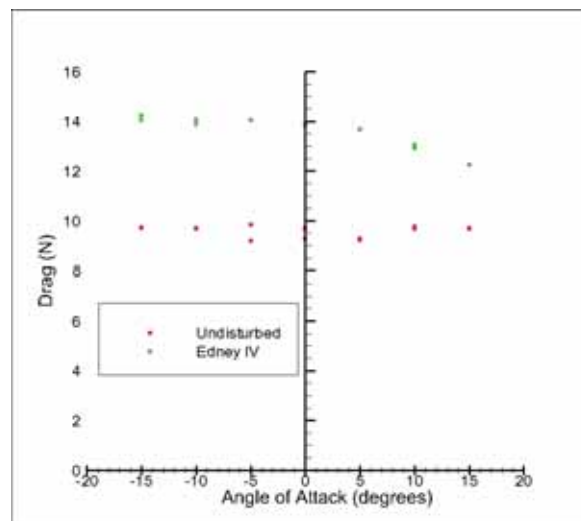


Fig. 5: Drag data for Edney Type IV interference and an undisturbed bow shock. The y-axis displays the drag in newtons and the x-axis displays the angle of attack in degrees